Time-Resolved Investigations on the Charge Carrier Dynamics of $CuBi_2O_4$ and Cu_2O Photocathodes for Photoelectrochemical Hydrogen Evolution Reaction

by

Emir Ardalı

A Dissertation Submitted to the
Graduate School of Sciences and Engineering
in Partial Fulfillment of the Requirements for the Degree of

Master of Science

in

Chemistry

August 5, 2024

Time-Resolved Investigations on the Charge Carrier Dynamics of $CuBi_2O_4$ and Cu_2O Photocathodes for Photoelectrochemical Hydrogen Evolution Reaction

Koç University

Graduate School of Sciences and Engineering

This is to certify that I have examined this copy of a master's thesis by

Emir Ardalı

and have found that it is complete and satisfactory in all respects,
and that any and all revisions required by the final
examining committee have been made.

Committee Members:

_____

Assoc. Prof. Sarp Kaya (Advisor)

_____

Prof. Alphan Sennaroğlu

_____

Prof. Uğur Yahşi

Date: 05.08.2024

To my dear grandparents Habibe, Ruhiye, and Nejat...

ABSTRACT

Time-Resolved Investigations on the Charge Carrier Dynamics of $CuBi_2O_4$ and Cu_2O Photocathodes for Photoelectrochemical Hydrogen Evolution Reaction

Emir Ardalı

Master of Science in Chemistry

August 5, 2024

As green hydrogen starts to become a more prominent candidate for being the fuel of the future, research on solar hydrogen production methods is gaining widespread attention. Among these methods, photoelectrochemical (PEC) overall water splitting (OWS) stands out as a compact technology that aims to combine sunlight with electrochemistry by using light-absorber semiconductor materials. A conventional PEC OWS setup consists of a photoanode and a photocathode that can convert the energy of solar light into photocurrent to split water molecules into molecular oxygen and hydrogen, respectively. Although the molecular oxygen production at the photoanode surface, known as oxygen evolution reaction (OER), is the main bottleneck of PEC OWS, the achievement of a fully functional cell equally relies on the optimization of the molecular hydrogen production at the photocathode compartment, also known as hydrogen evolution reaction (HER). Therefore, the investigations carried out within the scope of this thesis focus on photocathode research, which has been in scarce volumes compared to photoanode research. In particular, two promising photocathode candidates, $CuBi_2O_4$ (CBO) and Cu_2O are studied in detail with the utilization of two different approaches.

The PEC activity of a photoelectrode is a vital property that is primarily dependent on the successful utilization of the charge carriers within the system. In this context, a time-resolved investigation of the charge carrier dynamics upon illumination opens new possibilities for comprehending and optimizing photoelectrodes to unlock the full potential of PEC OWS. Such charge carrier events that are influential on the generation of photocurrent in photoelectrodes can occur at timescales as short as a few femtoseconds up to a relatively longer time duration of a second. In the first part of the thesis, ultrafast polaronic charge trapping and recombination dynamics of compositionally manipulated CBO photocathodes are screened via *ex situ* and *in situ* ultrafast transient absorption spectroscopy (TAS). In the second part, interfacial charge trapping, accumulation, and utilization dynamics of Cu_2O-based single or heterojunction photocathodes are investigated via transient photocurrent (TPC) experiments. Throughout the thesis, time-resolved investigations are combined with advanced structural characterization techniques and complementary PEC performance tests to develop a thorough understanding of the effects of structural differences on ultrafast charge transport and interfacial charge transfer dynamics.

Intrinsically, p-type photocathodes such as CBO gain their p-type behavior from the cation vacancies that are found in their crystal lattices as natural dopant sites. Yet, such vacancy sites hold the capacity to polaronically trap valence band (VB) holes, which results in their recombination with conduction band (CB) electrons. There are two common types of cation vacancies (Cu^{2+} vacancy: V''_{Cu} and Bi^{3+} vacancy: V'''_{Bi}) that can be found within the CBO lattice, which can act as polaronic trap sites and hinder the ultrafast charge transport. Therefore, unraveling the differences between the two types of

vacancy sites in terms of polaronic charge trapping is of great importance. For this purpose, two different types of cation-deficient CBO photocathodes were fabricated. The structural and PEC properties of these Cu- and Bi-deficient CBO photocathodes were analyzed to understand their possible influence on the charge transfer processes. Later, ultrafast charge carrier dynamics screening of CBO photocathodes was carried out under *ex situ* and *in situ* conditions via ultrafast TAS measurements. Through the sequence of such experiments, the transient absorption (TA) spectral features near 460 nm and 560 nm were successfully assigned to dominant hole absorption (HA) and hole polaron absorption (HPA) character, respectively. Later, it was revealed that the $V_{Bi}^{'''}$ sites are more prone to polaronically trap the VB holes and retard the ultrafast hole transport causing poorer photocurrent generation in Bi-deficient CBO photocathodes.

Heterojunction photoelectrodes are prominent devices for achieving enhanced interfacial charge transfer dynamics that allow better PEC OWS efficiencies. Therefore, the application of such a concept to one of the most popular photocathode candidates, Cu_2O, has been introduced previously. Cu_2O photocathodes and their heterojunctions with TiO_2 are widely studied topics within the field of PEC HER research. Still, the potential-dependent interfacial charge transfer dynamics of such systems have yet to be understood. In this context, the fabrication of bare Cu_2O, bare TiO_2, and TiO_2/Cu_2O systems was carried out, and their structural properties were analyzed via surface- and bulk-sensitive characterization methods. The PEC performances of all three systems were tested under chopped light conditions through consecutive linear sweep voltammetry (LSV) scans. The Cu_2O optimization experiments showed that an hour-long electrodeposition of the Cu_2O layer results in larger grain sizes, higher crystallinity, and a smaller number of defects compared to shorter durations. Therefore, an hour-long electrodeposition duration was found to increase the PEC stability of photocathodes to a great extent. Later, the interfacial charge carrier dynamics of bare Cu_2O, bare TiO_2, and TiO_2/Cu_2O heterojunction systems were investigated through potential-dependent TPC measurements performed at millisecond resolution. The potential-dependent TPC responses of the bare Cu_2O and heterojunction photocathodes revealed that the interfacial hole trapping is more dominant below 0.3 V for Cu_2O while the heterojunction system mostly suffers from the electron trapping above 0.3 V. As a result of these findings, it was determined that the heterojunction system was subjected to less Cu reduction below 0.3 V compared to bare Cu_2O, enabling the heterojunction system to have a more stable PEC performance. More importantly, the periodic oscillations observed along the photocurrent baseline are considered to stem from the side processes that occur in parallel with the PEC OWS reactions. Such periodically occuring anodic and cathodic events are expected to involve the consumption of trapped charge carrier populations and, therefore, influence the working mechanisms of photocathodes. Yet, further *in situ* time-resolved spectroscopic investigations are essentially required to resolve such concepts.

Overall, the thesis sheds light on the charge carrier dynamics of photocathodes during their operation for PEC HER by combining time-resolved investigations with an elaborate understanding of structure and performance. Eventually, a detailed picture of the photocurrent generation mechanism in both CBO and Cu_2O photocathodes is provided.

ÖZETÇE

Fotoelektrokimyasal Hidrojen Evrim Reaksiyonu için $CuBi_2O_4$ ve Cu_2O Fotokatotların Yük Taşıyıcı Dinamikleri Üzerine Zamana Bağlı İncelemeler

Emir Ardalı

Kimya, Yüksek Lisans

5 Ağustos 2024

Yeşil hidrojenin geleceğin yakıtı olmaya aday gösterilmesi ile birlikte güneş enerjisiyle hidrojen üretim yöntemleri üzerine araştırmalar da yaygınlaşmaktadır. Bu yöntemler arasında fotoelektrokimyasal (PEC) bütünleşik su ayrıştırması (OWS), ışık soğurucu yarı iletken malzemeler kullanarak güneş ışığını elektrokimya ile birleştirmeyi amaçlayan kompakt bir teknoloji olarak öne çıkmaktadır. Yaygın bir PEC OWS sistemi, su moleküllerini sırasıyla moleküler oksijen ve hidrojene ayırmak için güneş enerjisini fotoakıma dönüştürebilen bir fotoanot ve bir fotokatottan oluşur. Oksijen evrim reaksiyonu (OER) olarak bilinen fotoanot yüzeyindeki moleküler oksijen üretimi, PEC OWS'nin ana sınırlayıcısı olmasına rağmen, tamamen işlevsel bir hücrenin elde edilmesi, aynı zamanda fotokatot bölmesinde gerçekleşen ve hidrojen evrim reaksiyonu (HER) olarak da bilinen moleküler hidrojen üretiminin optimizasyonuna da eşit derecede bağlıdır. Dolayısıyla bu tez kapsamında yapılan araştırmalar, fotoanot araştırmalarına göre sayıca az olan fotokatot araştırmalarına odaklanmaktadır. Özellikle, gelecek vaat eden iki fotokatot adayı olan $CuBi_2O_4$ (CBO) ve Cu_2O, iki farklı yaklaşım ile ayrıntılı olarak incelenmiştir.

Bir fotoelektrodun PEC aktivitesi, sistem içindeki yük taşıyıcılarının başarılı kullanımına bağlı olan önemli bir özelliktir. Bu bağlamda, aydınlatma sonrasında gerçekleşen yük taşıyıcı dinamiklerinin zamana bağlı olarak araştırılması PEC OWS'nin tüm potansiyelini ortaya çıkarmak için fotoelektrotların anlaşılması ve optimize edilmesi için yeni olanaklar açmaktadır. Fotoelektrotlarda fotoakım oluşumu üzerinde etkili olan bu tür yük taşıyıcı olayları, birkaç femtosaniyeden nispeten daha uzun bir zaman dilimi olan bir saniyeye kadar olan zaman ölçeklerinde meydana gelebilir. Tezin ilk bölümünde, kimyasal kompozisyon olarak manipüle edilmiş CBO fotokatotların ultra hızlı polaronik yük tuzaklama ve yeniden birleşim dinamikleri, *ex situ* ve *in situ* ultra hızlı süreksiz absorpsiyon spektroskopisi (TAS) kullanılarak taranmıştır. İkinci bölümde Cu_2O bazlı tek veya heterobağlantılı fotokatotlarının arayüzey yük tuzaklama, birikim ve kullanım dinamikleri geçici fotoakım (TPC) deneyleri ile incelenmiştir. Tez boyunca, yapısal farklılıkların ultra hızlı yük taşınımı ve arayüzey yük aktarımı dinamikleri üzerindeki etkilerinin kapsamlı bir şekilde anlaşılmasını sağlamak için zamana bağlı araştırmalar, gelişmiş yapısal karakterizasyon teknikleri ve tamamlayıcı PEC performans testleri ile birleştirilerek kullanılmıştır.

Özünde, CBO gibi p-tipi fotokatotlar, p-tipi davranışlarını, doğal katkı bölgesi davranışı gösteren ve kristal kafes yapısı içinde bulunan katyon boşluklarından alırlar. Ancak bu tür boşluk bölgeleri, değerlik bandında (VB) bulunan elektron boşluklarını polaronik olarak tuzaklama kapasitesine sahiptir. Bu durum da tuzaklanan boşlukların iletim bandında (CB) bulunan elektronlarla yeniden birleşimi ile sonuçlanır. CBO kafesinde bulunabilen iki yaygın katyon açıklığı türü (Cu^{2+} kusur açıklığı: V''_{Cu} ve Bi^{3+} kusur açıklığı: V'''_{Bi}) de polaronik tuzak bölgeleri olarak hareket edebilir ve ultra hızlı yük

taşınımını engelleyebilir. Bu nedenle, polaronik yük yakalama açısından iki tip açıklık alanı arasındaki farkların çözülmesi büyük önem taşımaktadır. Bu amaçla iki farklı tipte katyon eksikliği bulunduran CBO fotokatot üretilmiştir. Cu ve Bi eksikliği olan CBO fotokatotların yapısal ve PEC özellikleri, yük taşınımı süreçleri üzerindeki olası etkileri anlamak amacıyla bu kapsamda analiz edilmiştir. Daha sonra CBO fotokatotlarının ultra hızlı yük taşıyıcı dinamiği taraması, ultra hızlı TAS ölçümleri yoluyla *ex situ* ve *in situ* koşullar altında gerçekleştirilmiştir. Bu tür deneyler aracılığıyla, 460 nm ve 560 nm civarında gözlemlenen süreksiz soğurma (TA) spektral bulguları sırasıyla, baskın boşluk absorpsiyonu (HA) ve boşluk polaronu absorpsiyonu (HPA) karakteri ile ilişkilendirilmiştir. Bu sayede $V_{Bi}^{'''}$ bölgelerinin VB boşluklarını polaronik olarak tuzaklamaya ve ultra hızlı delik taşınımını geciktirmeye daha yatkın olduğu ve bu durumun da yapısında Bi eksikliği bulunduran CBO fotokatotlarda daha zayıf fotoakım üretimine neden olduğu tespit edilmiştir.

Heterobağlantılı fotoelektrotlar, gelişmiş arayüzey yük aktarım dinamikleri elde etmek için öne çıkan ve bu sayede daha iyi PEC OWS verimliliğine ulaşılmasına olanak tanıyan cihazlardır. Bu nedenle böyle bir konseptin en popüler fotokatot adaylarından biri olan Cu_2O'e uygulanması hali hazırda yapılmıştır. Cu_2O fotokatotları ve bunların TiO_2 ile heterobağlantısının yapılması, PEC HER araştırmaları alanında geniş çapta incelenen konulardır. Buna rağmen, bu tür sistemlerin potansiyele bağlı arayüzey yük transfer dinamikleri henüz tam olarak anlaşılamamıştır. Bu kapsamda yalın Cu_2O, yalın TiO_2 ve TiO_2/Cu_2O sistemlerinin sentezi gerçekleştirilmiş olup, yüzey ve yığına duyarlı karakterizasyon yöntemleriyle yapısal özellikleri analiz edilmiştir. Her üç sistemin de PEC performansları, ardışık doğrusal tarama voltametrisi (LSV) ölçümleri yoluyla kesikli ışık koşulları altında test edilmiştir. Cu_2O optimizasyon deneyleri, Cu_2O katmanının bir saat süren elektrokaplama sonucunda daha kısa sürelerle karşılaştırıldığında daha büyük tane boyutlarına, daha yüksek kristallenme derecesine ve daha az sayıda yapısal kusura yol açtığını göstermiştir. Bu nedenle bir saat süren elektrokaplama süresinin fotokatotların PEC stabilitesini büyük ölçüde arttırdığı gözlemlenmiştir. Daha sonra, yalın Cu_2O, yalın TiO_2 ve heterobağlantılı TiO_2/Cu_2O sistemlerinin arayüzey yük taşıyıcı dinamikleri, milisaniyelik çözünürlükte gerçekleştirilen potansiyele bağlı TPC ölçümleri aracılığıyla incelenmiştir. Yalın Cu_2O ve heterobağlantılı fotokatotların potansiyele bağlı TPC yanıtları, 0.3 V'un altında Cu_2O'te arayüzeysel boşluk tuzaklanmasının daha baskın olduğunu, öte yandan heterobağlantılı sistemin ise 0.3 V'un üstünde baskın olarak elektron tuzaklamasına maruz kaldığını ortaya çıkarmıştır. Bu bulgular neticesinde yalın Cu_2O'e kıyasla heterobağlantılı sistemin 0.3 V'un altında daha az Cu indirgenmesine maruz kaldığı ve bu durumun da heterobağlantılı sistemin daha stabil bir PEC performansına sahip olmasını sağladığı tespit edilmiştir. Daha da önemli bir bulgu olarak fotoakım eğrisi boyunca gözlemlenen ilginç periyodik salınımların, PEC OWS reaksiyonlarına paralel olarak meydana gelen yan reaksiyonlardan kaynaklandığı düşünülmektedir. Bu tür periyodik olarak meydana gelen anodik ve katodik olayların tuzaklanmış yük taşıyıcı popülasyonlarının tüketimini içerdiği ve dolayısıyla fotokatotların çalışma mekanizmasını etkilediği sonucuna varılmaktadır. Bu tür ilginç konseptlerin yakın gelecekte çözümlenebilmesi için *in situ* zamana bağlı spektroskopik araştırmalara esasen ihtiyaç duyulmaktadır.

Genel olarak bu tez çalışması, zamana bağlı araştırmaları ayrıntılı yapı ve performans anlayışıyla birleştirerek, fotokatotların PEC HER sırasındaki yük taşıyıcı dinamiklerine ışık tutmaktadır. Bu çalışmalar sonucunda hem CBO hem de Cu_2O bazlı fotokatotlardaki fotoakım üretim mekanizmasına dair ayrıntılı bir kavrayış geliştirilmiştir.

AKNOWLEDGEMENTS

First of all, I would like to dedicate this thesis to my dear late grandparents Habibe, Ruhiye, and Nejat. Growing up with grandparents who supported me unconditionally was a true blessing. Although they are gone, their memories will live on with me until the very end of my life. I love them and will keep on doing everything I can to make them proud.

Secondly, I want to thank my dear mother, Burcu, for being my biggest supporter in life and my beloved father, Ömer, for planting the seeds of my curiosity in nature at an early age. I also thank my dear aunts İrem and Mübeccel for being second mothers to me. I thank my dear late aunt Azra and my dear late uncle Yaşar for being my guardian angels. I especially thank İlhan for being my role model in pursuing an academic career. Last but not least, I thank all my other family members who have believed in me up to this point.

Most importantly, I would like to use this chance to thank my dear advisor, Assoc. Prof. Sarp Kaya. He gifted me a career in science with his exceptional mentorship since day one. Terms like “hard work” and “motivation” were re-defined after I started to work with him, and I firmly believe that without this re-definition, I wouldn’t be who I am today. I have spent nearly three years in his laboratory, with highs and lows, but looking back makes me realize how lucky I was to be his student and be a part of his lab.

I also thank my dear co-advisor, Prof. Alphan Sennaroğlu, for accepting me to Koç University Laser Research Laboratory from the beginning of my master’s studies as a chemist who knows almost nothing about lasers. Alongside my main research, he encouraged me to become a part-time laser researcher, which resulted in novel outcomes and allowed me to gain a broader perspective on light-matter interactions.

Additionally, I thank Prof. Uğur Yahşi for accepting to be my thesis defense jury member. I also would like to thank him and Prof. Cumali Tav for teaching me the basics of positron spectroscopy and allowing me to join their laboratory for a few days during our collaboration.

I equally thank my dear mentors and experimental collaborators, Res. Asst. Prof. Yağız Morova and Dr. Hadi Jahangiri. Without their determination, none of my scientific outcomes could have been possible. I also thank them for their mental support at times when things went wrong. I thank Dr. Barış Yağcı for his patience with me when I always showed up with more samples than I promised during the FESEM and XPS measurements. His music taste and sense of humor, along with our hours-long conversations on basically anything, will be dearly missed. I thank Dr. Pınar Tatar Güner

for being my idol in teaching and showing me effective but fun ways of teaching science. Her patience for both her teaching assistants and students will be my guide in my teaching career. I would also like to extend my gratitude to Assoc. Prof. Uğur Ünal, Prof. Alper Uzun, and Assoc. Prof. Önder Metin, and all my other professors and teachers who taught and inspired me throughout these three years.

Especially, I would like to thank my loved ones Hanna, Atılay, Şafak, Sinan, and Beyza for sharing the best times and providing the mental support that I needed. I thank Yunus for not only being the best flatmate but also such a good friend. I thank Ece for her close and thoughtful friendship. She was always there whenever I needed it.

I thank my sarpkayaLAB friends, who have been nothing but the best. I thank Tuğçe for being the best companion in good and bad times in the lab. I thank Fatih for being the best project mate ever. I thank Kaan and Başak for the long days and nights together in and outside of the lab. I thank Amin for showing unconditional help and support not only to me but also to anyone who needs it. Thanks to Öykü and Emre for being the kindest and answering my neverending questions about PEC experiments. I thank Saeede, Hana, and Shervin for their sincere friendship and teachings. Without their help, the second part of my thesis wouldn't be here. Thanks to Navid for his vision and collaboration. He was one of the first persons to remind me that I can and should try harder. I thank Timuçin for being a true big brother to all of us in and outside the lab. I thank Maida and Muhammed for showing me that friendship and chaos can coexist in such harmony. Thanks to Mert and Ela for their not-so-distant friendship from Tüpraş. I thank Esmail and Samira for their nice wishes along the way. I also thank my "little" friends Azra, Eğin, Alp, Ali, Hasan, Özce, and Esra for harmonizing with the lab culture and allowing us to both teach them and learn from them.

I would also like to thank my laser lab friends. Thanks to Nihan for her supportive friendship and for teaching me how to build my first laser. I thank Derya for his generous friendship and endless inspiration. I also thank Berke, Suat, Minahil, Ayşenur, Melih, and all my other LRL friends, who have inspired me from many different perspectives.

Lastly, I thank all my friends from other labs who do their amazing things. I thank Nitasha, Samira, Ezgi, and others from the other side of KUTEM, Mine, Ferid, İrem, Işıl and others from Funtech, Gizem and Bengisu from UnalLab and many many more.

PS: Little Emir would have been so proud to see this.

TABLE OF CONTENTS

LIST OF TABLES

LIST OF FIGURES

ABBREVIATIONS AND SYMBOLS

A	Absorption
CA	Chronoamperometry
CB	Conduction Band
CBO	$CuBi_2O_4$ (Copper Bismuth Oxide)
CP	Chronopotentiometry
C_s	Capacitance
DBS	Doppler Broadening Spectroscopy of Positron Annihilation
EDX	Energy Dispersive X-Ray Spectroscopy
E_g	Optical Band Gap Energy
FESEM	Field Emission Scanning Electron Microscopy
FTO	$F:SnO_2$ (Fluorine-Doped Tin Oxide)
HA	Hole Absorption
HER	Hydrogen Evolution Reaction
HHC	Hot Hole Cooling
HPA	Hole Polaron Absorption
HPF	Hole Polaron Formation
HT	Hole Transfer
IPCE	Incident Photon-to-Current Efficiency
IVBA	Intra-Valence Band Absorption
i	Current
j	Current Density
LSV	Linear Sweep Voltammetry
MS	Mott-Schottky
N_A	Acceptor Density
OCP	Open Circuit Potential
OER	Oxygen Evolution Reaction
OWS	Overall Water Splitting
PEC	Photoelectrochemistry
PEIS	Photoelectrochemical Impedance Spectroscopy
R_{CT}	Charge Transfer Resistance
RHE	Reversible Hydrogen Electrode

SHE	Standard Hydrogen Electrode
STH	Solar-to-Hydrogen
TAS	Transient Absorption Spectroscopy
TPC	Transient Photocurrent
VB	Valence Band
XPS	X-Ray Photoelectron Spectroscopy
XRD	X-Ray Diffraction
ΔA	$A_{Unpumped} - A_{Pumped}$
φ	Applied Potential
φ_{fb}	Flatband Potential
V''_{Cu}	Cu^{2+} Vacancy
V'''_{Bi}	Bi^{3+} Vacancy

Chapter 1:
INTRODUCTION

1.1 Solar Hydrogen Production

Green hydrogen holds the potential to become the fuel of the future owing to its environmentally friendly and sustainable as well as highly efficient nature. Compared to non-renewable fossil fuels such as petrol and natural gas, hydrogen holds a gravimetric heating value of 141.9 MJ.kg^{-1}, which is around three times larger than of petrol (47.5 MJ kg^{-1}) and natural gas (55.5 MJ kg^{-1})[1]. Yet, non-renewables still account for around 85% of energy consumption around the Globe and are the most significant cause of carbon emissions that lead to global warming and climate change[2]. Therefore, replacing fossil fuels with hydrogen holds great importance in overcoming carbon emissions and their effects. However, in today's world, conventional hydrogen production is also based on carbon-emitting, low efficiency black and gray methods[2], [3]. From this perspective, solar-driven hydrogen production via photochemical (PC), photoelectrochemical (PEC), and photovoltaic-electrochemical (PV-EC) overall water splitting (OWS) with several other methods shown in Figure 1.1 is crucial for the green production of hydrogen[4].

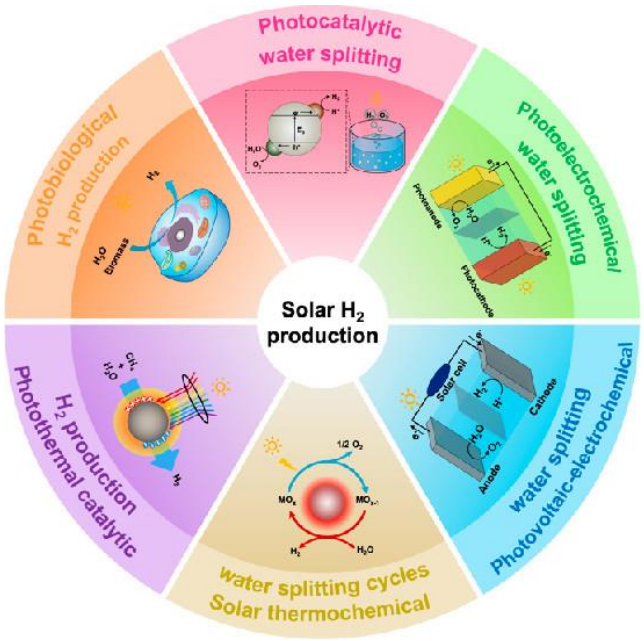

Figure 1.1: Solar hydrogen production methods[4].

1.2 Overall Water Splitting

In OWS, water is split into molecular oxygen and hydrogen species through the oxidation of water in the oxygen evolution reaction (OER) and the reduction of protons in the hydrogen evolution reaction (HER)[5]. Nonetheless, the solar hydrogen production methods differentiate from each other both energetically and mechanistically in catalyzing water redox reactions[4]. Specifically, PEC OWS has stood out among these techniques as a compact technology that combines light absorption and electrochemical conversion in a single device, as shown in Figure 1.2 rather than combining two systems as done in PV-EC OWS[6].

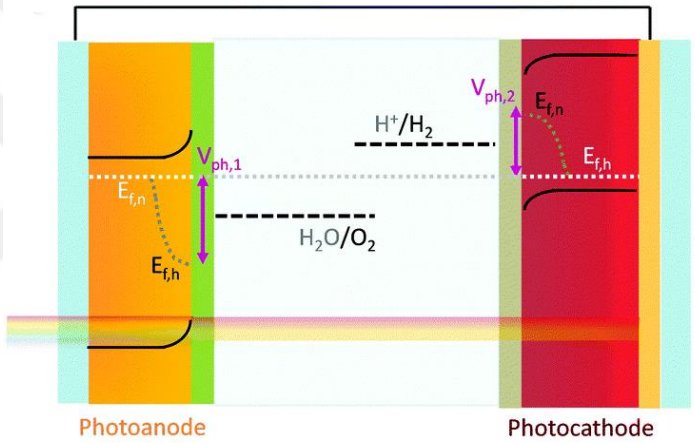

Figure 1.2: Photoanode–photocathode tandem cell diagram for PEC OWS[7].

Additionally, unlike PC OWS, the PEC technology allows OER and HER to occur on separate electrode surfaces and, therefore, prevents back reactions and gas explosions[8]. However, although the technology has drawn attention for over five decades, no wide commercial application of it does not seem possible without the use of noble metal cocatalysts due to low solar-to-hydrogen (STH) conversion efficiencies in self-biased PEC OWS trials with non-noble metal-based semiconductor systems[6], [9]. Hence, further research on non-noble metal-based semiconductor systems is immensely needed to achieve true low-cost, real-life applications of PEC OWS.

1.3 Hydrogen Evolution Reaction

The rate of PEC OWS (Eq. 1.3) is determined by the rate of OER (Eq. 1.1) since it is kinetically the more challenging reaction occurring at +0.40 V vs. standard hydrogen electrode (SHE) under alkaline conditions. On the other hand, HER (Eq. 1.2) is expected to occur at −0.83 V vs. SHE with OWS reaction having a reversible cell potential of -1.23 V vs. SHE (Eq. 2)[7], [10], [11].

$$\text{OER: } 2OH^- + 2h^+ \rightarrow H_2O + \frac{1}{2}O_2 \ (E^\circ = +0.40 \text{ V vs. SHE}) \qquad \text{(Eq. 1.1)}$$

$$\text{HER: } 2H_2O + 2e^- \rightarrow H_2 + 2OH^- \ (E^\circ = -0.83 \text{ V vs. SHE}) \qquad \text{(Eq. 1.2)}$$

$$\text{OWS: } H_2O \rightarrow H_2 + \frac{1}{2}O_2 \ (E_{Rev} = -1.23 \text{ V vs. SHE}) \qquad \text{(Eq. 1.3)}$$

A standard PEC OWS setup consists of a tandem cell: a photoanode that is essentially an n-type semiconductor that has the proper band alignment to drive OER while eliminating HER and a photocathode that is usually a p-type semiconductor to favor HER over OER[4]. In a photoanode, the OER occurs with the accumulation of photogenerated holes at the photoanode/electrolyte interface while the photoexcited electrons are transferred to the photocathode through the external circuit[12]. Meanwhile, the HER occurs with the photoexcited electron accumulation at the photocathode/electrolyte interface as the photogenerated holes are transferred to the photoanode through the external circuit[12]. Therefore, processes that involve electrons and holes in both photoanodes and photocathodes are of great importance in terms of catalytic understanding of a PEC OWS system. However, in recent years, due to the abundance of n-type materials as suitable photoanodes for PEC OER, the research on photoanodes has surpassed the research on photocathodes[13], [14], [15]. Still, the enigmatic nature of photocathodes requires further investigations to comprehend the reasons behind their poor reduction performances.

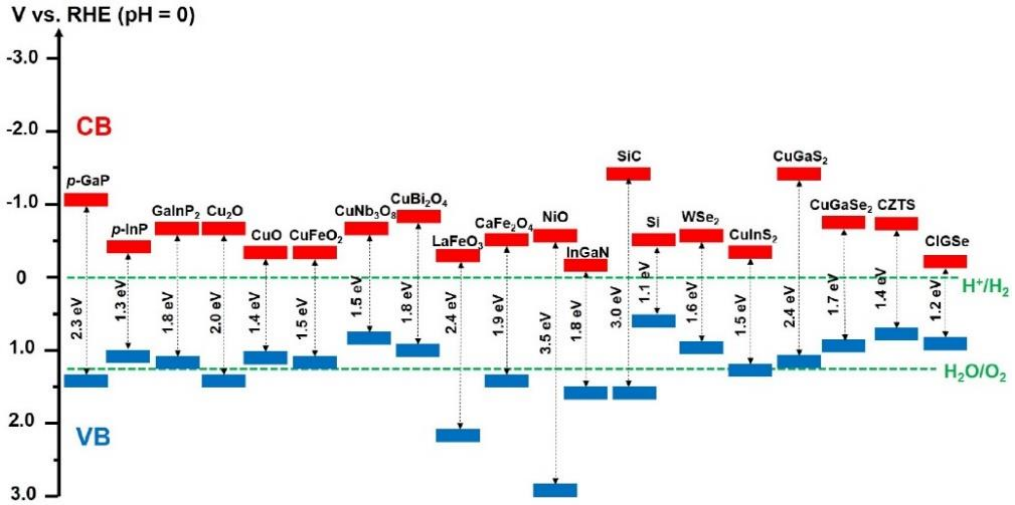

Figure 1.3: Band alignment of commonly studied p-type photocathode candidates[16].

The most studied non-noble metal-based photocathodes and their band alignments are depicted in Figure 1.3. Photocathode candidates can be grouped under five main categories as metal oxide-based (i.e. Cu_2O, $CuBi_2O_4$, NiO, p-TiO_2), metal chalcogenide-based (i.e. Sb_2Se_3, $Cu_2BaSn(S,Se)_4$), metal phosphide-based (CoP, GaP, $GaInP_2$), silicon-based (p-Si), and metal-free (g-C_3N_4) photocathodes[17]. This thesis mainly focuses on two of the most promising metal oxide-based photocathodes, $CuBi_2O_4$ and Cu_2O.

1.4 Photocathodes

1.4.1 $CuBi_2O_4$

Since its first proposal as a visible-light-responsive porous photoelectrode, tetragonal $CuBi_2O_4$ (CBO) has drawn growing attention as an alternative for over a decade[18]. As depicted in Figure 1.4, the tetragonal CBO crystal structure consists of square planar [CuO_4] planes that are interconnected via Bi atoms, which form the [BiO_6] octahedra[19]. To this day, CBO has been among the most significant photocathode materials for many photoelectrochemical (PEC) conversion reactions such as hydrogen evolution reaction (HER)[20], CO_2 reduction reaction (CO_2RR)[21], and oxygen reduction reaction (ORR)[22].

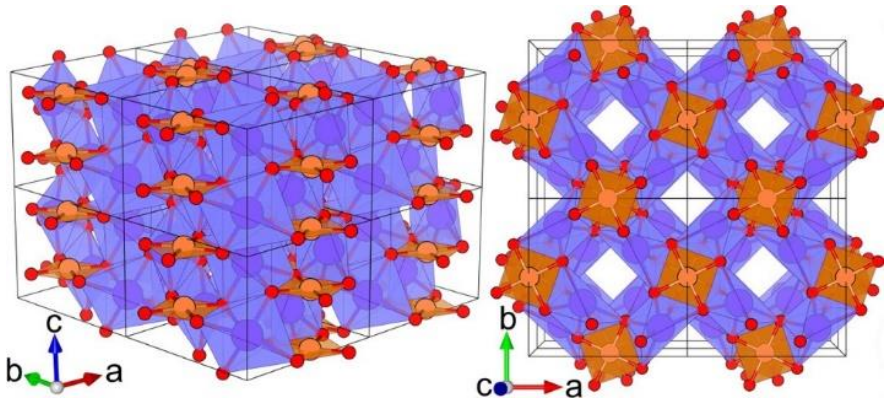

Figure 1.4: Crystal structure of CBO. Cu, Bi, and O atoms are depicted in orange, purple, and red colors, respectively[19].

Despite having a small band gap of 1.5-1.8 eV and suitable band alignment to drive the HER, the PEC performance of CBO under illumination at higher wavelengths of the visible spectrum is known to be inefficient. Therefore, it has been understood that the transitions requiring low excitation energy to populate the empty Cu 3d states in the conduction band (CB) are insignificant compared to the transitions that occur at higher energies populating Bi 6p states, which contribute to the photocurrent generation in CBO at a larger extent[19], [23], [24]. Yet, the ultrafast hole dynamics of these p-type materials have not been deeply investigated, and understanding the nature of the hole transport dynamics remains an essential step toward a complete PEC performance improvement.

Lately, the performance and stability of tetragonal CBO photocathodes have been constantly improving with the introduction of novel synthesis methods and heterostructured systems[25], [26], [27]. The intrinsic nature of the CBO structure was thoroughly investigated with the gradient self-doping method, which also improved the charge separation efficiency[28]. The revealing of the influence of antisite cationic intermixing on electronic conductivity has been an important milestone for understanding distorted energetics and their effects on the electronic structure in CBO[29]. The formation of Cu 3d hole-polaron states near the valence band (VB) edge and the hole-polaron hopping mechanism resulting from the antisite Bi_{Cu} (Bi replaces Cu) intermixing was suggested as a reason for the retarded hole conduction in CBOs[29]. On the other hand, the roles of hydrogen and oxygen defects in ultrafast charge carrier dynamics have also been explored in CBO thin films with the use of transient transmission (TT) and transient reflection (TR) spectroscopy[23]. In a more recent study, nanoporous CBOs

were point-defect engineered with rapid thermal processing for enhanced PEC activity[30]. These studies have shown that further advancements would certainly be needed to understand the hole-trapping tendencies of p-type CBOs that can be explored by the manipulation of their composition to induce cationic vacancies[23], [28], [31].

1.4.2 Cu_2O

As one of the most studied photocathodes, cuprous oxide (Cu_2O) stands out with its desirable band alignment to drive various PEC reactions, 2.0 eV band gap, and 18% theoretical STH[32]. In recent years, Cu_2O photocathodes have been under constant improvement as a PEC HER catalyst along with PEC CO_2RR research[33], [34].

Despite its advantages, Cu_2O photocathodes suffer from photocorrosion-related stability issues due to their redox potentials lying within the same potential range as HER[35]. Although the EC redox of Cu_2O photocathodes can simply be described by Eq. 1.4 and 1.5, the elementary processes that lead to the photocorrosion in these materials are rather complex and require further time-resolved PEC investigations to be completely understood.

$$Cu_2O + H_2O + 2e^- \leftrightarrow 2Cu + 2OH^- \ (+0.47 \text{ V vs. SHE}) \qquad \text{(Eq. 1.4)}$$

$$2CuO + H_2O + 2e^- \leftrightarrow 2Cu_2O + 2OH^- \ (+0.60 \text{ V vs. SHE}) \qquad \text{(Eq. 1.5)}$$

Still, to overcome the photocorrosion of these p-type photocathodes, n-type protective overlayers such as Al:ZnO and TiO_2 have been introduced [35]. These kind of protective over and underlayers are expected to form a heterojuction system with Cu_2O to extract the excess electrons that can accumulate at the photocathode/electrolyte interface upon illumination as depicted in Figure 1.5[36].

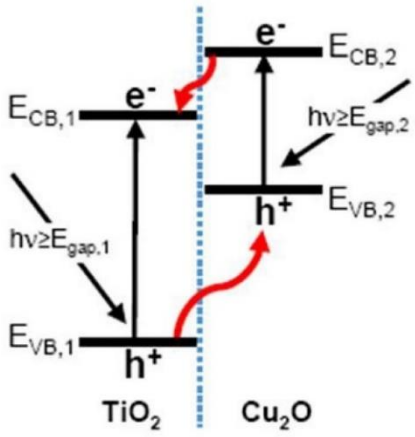

Figure 1.5: Band diagram representation of double charge transfer processes in TiO_2/Cu_2O heterojunction system[36].

If not prevented, such an excessive electron accumulation results in the photoreduction of Cu_2O to CuO and even Cu. Therefore, comprehension of the electron accumulation and extraction mechanisms of a p-Cu_2O and n-TiO_2-based type-II heterojunction system is an essential step toward understanding the interfacial charge transfer and reaction kinetics of photocathode materials.

1.5 Charge Carrier Dynamics in Photoelectrodes

1.5.1 Ultrafast Charge Transport Dynamics

As some of the most crucial processes in light-energy conversion, the ultrafast dynamics that involve charge carriers in semiconductors are fundamental [37]. Ultrafast charge carrier dynamics studies play an essential role in understanding the obstacles that hinder the photocurrent generation mechanism of photoelectrode materials for PEC reactions[38], [39]. The chain of events that takes place following photoexcitation, such as charge separation, hot carrier cooling, self-localization, polaron formation, trapping, and recombination, can be realized within ultrashort timescales, as depicted in Figure 1.6[13]. Hence, a comprehensive understanding of these processes in each system holds great importance for the successful extraction and eventual reaction of free carriers[14]. In particular, phonon-assisted self-localization of charge carriers at intraband gap states, also called polaron formation[40], [41], has been widely studied as a loss and/or transport mechanism[42], [43], [44], [45] in photoelectrode materials[46], [47], [48], [49].

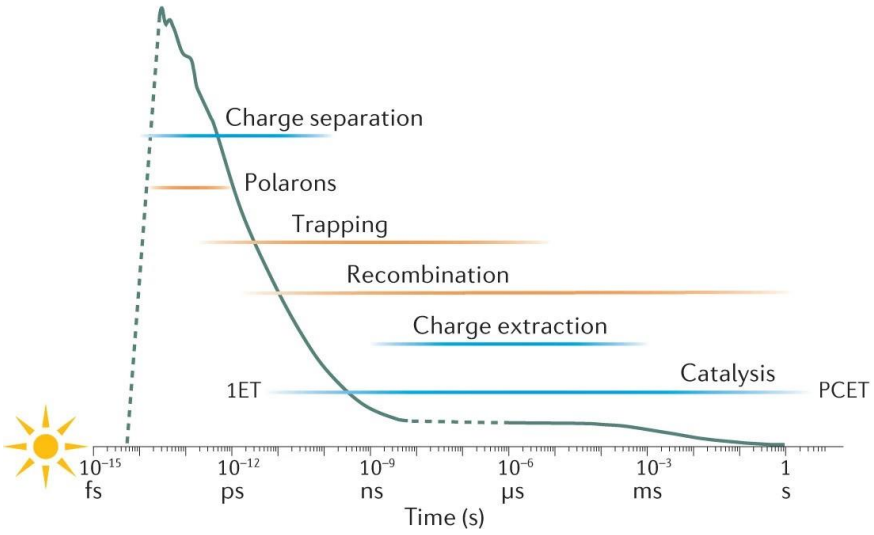

Figure 1.6: Time ranges and corresponding energy losses of charge carrier dynamics processes in photoelectrodes. 1ET is single electron transfer, and PCET is proton-coupled electron transfer[13].

Upon photoexcitation, the photogenerated holes in the VB and electrons in the CB get involved in ultrafast processes that cause the loss of these carrier populations prior to utilization. At fs-ps time scales, hot electrons and holes first go through fast, non-radiative relaxation events to reach thermal equilibrium with the lattice phonons, also called hot carrier cooling. The hot carrier cooling process is followed by the previously described polaron formation. Polarons in such a semiconductor system form under a ps via non-radiative relaxation to intraband gap states and generally occur within the same time range as the hot carrier cooling process[50]. The formation of polarons at the trap sites remarks the start of the ps-ns charge carrier trapping process. Trapped electrons and holes later radiatively recombine with VB holes and CB electrons, respectively. These trap-mediated recombination processes occur at ns-ms timescales, resulting in the hindrance of the PEC reaction rates. On the other hand, free carriers can also non-radiatively recombine at ps-ns with their excitonic counterparts[13]. Throughout all these time ranges, transient absorption spectroscopy (TAS) stands out as an effective tool for probing such ultrafast events with high precision. While these processes dominate the bulk of the photoelectrode materials, interfacial charge transfer dynamics occur at the photoelectrode/electrolyte interface and influence the reaction kinetics of the photoelectrodes for the PEC OWS reactions.

1.5.2 Interfacial Charge Transfer Dynamics

The interfacial charge transfer dynamics play a crucial role in determining the reactivity and stability of photoelectrode systems. As depicted in Figure 1.7, photogenerated electrons and holes are in a kinetic competition to be transferred or trapped at the surface states within the ms-s timescales[51], [52]. Such processes are heavily influenced by intrinsic, extrinsic, or interstitial defects found in metal oxide photoelectrode systems. Hence, a comprehensive understanding of surface and bulk defects is detrimental to identifying such processes that cause loss of photogenerated carrier populations[53]. These sorts of kinetic processes define the charge utilization efficiencies in PEC OWS reactions along with photoreduction and photooxidation-related photocorrosion of the photoelectrode materials[54], [55], [56]. Therefore, probing of fast interfacial carrier dynamics is an essential step in understanding the processes that govern the activity of photoelectrodes. Consequently, interfacial electron and hole trapping processes can be realized with combined time-resolved experiments that can cover a wide time range that spans from a few fs to a s[57].

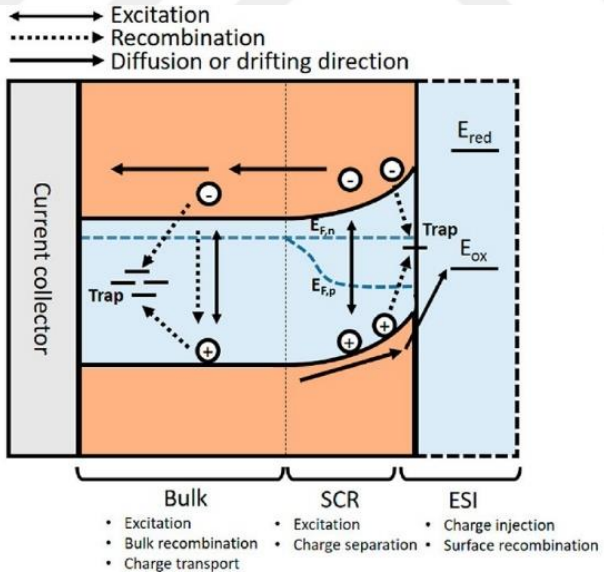

Figure 1.7: Excitation, charge transport, trapping, and recombination processes of photogenerated charge carriers at a photoanode–electrolyte interface. SCR is the space charge region, and ESI is the electrolyte–semiconductor interface[52].

The kinetics that lead to the utilization of $2h^+$ and $2e^-$ in OER and HER, respectively, occur also at ms-s timescales[58], [59]. The elementary reaction steps of OER that release $4H^+$ and $2O_2$ along with the single step $4H^+$ reduction to form $2H_2$ under acidic conditions,

as well as the alkaline intermediates can be tracked with time-resolved and frequency-resolved PEC methods such as ms transient photocurrent (TPC) measurements and intensity-modulated photocurrent spectroscopy (IMPS) [60], [61]. Especially in the case of the p-type/n-type heterojunction systems, both reaction kinetics might occur on the electrode surface upon illumination, depending on the potential range of operation[62]. Therefore, addressing the surface and interface reaction kinetics of heterojunction systems stands out as an experimentally challenging but important issue. Comprehension of the mechanisms that cause the poor stability and activity of photoelectrode systems can be made possible through such investigations.

1.6 The Aim of the Thesis

The thesis intends to study the charge carrier dynamics of photocathodes through a combination of time-resolved investigations with structural characterization techniques and PEC performance tests to understand the connections between the material structure, charge carrier behavior, and performance. In the first part of the thesis (Chapter 3), ultrafast charge carrier dynamics of compositionally manipulated CBO photocathodes were screened via *ex situ* and *in situ* ultrafast TAS experiments. The effects of different types of intrinsic cation vacancies on the ultrafast processes that govern the photocurrent generation were studied through cation-deficient photocathodes. Overall, this chapter aims to reveal how varying types of defects hinder the hole utilization dynamics in CBO photocathodes and retard the PEC HER activity to different extents.

In the second part of the thesis (Chapter 4), interfacial charge carrier dynamics of bare Cu_2O and Cu_2O-based heterojunction photocathodes were investigated at ms resolution via potential-dependent TPC experiments together with surface- and bulk-sensitive characterization methods and PEC performance measurements. Throughout this chapter, the effects of the TiO_2 underlayer on the interfacial charge transfer dynamics of Cu_2O-based heterojunction photocathodes were studied. The research aims at unraveling different interfacial charge trapping and accumulation tendencies of both single and heterojunction systems. Alongside these goals, the influence of the electrodeposition duration on the photoactivity of the Cu_2O layer was also studied, and a correlation between the photocathode stability and longer electrodeposition duration was sought due to enhanced structural integrity of the Cu_2O at longer electrodeposition durations.

Chapter 2:
EXPERIMENTAL METHODS

2.1 Synthesis Techniques

2.1.1 Spin Coating

Spin coating is a simple and widely used technique in thin film fabrication. The technique involves the dropping of a small amount of resin that gets spread with the spinning of the substrate at high rates. As a result of the spinning motion, a thin layer of film forms on the surface of the substrate. The film generally dries with the help of the volatile solvents and can also be heat-treated to reach its final form. One of the most significant advantages of this technique is the thickness control depending on the spinning rate, resin concentration, and number of revolutions[63].

CBO photocathodes were synthesized via the spin coating method[64]. Ideally, $Cu(NO_3)_2 \cdot 2.5H_2O$ (Sigma–Aldrich, ACS, 98%) and $Bi(NO_3)_3 \cdot 5H_2O$ (Sigma–Aldrich, ≥99.99%) were dissolved in 2-methoxyethanol (Sigma–Aldrich, ≥99.0%) separately to achieve a concentration of 0.1 M per solution. The resulting precursor solutions were then mixed at a 1:2 volume ratio to achieve a 1:2 Cu:Bi ratio. In this study, the synthesis of cation vacancy-bearing Cu-deficient and Bi-deficient photocathodes was achieved by changing the molarity of the precursor solutions by ±10% while keeping the volume ratio the same. The resulting precursor solution mixtures were then dropped onto precleaned 0.83 cm × 0.83 cm fluorine-doped tin oxide (FTO)-coated soda lime glass substrates (Osilla TEC 8, 2.2 mm thick). The FTO substrates were cleaned in a sonicator bath at room temperature by placing them in ethanol, acetone, and deionized water for 10 minutes each. After that, the substrates were dried in a drying oven at 60 °C for an hour. Following the dropping of the precursor solution mixture, the substrates were spun in a spin-coater at 1200 rpm for 10 seconds with a 3-second acceleration duration for wet thin-film formation on the FTO surface. The wet samples were later annealed in a muffle furnace at 500 °C for 20 min after each spin-coating cycle and then subjected to a final annealing process for 3-h after the last cycle. The whole synthesis process is summarized in Figure 2.1. The thickness and homogeneity of the photocathodes were optimized by changing the number of spin-coating cycles.

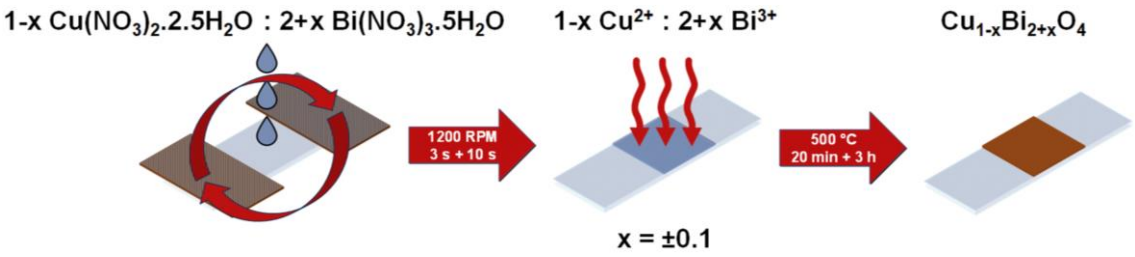

Figure 2.1: Synthesis scheme of thin-film CBO photocathodes.

2.1.2 Electrodeposition

Electrodeposition is a technique based on the use of electrochemical redox reactions to deposit metallic or semiconductor thin films onto a conductive substrate. In such a technique, the substrate is connected to the circuit as a cathode, which acts as the negatively charged electrode, attracting the positively charged metal ions from the electrolyte to reduce and deposit them on the surface electrochemically. In the meantime, the anionic species within the electrolyte go through the oxidation process at the anode. Eventually, the crystalline deposit of the desired material is obtained on the surface of the cathode substrate[65].

The synthesis of Cu_2O thin films is done using the cathodic electrodeposition method. For this purpose, an alkaline electrolyte solution is prepared by first dissolving 0.4 M $CuSO_4.5H_2O$ (ISOLAB, ≥99.0%) and 12.1 M (S)-lactic acid (ISOLAB, about 90%) in deionized water in the relevant volume amounts. This blue acidic solution is then placed in a 40 °C water bath, and the pH value of the solution is fixed at 12.00 by adding 5 M NaOH (ISOLAB, ≥99.0%) solution dropwise. When the pH value is fixed at 12.00, the color of the solution turns dark blue, and the solution is kept in the dark overnight to reach pH stability. The next day, the pH value is stabilized at 12.00 by re-checking the pH in a 40 °C water bath and adding a few more drops of the NaOH solution if necessary. Once the pH is permanently set, the solution becomes ready to be used as an electrolyte for the electrodeposition.

The FTO-coated glass substrates are prepared and cleaned using the same method described in section 2.1.1. During the electrodeposition method, in order to transmit the current applied to the substrate with the alligator mouth crocodile cable, the conductive copper tape is attached to the side of the FTO-coated surface of the substrates that will

not contact the electrolyte, and the connection of the conductive FTO layer to the crocodile is made through this tape and immersed in the electrolyte in this way. Afterward, the surfaces of the substrates are temporarily covered with adhesive Teflon tape, leaving an area of approximately 1 cm^2 exposed for electrodeposition.

For the electrodeposition, the electrochemical cell is placed in a water bath, and a certain amount of electrolyte is added. It is ensured that the electrolyte level is below the water level of the surrounding bath to prevent the formation of a heat gradient in the electrolyte volume. The electrolyte temperature equilibrates with the bath temperature at 40 °C. The electrodeposition setup with a three-electrode configuration is installed in the electrochemical cell, and the connections of the BioLogic SP200 potentiostat and the Ag/AgCl reference electrode, working electrode, and platinum counter electrode are made using crocodile cables. Once the setup is ready, the open circuit potential (OCP) is waited to come to steady-state. Following the stabilization of OCP, -0.421 mA of cathodic current is applied to the cell for an hour with the chronopotentiometry technique. While a continuous current is applied to the substrate during the electrodeposition process, the potential change is monitored over time. In the end, the electrodeposited Cu_2O samples are washed with deionized water and dried under N_2 flow.

2.1.3 Hydrothermal

Hydrothermal synthesis originates from the volcanic hydrothermal vents found in the ocean ridges. Although this method has been under development for more than 150 years, it is simply based on the controlled reaction of inorganic substances dissolved in water or other solvents (also known as solvothermal) at high pressures and temperatures in a Teflon-lined steel autoclave system. Along with these parameters, the pH, concentration, and reaction time of the reactants play an essential role in achieving crystalline inorganic solid products. At the end of a hydrothermal reaction, the products are washed out of impurities, and the solvent is evaporated to obtain pure and dry crystalline products[66].

The synthesis of the reference pristine CBO powder was carried out using a hydrothermal method[67]. For this purpose, $Cu(NO_3)_2 \cdot 2.5H_2O$ was dissolved in 25 mL of ethanol (ISOLAB, ≥99.9%), and $Bi(NO_3)_3 \cdot 5H_2O$ was dissolved in 5 mL of acetic acid (Sigma–Aldrich, ≥99%) to achieve 0.04 M and 0.4 M solutions, respectively. The

obtained precursor solutions were mixed to obtain a 1:2 Cu:Bi ratio. The pH of the reaction mixture was adjusted to 14 by the dropwise addition of 5 M NaOH (ISOLAB, ≥99.0%). The resulting reaction mixture was then transferred into a 100 mL Teflon-lined steel autoclave and kept in an oven at 120 ℃ for 12 hours. The product was first washed with ethanol and then with water in a centrifuge three times each to remove any impurities. Later, the washed product was dried in a vacuum oven at 80 ℃ for 12 hours.

2.2 Structural Characterization Techniques

2.2.1 Field Emission Scanning Electron Microscopy

Field emission scanning electron microscopy (FESEM) is a type of electron microscope that uses a field emission gun to generate electrons. A field emission gun generally generates a thousand times higher emission compared to a tungsten filament. Generated electrons at the gun are focused and monochromatized with the use of metallic apertures and magnetic lenses. This electron beam is targeted toward the sample. The electrons that reach and interact with the sample are collected through different types of detectors, and eventually, a highly magnified image of the material is generated[68].

In this study, FESEM measurements were taken with a Zeiss Ultra Plus Field Emission Scanning Electron Microscope at an acceleration potential of 20 kV. Cross-sectional FESEM images were used to estimate the film thicknesses of CBO and Cu_2O thicknesses.

2.2.2 Energy-Dispersive X-Ray Spectroscopy

The ionization of a core electron as a result of the electron bombardment from the field emission gun of an FESEM results in the decay of an upper shell electron to fill the electron hole generated with the ionization. Following this, either an auger electron can be produced, or fluorescent X-rays are emitted to reach an energy equilibrium within the system. The probing of these characteristic fluorescent X-rays is called energy-dispersive X-ray spectroscopy (EDX). EDX is an element-selective method and is very effective in the chemical probing of the bulk of thin-film samples[69].

In this study, EDX measurements were also taken with a Zeiss Ultra Plus Field Emission Scanning Electron Microscope at an acceleration potential of 20 kV. EDX measurements were used to probe the bulk chemical compositions of CBO photocathodes to estimate their cationic deficiencies.

2.2.3 X-Ray Photoelectron Spectroscopy

X-ray photoelectron spectroscopy (XPS) is a surface and element-sensitive characterization technique based on the ionization of core electrons under X-ray bombardment. Following this ionization, X-ray fluorescence and Auger decay processes can also be observed, as described in Figure 2.2. In XPS, samples are probed with soft X-rays that have photon energies lower than 6 keV. Once an X-ray photon interacts with a core electron, its energy gets completely transferred to the electron. If this energy is greater than the binding energy (BE) of the core electron, the remainder of the energy equals the kinetic energy (KE) of the emitted electron plus the work function (Φspec) of the spectrometer, which is a constant value. This equality is given by Eq. 2.1.

$$h\nu = BE + KE + \Phi_{spec} \qquad (2.1)$$

BE of the elements that are included in the analyzed samples can be determined through Eq. 2.1. Since the BE of an electron is a specific property of that material, the information obtained from XPS becomes X-ray source independent and therefore makes it a robust technique in understanding elemental and ionic properties of all kinds of substances[70].

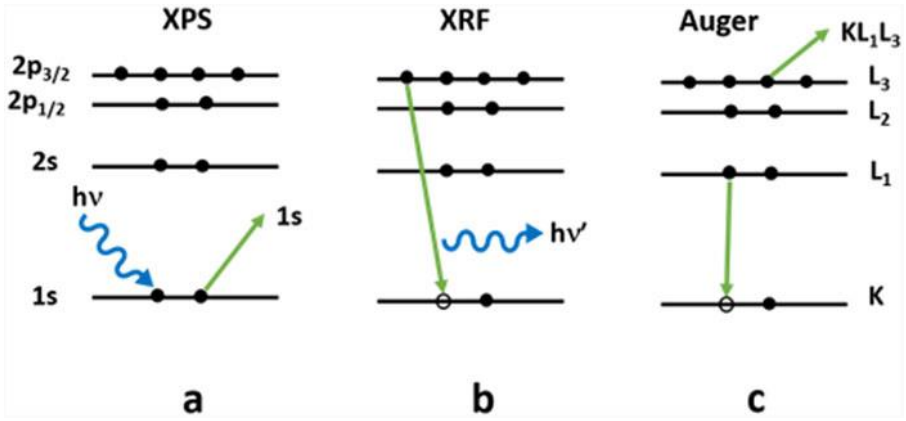

Figure 2.2: X-ray bombardment-related processes that occur at surfaces: (a) emission of a photoelectron, (b) x-ray fluorescence, and (c) emission of an Auger electron[70].

In this study, XPS data were collected via a Thermo Scientific K-Alpha X-ray photoelectron spectrometer with Al K_α radiation (hν=1486.7 eV). The obtained binding energies were subsequently corrected according to the C 1 s binding energy of 284.5 eV. All individual XPS spectra were normalized to the background with the lowest binding energy. Spectral deconvolutions were carried out using CasaXPS software.

In the first part of the thesis, XPS measurements were used to characterize the cation-deficient surfaces of CBO photocathodes. In the second part, oxidation state of the Cu species on the Cu_2O-based photocathodes surfaces were also identified using XPS. Additionally, the possibility of the differences in terms of oxygen vacancy amounts in bare Cu_2O and heterojunction photocathodes were also discussed based on the XPS results.

2.2.4 X-Ray Diffraction

Interaction of X-rays with matter can result in absorption, scattering, and diffraction of X-ray photons. X-ray diffraction (XRD) analysis relies on the diffraction of X-rays from the periodically ordered crystal lattices of materials. As described by Bragg in 1913, periodically diffracted X-ray beams form constructive interference patterns that eventually give rise to the XRD spectrum of a material. The technique is an effective tool for understanding the crystal structure of solids as well as crystallite sizes and lattice strain values through further analysis of lattice parameters obtained from XRD patterns[71].

XRD measurements of the photocathodes were performed using a Bruker D2 Phaser diffractometer. During the measurements, a Cu K_α radiation source was used at a 10 kV beam voltage and 30 mA beam current. The qualitative evaluation of the XRD patterns was performed via Bruker DIFFRAC.EVA software. Gaussian crystallite size and lattice strain values were estimated from the analyses of the XRD profiles using the fundamental parameters approach (FPA) through Bruker DIFFRAC.TOPAS software.

XRD was used extensively to understand and estimate the crystal properties of both cation-deficient CBO photocathodes and Cu_2O-based photocathodes in terms of degree of crystallinity, crystallite sizes, and lattice strain values.

2.2.5 Doppler-Broadening Spectroscopy of Positron Annihilation

The annihilation of an electron with a positron results in the emission of two gamma-ray photons with an energy of 511 keV due to a Doppler shift in the energy spectrum caused by the momentum projection along the emission direction[72]. This Doppler broadening spectrum of positron annihilation is measured via Doppler broadening spectroscopy (DBS). The DB spectrum is divided into six regions. In the scope of our work, two areas of the DB spectrum are significant: the center and the wing areas of the 511 keV annihilation peak. The parameters S (sharpness) and W (wing) are established as the ratio of the areas of the center or the wings to the total peak area[72], [73]. The positron annihilation at the vacancy defects causes an increase in the S-parameter and a decrease in the W-parameter, corresponding to low and high momentum values of the valence and core electrons, respectively. Although the S and W parameters are not absolute, the central region width of the 511 keV annihilation peak is calibrated to 0.5 for the S-parameter and 0.05 for the W-parameter using a Si crystal. DBS measurements in this study were performed using a Canberra GC2519 HPGe detector and an ORTEC572A amplifier with an ORTEC ASPEC-927 multichannel analyzer. Subsequently, the SP-SE program was used to estimate the S- and W-parameters from the obtained DB spectra[74]. The incident positron energies were varied from 0.2 to 13 keV to achieve average probing depths that cover the pronounced thicknesses of the CBO photocathodes. The corresponding average positron penetration depth (z) values are calculated from Eq. 2.2:

$$z = \frac{40}{\rho} E_{+}^{1.6} \qquad (2.2)$$

where ρ is the density of the film in g/cm^3 and E_+ represents the incident positron energy in keV[72], [75], [76]. During DBS measurements, surface effects are expected to occur at low incident positron energies, specifically below 5 nm depth, due to electron pile-up and backscattering events. Therefore, this discussion does not encompass delineating the very front surface region. The rest of the incident positron energies cover a film thickness of approximately 285 nm, and these data points are linearly fitted.

In the first part of the thesis, DBS plays a crucial role in characterizing the varying amounts and types of vacancy defects (V''_{Cu} and V'''_{Bi}) through the calculation and comparison of S and W parameters.

2.2.6 Raman Spectroscopy

Raman spectroscopy is an effective tool for understanding the structure of thin film materials. It is based on the Raman scattering phenomenon, which occurs when the energy of the scattered light becomes higher than the incoming light. This energy shift, also called the Stokes-Raman shift, occurs through the interaction of light with the vibrational modes of chemical bonds found within the material. At rough surfaces, this scattering intensity can be amplified with the higher number of electrons oscillating perpendicular to the surface, causing plasmon resonance. The plasmon resonance causes the Raman scattering to occur at a higher intensity and, therefore, allows the detection limit to get lower and signal intensity to get higher. The Raman spectroscopy that includes this kind of enhancement in the signal is named surface-enhanced Raman spectroscopy (SERS). SERS finds its applications in various fields, including thin film characterization and catalysis[77], [78].

In this study, Raman spectra of the photocathodes were measured under a Renishaw inVia Microscope at an excitation laser wavelength of 532 nm. The Raman spectrum was calibrated to the signature peak of Si at 520.7 cm^{-1} using a Si slab. Both parts of the thesis include Raman spectroscopy to identify the changes in the bond symmetries of the photocathodes regarding the structural changes that have been applied.

2.2.7 UV-Vis Reflectance/Absorbance Spectroscopy and Tauc Analysis

Ultraviolet-visible (UV-Vis) spectroscopy is a common and robust technique in understanding the light-matter interactions within the UV-vis spectral range (UV: 200-380 nm and vis: 380-750 nm). In this technique, reflected, transmitted, or absorbed light intensity is measured as a function of incoming photon energy in wavelengths to obtain a reflectance, transmittance, or absorbance spectrum. The interactions measured within the scope of UV-vis spectroscopy are the VB electrons of subjected substances. Therefore, this technique is also called “electronic spectroscopy”[79].

In Tauc analysis, the absorbance spectrum of the subjected system is converted to a Tauc plot, $(\alpha h\nu)^2$ vs. $h\nu$ where α is the absorption coefficient calculated from the absorbance values obtained during the UV-vis spectroscopy measurements, h is the Planck’s constant, and ν is the frequency of UV-vis photons. This plot is called the direct

band gap Tauc plot, and it is used to determine the optical band gap of semiconductor materials[80].

In this study, UV–vis spectra of the thin films were collected via a Shimadzu UV-3600 UV–vis-NIR spectrophotometer in reflectance mode. The reflectance spectra were later converted to absorbance using the Kubelka–Munk transformation theory. Tauc analysis of the photocathodes was performed by considering the direct band gap transition of CBO, Cu_2O and TiO_2. The UV-vis spectra was obtained from all three different materials studied throughout this thesis to comprehend their ground state light absorption characteristics and to estimate the optical band gap energies through Tauc analysis.

2.3 Photoelectrochemical Tests

2.3.1 The PEC Setup

All PEC tests were conducted with a three-electrode configuration inside a quartz cell. The synthesized CBO and Cu_2O photocathodes were used as working electrodes alongside the graphite counter and Ag/AgCl (sat. KCl) reference electrode (Pine Research). All measurements for CBO photocathodes were performed in an alkaline 0.1 M NaOH (ISOLAB, ≥99.0%) electrolyte at pH 13 purged with O_2 as an electron scavenger. O_2 purging was continuously applied during almost all PEC tests. On the other hand, Cu_2O photocathodes were measured in neutral 0.1 M Na_2SO_4 (ISOLAB, ≥99.5%) electrolyte at pH 7 without an electron scavenger. A Newport Corp. - Oriel Instruments solar simulator with a 100 W Xe lamp was used to obtain 1.0 sun, 1.5G AM output. The PEC cell was positioned at a 22 cm distance to achieve an illumination intensity of 100 mW/cm^2 at the working electrode surface. During all PEC tests for CBO, the front side of the photocathodes was illuminated. In Cu_2O studies, due to the existence of TiO_2 underlayer back illumination, measurements were also carried out. A BioLogic VSP-300 potentiostat was used during all PEC tests. The conversion of the measured potential values from V vs. Ag/AgCl to V vs. RHE (reversible hydrogen electrode) was performed using the Nernst equation (Eq. 2.3):

$$E_{RHE} = E_{Ag/AgCl} + 0.059 \times pH + E^{\circ}_{Ag/AgCl} \qquad (2.3)$$

In the equation, E_{RHE} is the applied potential versus RHE, $E_{Ag/AgCl}$ is the applied potential versus Ag/AgCl reference electrode, and $E^{\circ}_{Ag/AgCl}$ is the standard electrode potential of Ag/AgCl (sat. KCl) reference electrode used during the experiments (0.199 V vs. RHE)

2.3.2 Linear Sweep Voltammetry

In linear sweep voltammetry (LSV), the current response of an electrochemical system is measured as a function of potential. A potential range is swept with potential steps, and the corresponding current is recorded over time. The potential scanning rates can differ from 10 mV/s to about 1000 V/s[81].

LSV measurements in this study were performed under chopped light conditions. A homemade chopper with 3-second chopping intervals was used. The potential scanning rate was set to 10 mV/s. The current response was recorded as a function of the applied potential (φ) and later converted to the current density (j) by dividing the current (i) by the photocathode geometrical surface area. Chopped LSV measurements were also repeated with front and back illumination in 30 min of N_2-purged electrolyte under constant purging conditions to investigate the charge accumulation on the surface of the photocathodes.

Throughout the thesis, chopped LSV scans play one of the most vital roles in assessing the PEC activity and stability of both photocathodes. Additionally, the anodic and cathodic charge accumulation spikes that occur at the light switch-ons and cut-offs are observed carefully to understand the potential-dependent charge trapping tendencies of the CBO and Cu_2O-based photocathodes.

2.3.3 Open Circuit Potential

Open circuit potential (OCP) is the built-in potential that exists between the working electrode and the reference electrode of an electrochemical system at steady-state[81]. In PEC systems, the change of OCP (ΔOCP) under illumination with respect to dark conditions can be measured with chronopotentiometry (CP) to understand the photovoltage response of the system.

In this study, OCP was measured via CP under dark and front illumination conditions. ΔOCP values were then calculated by subtracting the OCP values measured under dark conditions from the OCP values obtained under front illumination.

In the first part of the thesis, OCP measurements are used to estimate the differences between the Cu- and Bi-deficient CBO photocathodes in terms of photovoltage charging and discharging behaviors that might stem from the different amounts and types of cation vacancies.

2.3.4 Photoelectrochemical Impedance Spectroscopy

Sinusoidal alteration of applied potential on a PEC system results in an alternating current response that carries valuable information through its amplitude and phase angle. The term impedance can express this alternating potential-current relation. Impedance consists of a combination of specific resistance and specific resistance depending on the circuit model applied. Therefore, scanning of a potential modulation frequency range that can span from 100 μHz to 1 MHz gives a frequency-resolved impedance spectrum. PEC impedance spectroscopy (PEIS) stands out as an effective tool for probing essential properties of a PEC system, such as charge transfer resistance, interfacial capacitance, mass transfer limitations, and reaction kinetics with high precision[81].

In this thesis, PEIS measurements were taken under dark and front-illuminated conditions at a potential amplitude of 10 mV and between 100 kHz and 100 mHz. The obtained data were plotted as Nyquist plots and then Z-fitted with a Randle's circuit equivalent circuit model. The Z-fitting results were later used to estimate the solution resistance (R_S), charge transfer resistance (R_{CT}), and capacitance (C or Q depending on the circuit element used) properties of Cu- and Bi-deficient CBO photocathodes. Such properties are correlated with the defective nature of the CBO photocathodes.

2.3.5 Mott-Schottky Analysis

Mott-Schottky (MS) analysis is a valuable technique for the characterization of photocathode/electrolyte interfaces in terms of flatband potential (φ_{fb}) and acceptor density (N_A). In MS analysis of p-type materials, the potential-current relation is again monitored just like in PEIS but with a staircase potential sweep throughout the defined

potential and frequency ranges. The resulting C_s^{-2} vs. E curves plotted at specific frequencies include the φ_{fb} and N_A properties at the x-axis intercept and slope, respectively[81].

MS analyses in this study were also performed under dark and front-illuminated conditions at 1.075 kHz to compare the φ_{fb} and acceptor density N_A values of the photocathodes. Both values are obtained from the linear fitting of the negative slope of the MS data via the MS equation (Eq. 2.4).

$$\frac{1}{C^2} = \left(\frac{2}{\varepsilon_r \varepsilon_0 A^2 e N_A}\right)\left(\varphi - \varphi_{fb} - \frac{k_B T}{e}\right) \qquad (2.4)$$

where $\frac{1}{C^2}$ is the reciprocal of the squared capacitance, ε_r is the relative permittivity of $CuBi_2O_4$ (80 at 298 K)[20], ε_0 is the vacuum permittivity (8.85×10^{-12} F/m), A is the surface area of the photocathode, e is the electron charge (1.6×10^{-19} C), N_A is the acceptor density in a p-type photocathode, φ is the applied potential, φ_{fb} is the flat band potential, and k_B is the Boltzmann constant (1.38×10^{-23} $m^2.kg/(s^2.K)$, and T is the temperature in K.

In the first part of the thesis, Mott-Schottky analysis is primarily used to estimate the φ_{fb} and N_A properties of Cu- and Bi-deficient CBO photocathodes. However, the capacitive differences that form upon illumination are also well-investigated and discussed through measurements conducted under dark and illuminated conditions for both CBO photocathodes.

2.3.6 Incident Photon-to-Current Efficiency

Incident photon-to-current efficiency (IPCE) is a performance parameter in PEC systems that describes the wavelength dependence of quantum efficiency[15]. Such a parameter is essential in expressing the performance limitations of a photoelectrode that stem from photon energies under illumination.

IPCE measurements in this study were performed by placing the three-electrode quartz cell in front of the Newport Corp. - Oriel Instruments 300 W Xe lamp-coupled monochromator system. The experiments were conducted in an alkaline 0.1 M NaOH (ISOLAB, ≥99.0%) electrolyte at pH 13 purged with O_2 as an electron scavenger. Only

in these measurements, O_2 purging was not continuously applied for experimental reasons. Later, IPCE values were calculated with Eq. 2.5:

$$\text{IPCE} = \frac{1240\ (\text{V.nm}) \times j_\lambda\ (\text{mA/cm}^2)}{\lambda\ (\text{nm}) \times I_\lambda\ (\text{mW/cm}^2)} \times 100 \qquad (2.5)$$

where j_λ is the photocurrent density observed under illumination and I_λ is the optical intensity of the monochromatized light at wavelength λ. The optical power spectrum of the monochromator output is characterized by a Newport Corp. - Oriel Instruments UV-enhanced Si detector.

In the first part of the thesis, potential-dependent IPCE measurements are employed to calculate the photocurrent generation efficiencies of cation-deficient CBO photocathodes. In addition to that, the wavelength dependence of the IPCE curves were also discussed within the context of charge trapping tendencies of cation vacancies.

2.4 Time-Resolved Methods

2.4.1 Transient Absorption Spectroscopy

Transient absorption spectroscopy (TAS) is an ultrafast pump-probe-based technique that allows the screening of charge carrier dynamics of photoelectrode materials within the fs-ns timescales. In TAS, the photoelectrode material is excited by a periodically chopped pump pulse. Following the periodic pump excitation and relaxation instances, a weaker continuum pulse interacts with the same spatially overlapping area on the sample with a time delay, as shown in Figure 2.3. This allows the calculation of the differential absorption spectrum of the photoelectrode material with respect to its ground-state absorption. As the time delay between the pump pulse and the probe pulse is changed and differential absorption spectra are recorded at different delay times, the transient behavior of the photogenerated charge carriers can be observed[82]. As a three-dimensional measurement, a TAS measurement includes wavelength, delay time, and differential absorption components. A transient change in one of these parameters as a function of the other two carries information about crucial ultrafast processes that influence the performance of photoelectrode materials. Therefore, *in situ*, TAS experiments hold

especially great importance in understanding the ultrafast charge carrier dynamics of PEC systems.

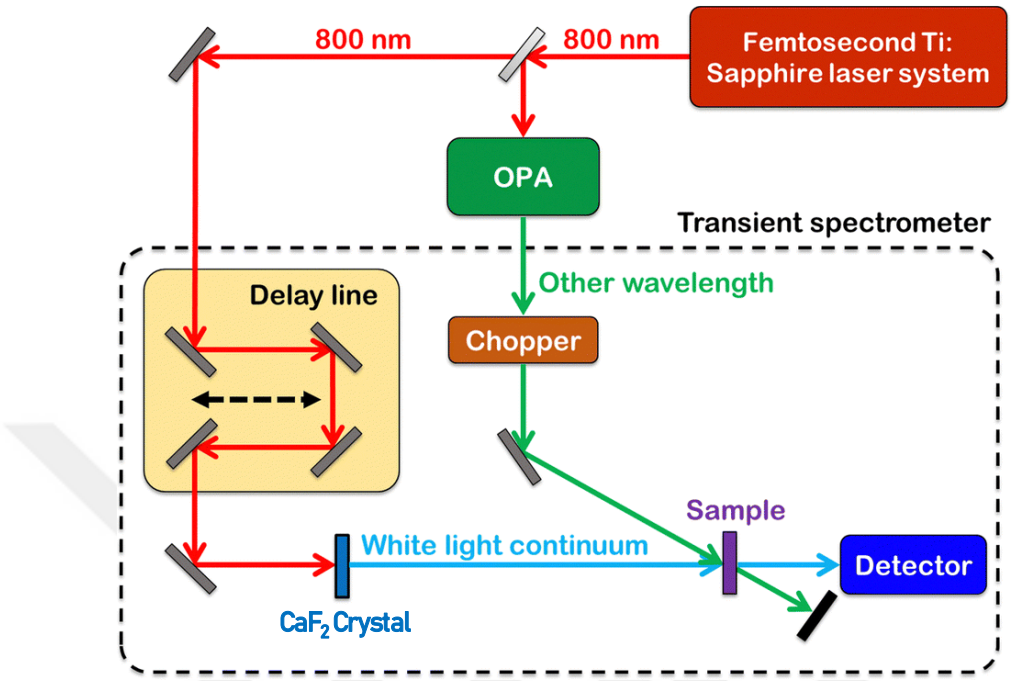

Figure 2.3: Scheme of a typical ultrafast TAS setup[83].

In this study, TAS measurements were conducted with a regeneratively amplified femtosecond Ti^{3+}:Sapphire laser (MKS Spectra-Physics Spitfire Ace), operating at a repetition frequency of 1 kHz and outputting 120-fs pulses at 800 nm. The output of the amplifier is split into two beams, one of which is used to excite an optical parametric amplifier (Light Conversion TOPAS) and generate the pump at 320 nm. The other beam is used to create a white light continuum (WLC) in a CaF_2 crystal, spanning the 380-800 nm range. The CaF_2 crystal is constantly moved on an automated stage throughout the measurements to prevent overheating of the slab.

The incident pump beam on the thin film photocathode sample was modulated periodically with a chopper operating at 500 Hz. This enables the measurement of the unpumped ($A_{unpumped}$) and pumped (A_{pumped}) values of the photocathode sample absorbance. The resulting difference in absorbance (ΔA) is determined from Eq. 2.6 given below:

$$\Delta A = A_{pumped} - A_{unpumped} \qquad (2.6)$$

Incident pump fluences were controlled throughout the TA experiments with the use of a natural density (ND) filter and were also calculated via Eq. 2.7:

$$\text{Fluence} = \frac{P_{average}}{f_{rep} \times \pi\omega^2} \qquad (2.7)$$

Here, $P_{average}$ is the average optical power of the incident pump at 320 nm, f_{rep} is the repetition rate (1 kHz), and ω is the pump spot size (550 μm). ω value is measured using the knife edge method.

The TA spectra and kinetic measurements were conducted inside the commercial pump-probe spectrometer system (Ultrafast Systems HELIOS). The probe beam is split into two parts with an ND filter as the "reference" and "signal", which are sent to separate fiber-coupled detectors of a multichannel spectrometer. The spectral resolution of the spectrometer within the WLC range was 1.5 nm. Pump-probe delays were created by an automated mechanical delay stage. Chirp correction, time zero (τ_0) adjustment, and kinetic fitting of the data were conducted in Ultrafast Systems Surface Xplorer software. Two exponential decay parameters (τ_1 and τ_2) were chosen to fit the TA kinetics within the fs-ps time range. The kinetic fitting function used by the software to fit a kinetic trace of a desired wavelength with a sum of convoluted exponentials is given in Eq. 2.8:

$$S(t) = e^{-\left(\frac{\tau-\tau_0}{\tau_p}\right)} \times \sum_i A_i e^{-\left(\frac{\tau-\tau_0}{\tau_i}\right)}, \qquad \tau_p = \frac{IRF}{2\cdot\ln 2} \qquad (2.8)$$

where τ_0 is time zero, τ_p is pulse width, A_i are amplitudes, τ_i are decay time constants, and IRF is the instrument response function (FWHM).

In situ TAS measurements were conducted with a three-electrode system inside a 1 cm × 1 cm quartz UV cuvette filled with 30 min of O_2-purged 0.1 M NaOH electrolyte at pH 13, as shown in Figure 2.4c. The three-electrode system included the CBO photocathode as the working electrode, a small Ag/AgCl reference electrode that fit the entrance of the quartz cuvette, and a Pt coil wrapped around a Cu wire as the counter electrode. A Pt counter was chosen due to the experimental complications caused by the small entrance of the quartz cuvette. The miniature cell was placed inside the transient absorption spectrometer and connected to a BioLogic SP-200 potentiostat. The whole *in*

situ TAS setup is shown in Figure 2.4a, and a close-up image of the setup is provided in Figure 2.4b.

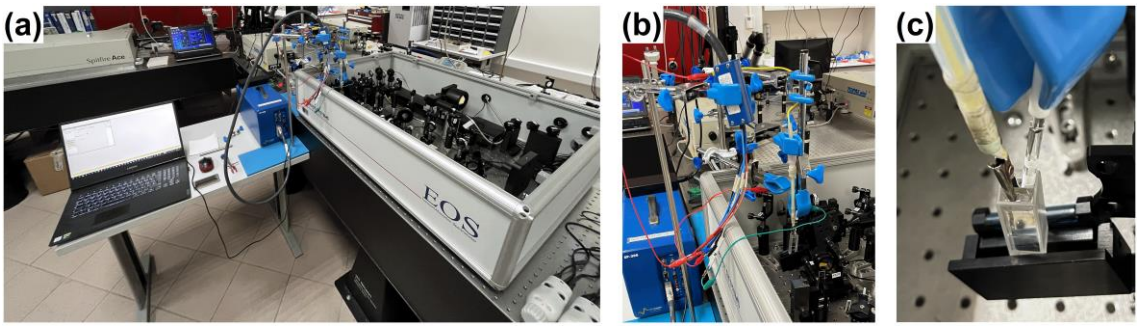

Figure 2.4: (a) *In situ* TAS setup, (b) close-up image of the setup, and (c) a three-electrode miniature cell inside the spectrometer.

Ultrafast TAS experiments form the core of the first part of the thesis by allowing the screening of the charge carrier dynamics of Cu- and Bi-deficient photocathodes. Such measurements give access to the three-dimensional "images" of the charge carriers within the CBO system with visible wavelength, ultrafast time, and ΔA forming the three dimensions. Moreover, *in situ* potential-dependent and pump fluence-dependent TAS measurements provide an extra variable that can be used to understand the charge carrier behavior observed in cation deficient CBO photocathodes. Lastly, exponential fitting of the two-dimensional TA decay kinetics is used to provide a numerical understanding for the effects of cation vacancies on the polaronic charge trapping, recombination, and transport dynamics.

2.4.2 Transient Photocurrent

Transient photocurrent (TPC) is an effective method to probe the transient current response that is generated following the interaction of a PEC system with a short light pulse. The resulting transient photocurrent response contains information about interfacial trapping, accumulation, recombination, de-trapping, and the reaction of photogenerated charge carriers[15], [60].

In this study, TPC measurements were carried out in chronoamperometry (CA) mode with the PEC setup described for the Cu_2O photocathodes. As a pulsed light source, instead of a solar simulator, a 60 W white LED light was used. During the experiments, the LED light was programmed to produce a 200 ms pulse per 10 s. Data collection time

steps during the measurements were chosen as 0.4 ms. Potential-dependent TPC measurements for the Cu_2O photocathodes were done cathodically from 0.5 V to 0.0 V with 0.1 V potential intervals that last 10 s. This way, the LED light's pulse generation frequency was matched with the potential application duration. 10 s intervals were explicitly chosen as the required time for the system to return to a steady state after the interaction with a light pulse. The TPC data were later shifted on the time axis to match and compare the systems' response to the light pulses at different applied potential values.

In the second part of the thesis, ms resolution potential-dependent TPC measurements are extensively utilized to understand the interfacial charge trapping, accumulation, utilization, de-trapping, and dissipation events that occur at the interfaces of Cu_2O-based photocathodes. The periodic photocurrent oscillations also named as "wiggles" are also observed within the TPC data collected from the bare Cu_2O and TiO_2/Cu_2O heterojunction systems.

Chapter 3:
ULTRAFAST CHARGE TRANSPORT DYNAMICS OF $CuBi_2O_4$ PHOTOCATHODES

3.1 Introduction

In recent years, due to the abundance of n-type materials as suitable photoanodes, which are also the main bottleneck of solar water splitting, research on the ultrafast dynamics of these materials has surpassed research on p-type photocathodes[4], [14], [15], [84], [85]. Nevertheless, the enigmatic nature of photocathodes requires further ultrafast spectroscopic investigations to determine the reasons behind their poor reduction performance[86], [87], [88]. To date, among the most promising candidates for a photocathode in solar water splitting has been Cu-based metal oxides, with Cu_2O being the most studied one[12]. Nonetheless, since its first proposal as a visible-light-responsive porous photoelectrode, tetragonal CBO has attracted increasing amounts of attention for more than a decade as a more stable alternative[18].

Herein, we investigate the ultrafast transport dynamics of holes in CBO thin films by manipulating their p-type character by tuning cation vacancies and address the mechanisms that are related to the cation vacancies which cause the loss of carrier populations prior to charge extraction. The use of *in situ* potential-dependent ultrafast transient absorption spectroscopy (TAS) enables the direct assignment of the spectral features of the CBO system in the visible region to hole absorption (HA) and hole polaron absorption (HPA)[89], [90] . Additionally, pump fluence-dependent TAS investigations revealed the HA and HPA saturation tendencies of the VB hole populations. The experimental results also demonstrate that different amounts and types of defects, such as Cu^{2+} and Bi^{3+} vacancies (V''_{Cu} and V'''_{Bi}), influence the polaronic trapping tendencies of the VB holes, which leads to a significant difference in the PEC HER performances of CBO films.

3.2 Experimental Methods

Synthesis details of CBO have been described in sections 2.1.1 and 2.1.2. Structural characterization experiments carried out on CBO photocathodes include FESEM, EDX,

XPS, XRD, DBS, Raman, and UV-vis spectroscopy. The experimental details of structural characterization techniques used in this chapter are described under section 2.2. The PEC performance tests carried out on CBO photocathodes consist of LSV, IPCE, OCP, MS analysis, and PEIS. These PEC experiments are described under section 2.3. Lastly, *ex situ* and *in situ* TAS experimental details are given in section 2.4.1.

3.3 Results & Discussion

The formation of tetragonal CBOs with similar thicknesses, homogeneities, and light absorption characteristics are all crucial for comparing the impacts of cationic vacancies and associated PEC performances. Therefore, a wide range of structural characterization techniques were utilized to understand and confirm the structural properties of CBOs with cationic vacancies.

The Cu:Bi atomic ratio estimated from the EDX measurements (Table 7.1) and Figure 7.1a corroborate the compositional differences between the two cation-deficient CBOs. Compared to the reference pristine CBO powder that was synthesized via the hydrothermal method, the Cu:Bi ratio in the thin-film CBOs deviates from that of the pristine CBO. The Cu:Bi ratio in CBO powder is approximately 0.54, while it is 0.46 and 0.67 in Cu-deficient and Bi-deficient CBOs, respectively. The cross-sectional FESEM images in Figure 7.1b and 7.1c verify that both CBOs have almost identical thicknesses, with Cu-deficient CBOs being 286 nm and Bi-deficient CBOs being 288 nm thick. A larger compositional divergence of Bi-deficient CBO results in a greater number of vacancy defects than in Cu-deficient CBO. This is further confirmed by DBS of positron annihilation, which is sensitive to the total number of defects and defect types in the photocathode[28], [73].

The crystal structure and phase purity of the tetragonal CBO (kusachiite – PDF 00-026-0502) films with varied compositions were confirmed by XRD analyses (Figure 7.2a). The main reflections from the (200), (211), (220), (002), (130), (112), (330), (132), (141), (420), (123), (332), (521), and (413) planes of CBO were observed at 20.99°, 28.13°, 29.81°, 30.83°, 33.42°, 34.37°, 45.30°, 46.21°, 46.85°, 47.91°, 53.15°, 55.89°, 60.84°, and 66.02°, respectively. Since CBO films are thin enough to allow TAS measurements in the transmission geometry, reflections attributed to FTO are also

observed. The peak at around 29.30° can be assigned to the (008) plane of Bi_2O_3 (PDF 03-065-3319), which is an expected minor side phase observed in both CBOs. Crystallite sizes and strain values were calculated from the analysis of the XRD data. The estimated values are tabulated in Table 7.2. Bi-deficient CBO has a crystallite size of 120.9 nm, while the Cu-deficient CBO has a larger crystallite size of 139.6 nm. Moreover, the estimated strain values support the pronounced defective nature of Bi-deficient CBO.

The observation of the four main A_{1g} features in the Raman spectra (Figure 7.2b) further confirms the crystal structure of tetragonal CBO for both photocathodes[23], [91]. It was also found that the Bi-deficient CBO has a slightly larger peak width and higher peak intensity than the Cu-deficient CBO, which is consistent with its more defective nature. The UV–vis spectra in Figure 7.2c demonstrate similar absorption characteristics for both CBOs in the UV–vis wavelength range, with the Cu-deficient CBO being more redshifted. Therefore, the Bi-deficient CBO is expected to be a slightly better absorber in the UV range. Still, the Cu-deficient CBO with a smaller band gap (Tauc analysis, inset of Figure 7.2c) could absorb a larger portion of the visible region[28]. Yet, the PEC performances depend on the charge-trapping nature of the states following the UV-vis absorption.

Although the conventional structural characterization results provide indirect information about the potential formation of vacancies in CBOs, a more direct assessment could be performed with the utilization of DBS. According to the DBS results in Figure 7.3a, the estimated S-parameter values (a measure of the low momentum valence electron contribution that is proportional to the number of vacancy defects) of the Bi-deficient CBO are much greater than that of Cu-deficient CBO, with some minor fluctuations throughout both films that give almost parallel linear fitting results. Different amounts and types of cation vacancies play a role in these differences in the S-parameters. Positrons are more likely to localize and annihilate with low-momentum electrons at trivalent $V_{Bi}^{'''}$ sites than at divalent $V_{Cu}^{''}$ sites. Therefore, Bi-deficient CBO corresponds to higher S-parameters and has a greater number of $V_{Bi}^{'''}$ vacancy defects, which is in good agreement with the EDX analysis results. In Figure 7.3b, the S-parameter values are drawn with respect to the W-parameter (a measure of the high momentum core electron contribution). The S–W linear fit lines essentially represent whether there are any

different types of defects in the system. Here, it can be clearly observed that both lines are well separated and almost parallel to each other. However, while all S-parameter values of the Bi-deficient CBO are much greater, the W-parameter average of the Cu-deficient CBO corresponds to a higher value than that of the Bi-deficient CBO. This is an expected outcome of the $V_{Bi}^{'''}$ in Bi-deficient CBO reducing the W-parameter since the Bi^{3+} cations are much bulkier than Cu^{2+}, and the removal of the Bi^{3+} cations from the CBO lattice decreases the W-parameter much more effectively. These findings further confirm the $V_{Cu}^{''}$- and $V_{Bi}^{'''}$-dominant nature of the Cu- and Bi-deficient CBOs.

The decrease in intensities of the Cu $2p_{3/2}$ and $2p_{1/2}$ XPS peaks at 953.4 eV and 933.7 eV, respectively, and their satellite peaks confirm the Cu-deficient nature of the Cu-deficient CBO surface (Figure 7.4a). Additionally, the surface Cu^{+}/Cu^{2+} ratio of the Bi-deficient CBO is estimated to be higher. This is an important finding due to the hole trapping capability of the Cu^{+} species. When the Cu LMM Auger spectra are compared in Figure 7.4b, a similar intensity relationship that justifies the near-surface compositional differences can be seen. The Bi 4f peak areas for both CBOs in Figure 7.4c are also consistent with the assumed compositional differences. For the Cu-deficient CBO, the Bi 4f binding energies are slightly greater due to the charge imbalance induced by the $V_{Cu}^{''}$ sites. The O 1 s spectra in Figure 7.4d do not indicate significant areal differences in terms of lattice O^{2-}. However, the extensively defective nature of the Bi-deficient CBO allows the adsorption of more OH^{-} species on the surface, and therefore, a larger amount of adsorbed hydroxide (OH_{ad}) was observed in Bi-deficient CBO. Overall, the compositional differences show that CBOs differ from each other to a much greater extent in terms of the amount of Bi. Therefore, the surface and bulk of the Bi-deficient CBO are presumed to be dominated by $V_{Bi}^{'''}$ sites, while the Cu-deficient CBO contains primarily $V_{Cu}^{''}$ sites.

Prior to the ultrafast investigations, the influence of cation vacancies on the photocurrent generation mechanism in CBO photocathodes was examined via various PEC experiments. Figure 3.1a shows the linear sweep voltammetry (LSV) curves obtained for both CBOs under O_2 purging conditions. The Cu-deficient CBO shows a better photocurrent density at all potentials beyond the onset. Additionally, the dark current behavior is slightly lower below 0.6 V. In Figure 3.1b, the charge trapping range

is determined from the intensity of the observed cathodic and anodic spikes that occur when the light is turned on and off during the chopped light experiment under N_2 purging conditions. While the cathodic spikes originate from excess electron accumulation on the surface of CBO, the anodic spikes are the result of a hole accumulation process. Both cathodic and anodic spikes are observed at higher intensities for the Bi-deficient CBO due to more dominant charge accumulation behavior below 1.05 V.

The LSV findings are supported by incident photon-to-current conversion efficiency (IPCE) measurements conducted at 0.9, 0.7, and 0.4 V. An efficiency jump between 0.9 and 0.7 V is expected. In contrast, a smaller increase in the IPCE was obtained at 0.4 V for the Bi-deficient CBO, as shown in Figure 3.1c. It is essential to emphasize 0.8 V as the possible onset potential for hole extraction from the trap states. Beyond this energy barrier, free carriers can be transferred more freely in the lattice, resulting in a higher photocurrent performance. Accordingly, the main reason behind these performance differences between the Cu-deficient and Bi-deficient CBOs is the different trapping tendencies following UV excitation, as further investigated with TAS.

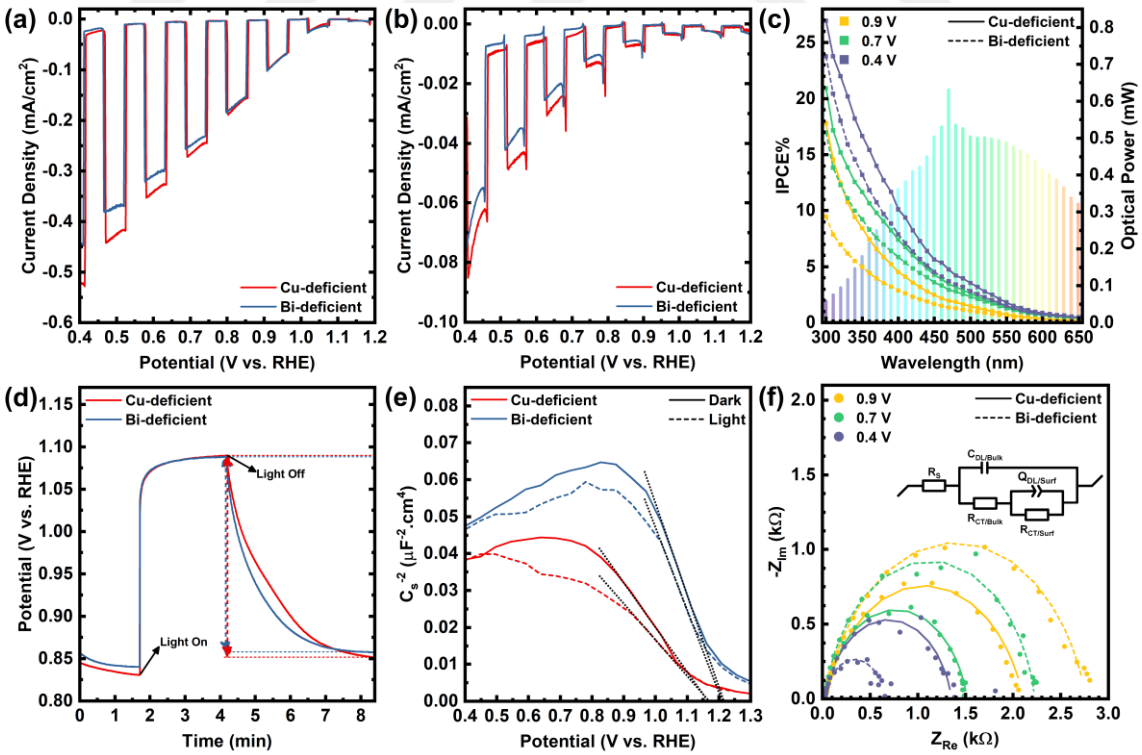

Figure 3.1: (a) Front-illuminated chopped LSV scans while (a) O_2 purging and (b) N_2 purging. (c) Potential-dependent IPCE. (d) OCP (ΔOCP = 0.239 V for Cu-deficient CBO and ΔOCP = 0.230 V for Bi-deficient CBO), (e) Mott–Schottky plots obtained in

the dark (φ_{fb} = 1.14 V, N_A = 96.36 × 10^{18} cm^{-3} for Cu-deficient CBO and φ_{fb} = 1.19 V, N_A = 61.92 × 10^{18} cm^{-3} for Bi-deficient CBO) and under light (φ_{fb} = 1.15 V, N_A = 121.7 × 10^{18} cm^{-3} for Cu-deficient CBO and φ_{fb} = 1.18 V, N_A = 66.28 × 10^{18} cm^{-3} for Bi-deficient CBO) conditions. (f) Nyquist plots of potential-dependent PEIS measurements.

The open circuit potential (OCP) measurements in Figure 3.1d reveal that the two CBOs have almost identical ΔOCP values that differ by 9 mV from each other. Both CBOs have similar OCPs under illumination. In the dark, the values for Cu- and Bi-deficient CBOs are 0.851 and 0.858 V, respectively. Additionally, discharging after switching off the light occurs at different rates for the two CBOs. The Bi-deficient CBO discharges its light-induced built-in potential faster due to a higher rate of hole trapping-related recombination at V_{Bi}''' defects, while the better-performing Cu-deficient CBO discharges slower and tends to sustain the built-in potential slightly longer.

In Figure 3.1e, the analysis of Mott–Schottky (MS) measurements performed under dark and illuminated conditions is presented. In the dark, the flat band potential (φ_{fb}) and acceptor density (N_A) of the Bi-deficient CBO were estimated to be 1.19 V and 61.92 × 10^{18} cm^{-3}, respectively. Compared to the Cu-deficient CBO (φ_{fb} = 1.14 V and N_A = 96.36 × 10^{18} cm^{-3}), the Bi-deficient CBO with more positive φ_{fb} and a smaller N_A experiences a larger band bending and Fermi level shift toward the VB edge[28]. Under illumination, φ_{fb} of Bi-deficient CBO decreases to 1.18 V, and its N_A increases to 66.28 × 10^{18} cm^{-3}. However, the effect of illumination is greater for the Cu-deficient CBO, especially in terms of the N_A. When the φ_{fb} of Cu-deficient CBO increases to 1.15 V, its N_A increases to 121.7 × 10^{18} cm^{-3}. Hence, the Bi-deficient CBO shows greater band bending and a lower Fermi level, which is an indication of trapped holes in V_{Bi}''' defects. The MS analysis results also reveal the difference between the two CBOs in terms of capacitance under dark and illuminated conditions. The difference between the MS curves of both samples represents the magnitude of the light response in terms of capacitance. Throughout the potential range of 1.05 to 0.45 V, the increase in the light-dependent capacitance could be attributed to the photoinitiated trapping of holes in the CBOs. Since the Bi-deficient CBO is expected to trap a greater number of holes, its light response in terms of capacitance is lessened.

In Figure 3.1f, the PEC potentiostatic electrochemical impedance spectroscopy (PEIS) results are represented as Nyquist plots obtained under illumination. The

corresponding charge transfer resistance ($R_{CT/Surf}$) values for the Cu-deficient CBO are smaller at 0.9 and 0.7 V (see also Table 7.3). In this potential region, the kinetics are limited by the charge transfer, and the traps mediate the activities of the CBOs. Consequently, the Cu-deficient CBO seems to perform better due to less hole trapping. Nevertheless, this behavior was only different at 0.4 V, with the Bi-deficient CBO corresponding to a smaller $R_{CT/Surf}$ value. However, in this cathodic potential range, multiple de-trapping and charge transfer channels could be accessible for the photoexcited holes.

The electron-trapping process occurring at various atomic sites within the bulk CBO lattice has been discussed in recent years. As an electron-trapping mechanism, $Cu^{2+} + e^- \rightarrow Cu^+$ reduction is proposed to occur at the surface of CBOs[19]. Interestingly, electron-trapping processes have been emphasized, although the holes make up the majority of the carriers in p-type CBOs. Herein, the $V''_{Cu} + h^+ \rightarrow V'_{Cu}$ and $V'''_{Bi} + h^+ \rightarrow V''_{Bi}$ (HPF_1 and HPF_2 in Figure 3.2a) mechanisms are considered prominent paths for the localization of holes in the Bi-deficient and Cu-deficient bulk CBO lattices. While the polaronic trapping of electrons occurs energetically near the CB edge, the holes become polaronically trapped close to the VB edge. Therefore, the photogenerated holes are expected to populate the mid-gap V'''_{Bi} and V''_{Cu} states that lie close to the VB hybrid orbitals of Cu 3d/Bi 6sp/O 2p and Cu 3d/O 2p, respectively[19]. The mechanistic pathways of the hole polaron formation processes are investigated via *ex situ* and *in situ* ultrafast TAS studies on Cu- and Bi-deficient CBOs.

The photoexcitation and decay events that are observed during the *ex situ* TAS experiments are shown in Figure 3.2a. Photoexcitation (P in Figure 3.2a) at 320 nm primarily involves the excitation of electrons from VB states with Cu 3d/Bi 6sp/O 2p and Cu 3d/O 2p character to the Bi 6p/O 2p CB states, resulting in the formation of photogenerated holes in the VB. The photoexcitation event is followed by the fast non-radiative relaxation of hot electrons and holes to reach a thermal equilibrium with the CBO lattice in the sub-ps time scales, also called hot electron and hot hole cooling (HEC and HHC in Figure 3.2a)[50]. Below the Fermi level, visible probe photons are subsequently absorbed by photogenerated holes at the VB edge (HA in Figure 3.2a). The HA event, populating deep VB orbitals of mixed Cu 3d/Bi 6sp/O 2p character, occurs in

exchange with the intra-valence band absorption (IVBA) of the deep VB electrons, as is commonly discussed in other p-type semiconductor systems[92]. Due to the p-type character of CBO, all positive transient absorption (TA) signals within the visible range are attributed to the absorption of photogenerated holes[90]. The features observed in the *ex situ* 3D TA surfaces in Figure 3.2b are correlated with this phenomenon.

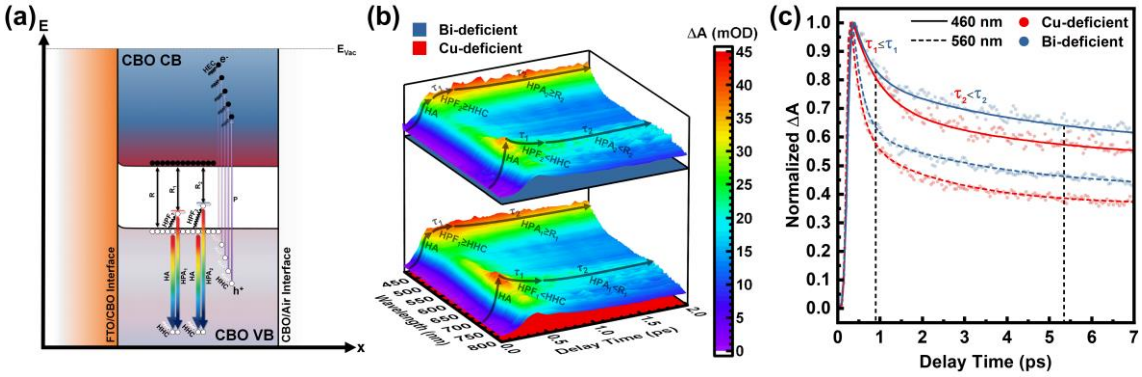

Figure 3.2: (a) Interfacial band diagram of CBO (*ex situ*). P is pump absorption at 320 nm. The kinetic processes considered are HEC: hot electron cooling, HHC: hot hole cooling, HA: hole absorption, HPF_1: $V_{Cu}^{'}$ hole polaron formation, HPF_2: $V_{Bi}^{''}$ hole polaron formation, HPA_1: $V_{Cu}^{'}$ hole polaron absorption, HPA_2: $V_{Bi}^{''}$ hole polaron absorption, R: recombination of VB holes with CB electrons, R_1: recombination of $V_{Cu}^{'}$ hole polarons with CB electrons, R_2: recombination of $V_{Bi}^{''}$ hole polarons with CB electrons. VB mid-gap states of $V_{Cu}^{''}$ and $V_{Bi}^{'''}$ character are shown in red and blue colors. (b) 3D TA surfaces and (c) TA decay kinetics of Cu-deficient and Bi-deficient CBOs compared at 460 nm and 560 nm ($\tau_1 = 587.8 \pm 240$ fs, $\tau_2 = 3.950 \pm 4.0$ ps at 460 nm and $\tau_1 = 242.5 \pm 34$ fs, $\tau_2 = 2.204 \pm 0.400$ ps at 560 nm for Cu-deficient CBO and $\tau_1 = 400.1 \pm 160$ fs, $\tau_2 = 4.494 \pm 2.7$ ps at 460 nm and $\tau_1 = 243.0 \pm 32$ fs, $\tau_2 = 3.387 \pm 0.830$ ps at 560 nm for Bi-deficient CBO).

Along with the HA event, photogenerated holes at the VB edge also start to localize in the sub-ps time range by short-range non-radiative relaxation (HPF_1 and HPF_2 in Figure 3.2a) to the near VB mid-gap states of $V_{Cu}^{''}$ and $V_{Bi}^{'''}$ character, respectively. In this case, $V_{Bi}^{''}$ polarons are expected to lie deeper within the band gap due to the trivalent nature of the $V_{Bi}^{'''}$ tightly binding the localized hole compared to the $V_{Cu}^{'}$ polarons that originate from divalent $V_{Cu}^{''}$ sites. The localized holes are then excited by the visible probe photons to the deep VB (HPA_1 and HPA_2 in Figure 3.2a) as an additional HA signal to the absorption of the holes located at the VB edge. Holes at the VB edge and localized holes at the $V_{Cu}^{''}$ and $V_{Bi}^{'''}$ sites later recombine with CB electrons through VB hole-CB electron

and V'_{Cu}-CB electron or V''_{Bi}-CB electron recombination channels (R, R_1, and R_2 in Figure 3.2a, respectively) within the ps-ns time range.

Predominantly, the HA character throughout the TA spectral range is considered to originate either from the excitation of the VB holes or the holes localized at the mid-gap states. The HPA character is observed more dominantly at shorter wavelengths, as depicted in Figure 2b, for both Cu- and Bi-deficient CBOs. It is important to note that the plateau behavior observed at shorter wavelengths is another indication of the polaronic processes (HPF and HPA) being more dominant than the HHC and recombination (R_1 and R_2) processes, while it is vice versa at longer wavelengths.

Analysis of the *ex situ* decay kinetics at 460 and 560 nm demonstrated in Figure 3.2c reveals a significant difference in the time evolution of the HPF and HHC processes (τ_1), which lasts less than a ps[90]. This difference is attributed to the higher number of holes localized at the V'''_{Bi} mid-gap states of the Bi-deficient CBO compared to the Cu-deficient CBO. Consequently, it is observed that the Cu-deficient CBO has shorter hole lifetimes within the HPA_1 time range (τ_2), which lasts a few ps[48]. These *ex situ* findings are correlated with the prolonged hole lifetimes in Bi-deficient CBO. Therefore, it can be presumed that the stronger HPA_2 character in the Bi-deficient photocathode has a direct negative influence on the PEC activity. Hence, applied potential-dependent *in situ* TAS investigations provide a deeper understanding of the ultrafast charge carrier dynamics of photogenerated holes and electrons[47], [51], [57], [93], [94].

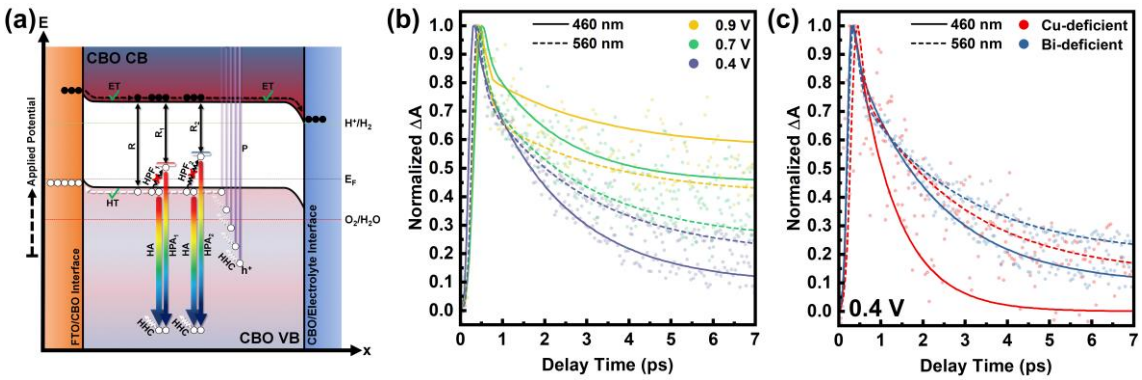

Figure 3.3: (a) Interfacial band diagram of CBO (*in situ*). The straight-line arrows indicate the photoexcitation and decay processes that occur during all TAS experiments, while the dotted-line arrows show the processes that occur only under in situ conditions. HT: hole transfer to the FTO/CBO interface, ET: electron transfer to the CBO/electrolyte

interface. (b) Potential-dependent TA decay kinetics of Bi-deficient CBOs at 460 nm and 560 nm at 0.9 V, 0.7 V, and 0.4 V. (c) TA decay kinetics of Cu-deficient and Bi-deficient CBOs at 460 nm and 560 nm at 0.4 V.

Applied potential gives rise to changes in charge carrier dynamics depicted in Figure 3.3a. The *in situ* decay kinetics presented in Figure 3.3b reveal a decrease in hole polaron (HPA) lifetimes as the potential was applied in the cathodic direction first from 0.9 to 0.7 V and then to 0.4 V. Thus, the cathodic potential-induced current density enhancement in the CBO leads to enhanced trap-assisted electron-hole recombination (R_1 and R_2) processes, resulting in shorter hole polaron lifetime. However, the influence of the application of a cathodic potential appears to be different for the decay kinetics at 460 and 560 nm. The 460 nm region is more susceptible to the application of a cathodic potential, while the kinetics at 560 nm show a lesser decrease in lifetime. The polaron (HPA_2) lifetime of the Bi-deficient CBO at 560 nm decreases by 12% (from 2.81 to 2.47 ps) when the applied potential changes from 0.9 to 0.4 V. Meanwhile, at 460 nm, the lifetime decreases by 26%. This confirms the susceptibility of hole polaron populations above the VB edge to the applied potential, revealing the enhanced recombination mechanisms of holes localized at $V_{Cu}^{''}$ and $V_{Bi}^{'''}$ sites (suppression of HPF_1 and HPF_2 through the enhancement of HT). Thus, the kinetics of both decay channels at 560 nm is less susceptible to the applied potential due to the less HPA character observed at longer wavelengths.

A comparison of the decay kinetics of both Cu- and Bi-deficient CBOs at 0.4 V (Figure 3.3c) highlights the enhanced recombination tendency of the holes localized at the $V_{Bi}^{'''}$ and $V_{Cu}^{''}$ sites. The influence of the applied potential in preventing the localization of holes and enhancing the hole transfer process in Bi-deficient CBO is minor. The results in Figure 3.3c support our hypothesis on the dominant recombination mechanism of hole localization at trivalent $V_{Bi}^{'''}$ sites (HPF_2) rather than at $V_{Cu}^{''}$ sites (HPF_1).

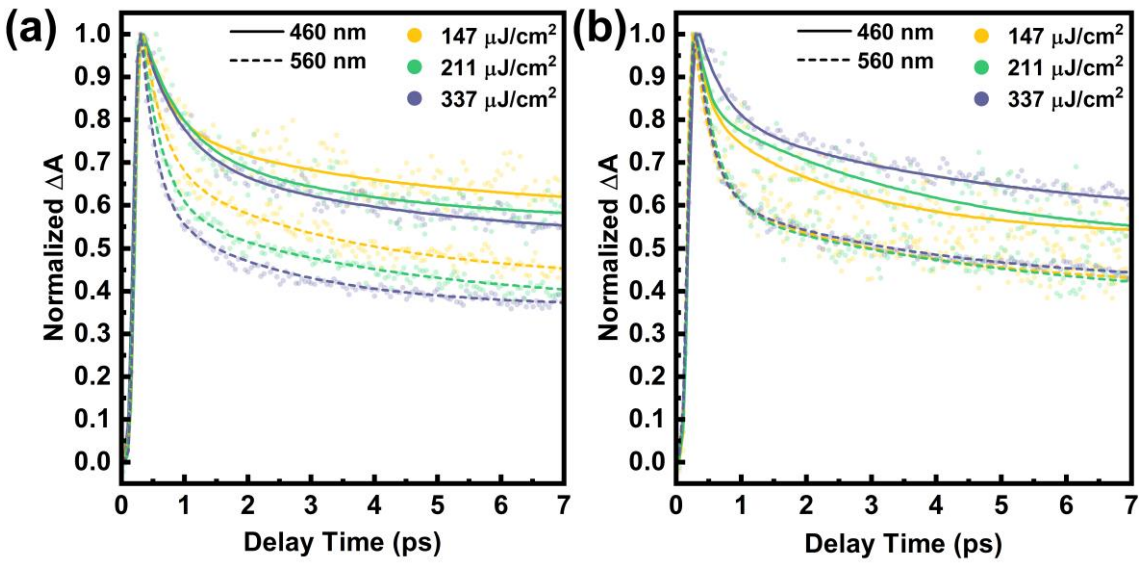

Figure 3.4: Pump fluence-dependent temporal TA kinetics for (a) Cu-deficient and (b) Bi-deficient CBOs.

Polaron formation tendencies of the hole populations in the presence of $V_{Bi}^{'''}$ and $V_{Cu}^{''}$ sites are further investigated via pump fluence-dependent TAS measurements. The results in Figure 3.4a and 4b can be explained based on the difference in the HA and HPA saturation behavior of the 460 and 560 nm kinetics for both $V_{Bi}^{'''}$ and $V_{Cu}^{''}$ sites. In particular, data suggest that the HA saturation of the Cu-deficient CBO is stronger, leading to a decrease in the overall absorption with increasing pump fluence. As a result, the hole population at the $V_{Cu}^{''}$ sites is reduced, leading to faster recombination and shorter τ_2 lifetimes at both wavelengths. In contrast, for the Bi-deficient CBO, kinetics at 460 and 560 nm are subject to different levels of saturation. As such, at 460 nm, HA saturation is weak. Therefore hole population in the $V_{Bi}^{'''}$ states increases with increasing pump fluence, giving a retarded recombination rate and prolonged lifetime. However, at 560 nm, the hole population remains nearly the same with increasing pump fluence, hinting at a saturation equilibrium that requires further investigation.

Overall, the pump fluence-dependent TAS results are also consistent with the less and more vacancy-bearing natures of the Cu- and Bi-deficient CBOs. While the *in situ* potential-dependent TAS results reveal the dominant HPA character present at the shorter wavelengths of the visible TA spectra, polaron lifetime and saturation dependence of the VB holes in the presence of $V_{Cu}^{''}$ and $V_{Bi}^{'''}$ sites is also confirmed through *ex situ* and *in situ* TAS experiments on compositionally manipulated Cu- and Bi-deficient CBOs. The

results contribute to the understanding of the relationship between the VB holes and mid-gap hole polaron states at ultrafast timescales.

3.4 Conclusion

In conclusion, the effects of polaronic hole trapping on the PEC HER performance are investigated through the compositional manipulation of CBOs in which cation vacancies act as hole localization sites. The hole polaron formation at $V_{Bi}^{'''}$ sites plays a more significant role in limiting the charge utilization and, therefore, hinders the photocurrent generation in CBOs to a greater extent compared to $V_{Cu}^{''}$ sites. The localized holes later recombine with CB electrons and cause a decrease in the free-carrier populations that are crucial for driving the PEC HER. Still, the probable existence of a hole polaron state lying close to the VB edge needs further investigation with VB-sensitive methods and element-specific domains. Direct observation of the phonon-assisted ultrafast localization of a hole state in a p-type photocathode material remains a difficult but intriguing experimental challenge. Such findings pave the way for a comprehensive understanding of the photocurrent generation mechanism in photocathodes and, therefore, can lead to the development of more efficient systems with shorter polaron lifetimes and better charge transfer capabilities to achieve higher PEC activities.

Chapter 4:
INTERFACIAL CHARGE TRANSFER DYNAMICS OF Cu_2O PHOTOCATHODES

4.1 Introduction

The application of heterojunction systems to solve performance and stability issues of photoelectrodes has been a widespread approach[95]. As a band gap engineering method, heterojunctions make use of band edge alignment to allow the charge transfer to occur at faster rates in photoelectrodes[96]. Therefore, understanding the charge carrier dynamics of such photoelectrode systems is an essential aspect of heterojunction research[97]. The processes that involve the photogenerated charge carriers in heterojunctions span from a few fs to a s[98]. However, due to the formation of multiple interfaces between the layers of the heterojunction photoelectrodes as well as the electrolyte, charge carrier dynamics at the photoelectrode/electrolyte interface play the most crucial role in determining the PEC limitations of photoelectrodes within the time range of μs to s[99]. In this time regime, the photogenerated charge carriers can accumulate at interfaces, recombine with other trapped carriers, take part in side reactions that cause photocorrosion, go through de-trapping, and dissipate with the remaining carriers[100]. There are several time- and frequency-resolved methods that are used to track these charge carrier-related events, such as TPC and IMPS[60], [61].

In recent years, electron extraction and protection layers have been widely used to stabilize and increase the activity of the Cu_2O layer of Cu_2O-based photocathodes[101]. Several examples of such solutions include n-TiO_2, Al:ZnO (AZO), metal-organic framework (MOF), and carbon overlayers[102]. As a type-II heterojunction, FTO/Cu_2O/TiO_2 is an extensively studied system in OWS research[103]. Due to a suitable band alignment, the TiO_2 layer acts as an electron extraction layer, preventing the electron trapping-related self-reduction of the Cu_2O layer[104]. Additionally, the FTO/Cu_2O/TiO_2 may also work as a Z-scheme heterojunction and boost the interfacial electron-hole recombination to prevent excess electron accumulation at the Cu_2O surface[36]. Alongside these possibilities, a TiO_2 underlayer has never been explored as an electron extractor from the bulk of the Cu_2O with an FTO/TiO_2/Cu_2O hierarchy.

In this study, we utilize TPC to decipher the charge carrier dynamics of Cu_2O-based single and heterojunction photocathodes within the ms time resolution. Although the Cu_2O-based photocathodes have been studied quite extensively in recent years, the understanding behind their charge trapping behavior upon illumination remains relatively poor[105], [106]. Therefore, this chapter explores the FTO/TiO_2/Cu_2O hierarchy as a type-II heterojunction candidate and later provides a deeper comprehension of the charge trapping tendencies of both the FTO/Cu_2O and FTO/TiO_2/Cu_2O systems through a series of TPC experiments coupled with chopped LSV measurements and comprehensive structural characterization results. The study also discusses the connections between the structural properties of the Cu_2O layer and the electrodeposition times regarding the crystallinity, grain size, and amount of defects within the photocathode system.

4.2 Experimental Methods

Synthesis details of Cu_2O and TiO_2 layers have been described in sections 2.1.1 and 2.1.3. Structural characterization experiments carried out on Cu_2O photocathodes include FESEM, EDX, XPS, XRD, Raman, and UV-vis spectroscopy. The experimental details of structural characterization techniques used in this chapter are described in section 2.2. The PEC performance tests carried out on Cu_2O photocathodes consist of LSV. LSV experiments are defined under section 2.3.1 and 2.3.2. Time-resolved TPC investigations are described under section 2.4.2.

4.3 Results & Discussion

The Cu_2O photocathode layer is optimized through different electrodeposition durations. Varying grain sizes and film thicknesses dependent on the electrodepositon time were imaged via top-view FESEM and cross-sectional FESEM imaging, shown in Figure 4.1 and Figure 4.2. The top-view FESEM images explain the color change observed at different deposition times. The color of the Cu_2O shifts toward red due to the larger grain formation compared to the yellow and orange colors observed at 15 and 30 min depositions (Figure 4.1a and Figure 4.1b).

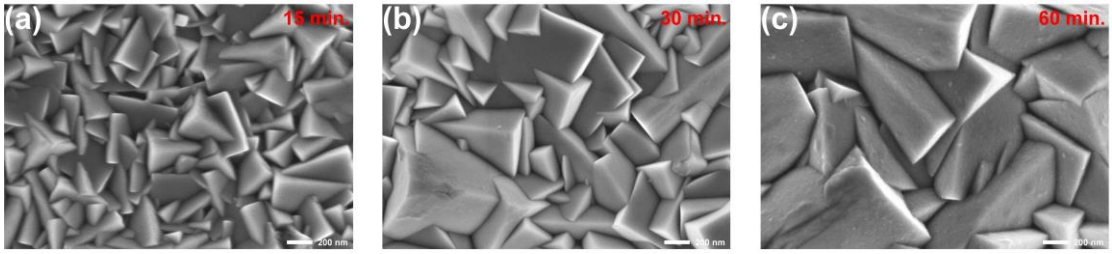

Figure 4.1: Top-view FESEM images of Cu_2O photocathodes with varying electrodeposition times: (a) 15 min, (b) 30 min, and (c) 60 min.

Additionally, the film thicknesses also increase with the deposition time, as shown in Figure 4.2. In Figure 4.2a, the film thickness is estimated as 586 nm for the 15 min deposited Cu_2O thin film. As the deposition time doubles, the estimated film thickness becomes 1225 nm for the 30 min deposited photocathode in Figure 4.2b. Lastly, at 60 min, the thickness reaches 2811 nm, as depicted in Figure 4.2c. Consequently, the grain sizes, grain boundaries, and film thicknesses are expected to influence the charge trapping properties of the Cu_2O photocathode layers which eventually determines their PEC activity and stability[107].

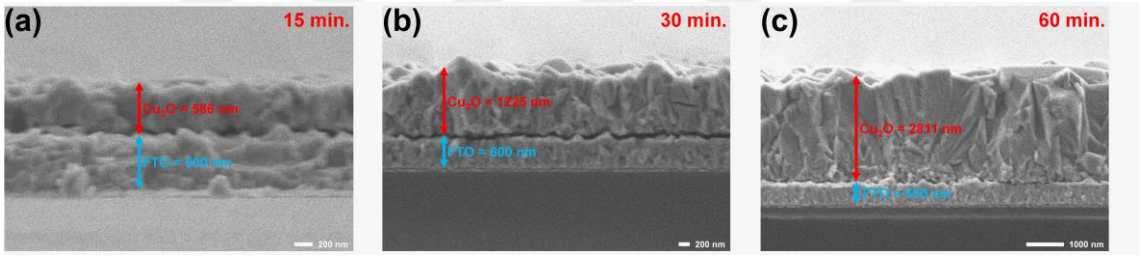

Figure 4.2: Cross-sectional FESEM images of Cu_2O photocathodes with varying electrodeposition times: (a) 15 min, (b) 30 min, and (c) 60 min.

The successful synthesis of bare FTO/Cu_2O and FTO/TiO_2 hierarchies was confirmed through cross-sectional EDX mapping, as depicted in Figure 4.3. In Figure 4.3a, the distribution of the Sn L-edge and Cu K-edge signals in EDX mapping images confirms the formation of a clear FTO/Cu_2O junction. On the other hand, in Figure 4.3b, a bare FTO/TiO_2 junction is successfully mapped with Sn L-edge and Ti K-edge signals. The image clearly shows the TiO_2 sitting on top of the FTO layer.

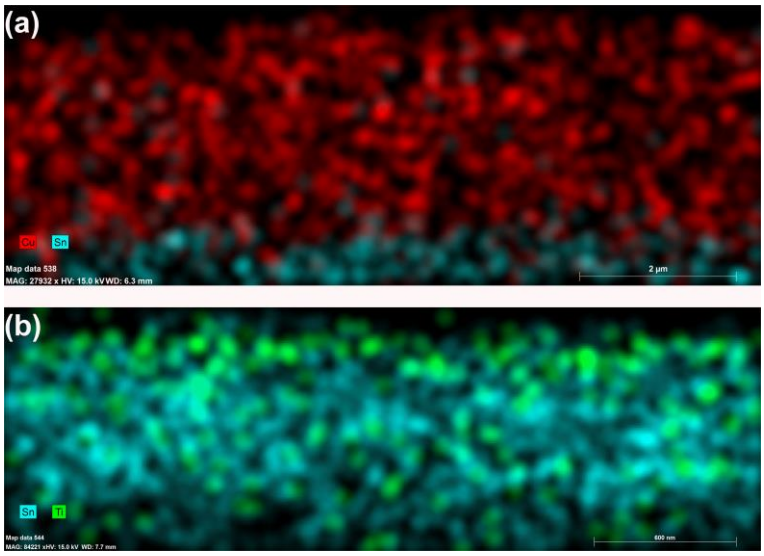

Figure 4.3: Cu K-edge, Sn L-edge, and Ti K-edge EDX mapping images of (a) FTO/Cu_2O and (b) FTO/TiO_2 junctions.

Cubic Cu_2O crystal phase formation (cuprite – ICDD PDF: 01-074-1230) was confirmed for all deposition times through XRD measurements. The XRD patterns shown in Figure 4.4a confirm a dominant growth of Cu_2O along the (111) plane direction with the increased deposition time. Also, in the inset of Figure 4.4a, a shift toward smaller 2θ values is observed with an increase in the deposition time. The angle of the (111) plane of 15 min deposited Cu_2O (36.58°) shifts to 36.56° for the 30 min deposited Cu_2O photocathode. At 60 min deposition, the angle yet again shifts down to 36.54°. Due to the inverse relationship between the 2θ angle and interplanar lattice spacing (d-spacing), such a shift toward smaller angles is interpreted as an increase in d-spacing and a decrease in compressive lattice strain[108]. Therefore, it can be concluded that longer deposition times result in less defective and highly crystalline cubic Cu_2O structure. Along with the dominant (111) plane, the existence of other facets of the cubic Cu_2O structure, such as (110) at 29.71°, (200) at 42.47°, (220) at 61.62°, (221) at 65.65°, and (311) at 73.69° are also confirmed for the 60 min photocathode.

The reflections that belong to the FTO (SnO_2, cassiterite – ICDD PDF: 01-070-4175) substrate are also observed at 2θ values of 26.59°, 33.80°, 37.83°, 51.61°, and 54.65° that are attributed to the (110), (101), (200), (211), (220), (310), and (301) planes respectively.

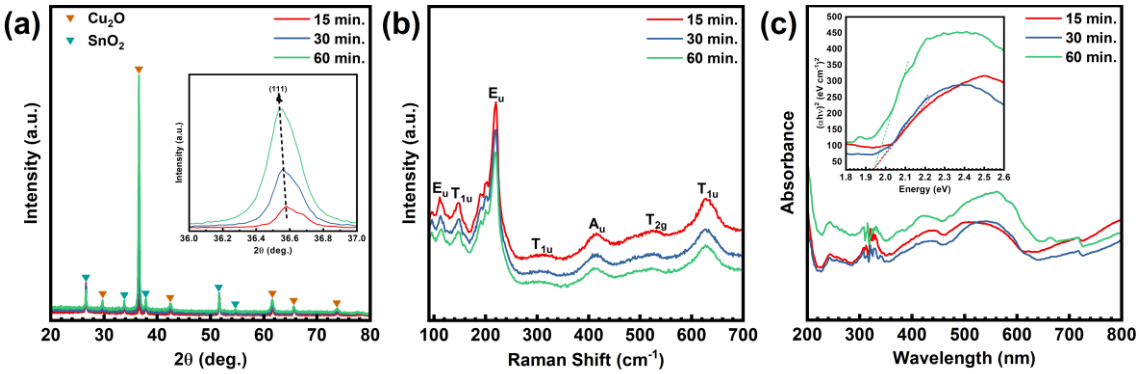

Figure 4.4: (a) XRD, (b) Raman spectra, and (c) UV–vis absorbance spectra of Cu_2O photocathodes with varying electrodeposition times. Inset of (c): Tauc analysis to determine the band gap values (E_g = 1.94 eV).

Raman spectra collected from the Cu_2O layers with varying electrodeposition times are also in parallel with the XRD results. In Figure 4.4b, the Raman peaks that stem from the stretching of the Cu–O bonds in the cubic Cu_2O lattice are observed at 110 cm^{-1}, 146 cm^{-1}, 220 cm^{-1}, 310 cm^{-1}, 412 cm^{-1}, 520 cm^{-1}, and 625 cm^{-1} with E_u, T_{1u}, E_u, T_{1u}, A_u, T_{2g}, and T_{1u} symmetries, respectively[109], [110]. Overall, an increase in the 220 cm^{-1} peak intensity was observed with the increased deposition time. On the other hand, the background intensity increase is attributed to the thinner films providing a stronger background signal from the FTO substrate.

The UV-vis spectra of the electrodeposited Cu_2O thin films in Figure 4.4c indicate that the deposition time does not affect the absorption characteristics of the photocathodes. Therefore, the Tauc analyses in the inset of Figure 4.4c yield almost identical band gap values for all Cu_2O photocathodes at 1.94 eV.

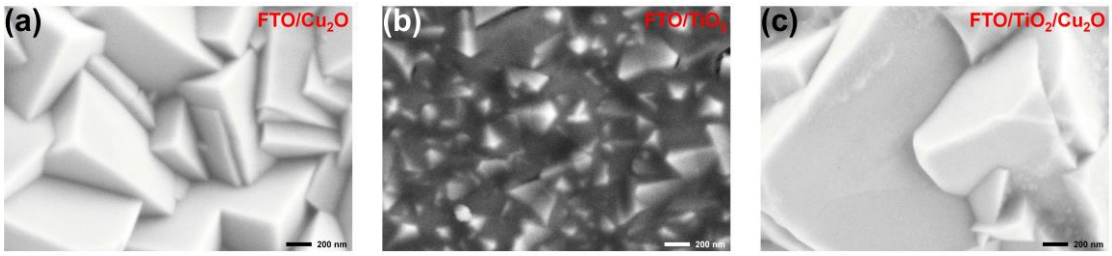

Figure 4.5: Top-view FESEM images of (a) FTO/Cu_2O, (b) FTO/TiO_2, and (c) FTO/TiO_2/Cu_2O hierarchies.

Top-view FESEM images given in Figure 4.5 show the morphological differences between the bare Cu_2O, bare TiO_2, and heterojunction hierarchies. In Figure 4.5a, a usual Cu_2O crystal phase growth is observed while the bare TiO_2 phase in Figure 4.5b has an

amorphous look due to the previously discussed synthesis technique. When the top-view of the heterojunction system in Figure 4.5c is compared to the bare Cu_2O layer in Figure 4.5a, a difference in the grain sizes is observed. While the bare Cu_2O layer has sharper edges, the heterojunction consists of grains that have more rounded edges. Therefore, the crystallinity of the FTO/Cu_2O hierarchy is observed as higher than the FTO/TiO_2/Cu_2O. This observation is considered to stem from the electrochemical growth of Cu_2O on amorphous TiO_2 resulting in a less crystalline phase due to a higher lattice mismatch than the growth on a highly crystalline FTO substrate.

The FTO/TiO_2/Cu_2O heterojunction photocathode is also mapped cross-sectionally with EDX. In Figure 4.6, the distribution of the Sn L-edge, Ti K-edge, and Cu K-edge signals again confirms the hierarchy. The intensification of the Ti K-edge signal within the FTO/Cu_2O interface clearly indicates the formation of a TiO_2 underlayer to form the FTO/TiO_2/Cu_2O order.

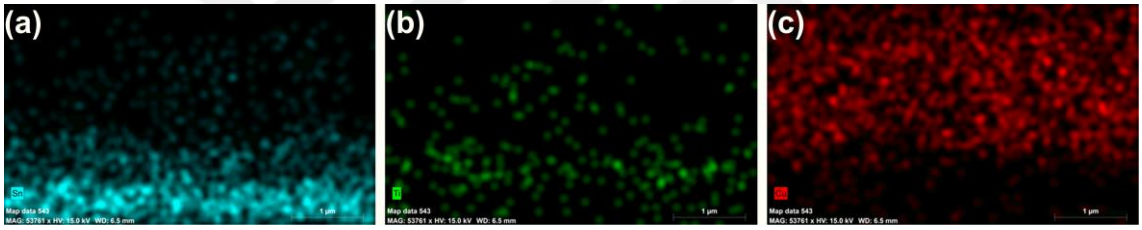

Figure 4.6: Sn L-edge, Ti K-edge, and Cu K-edge EDX mapping images of (a) FTO, (b) TiO_2, and (c) Cu_2O layers of an FTO/TiO_2/Cu_2O heterojunction.

XRD findings on the three different hierarchies are in line with the EDX mapping results. In Figure 4.7a, the cubic Cu_2O formation is again extensively observed along the (111) plane for both the FTO/Cu_2O and FTO/TiO_2/Cu_2O photocathodes. However, due to the compact-mesoporous morphology of the TiO_2 layer, no XRD peaks related to the TiO_2 phase were observed for both the FTO/TiO_2 and FTO/TiO_2/Cu_2O systems. Higher crystallinity was observed in terms of XRD peak intensities due to the shift of the (111) plane to lower 2θ degrees for the bare FTO/Cu_2O system compared to the FTO/TiO_2/Cu_2O heterojunction (Inset of Figure 4.7a). XRD peaks related to the FTO layer were observed for all three systems, as expected.

The Raman spectra of the bare FTO/Cu_2O and FTO/TiO_2/Cu_2O systems appear almost identical, as it is shown in Figure 4.7b. Yet, a Raman peak broadening is observed for the structurally sensitive T_{1u} peaks of the FTO/TiO_2/Cu_2O heterojunction system due

to the prolonged Raman lifetimes[109]. Additionally, Raman spectra in the inset of Figure 4.7b reveal that the compact-mesoporous TiO_2 layer consists of the anatase phase. The four main Raman peaks of the anatase phase (E_g, B_{1g}, A_{1g}, and E_g) are observed at 145 cm^{-1}, 400 cm^{-1}, 550 cm^{-1}, and 635 cm^{-1}[111].

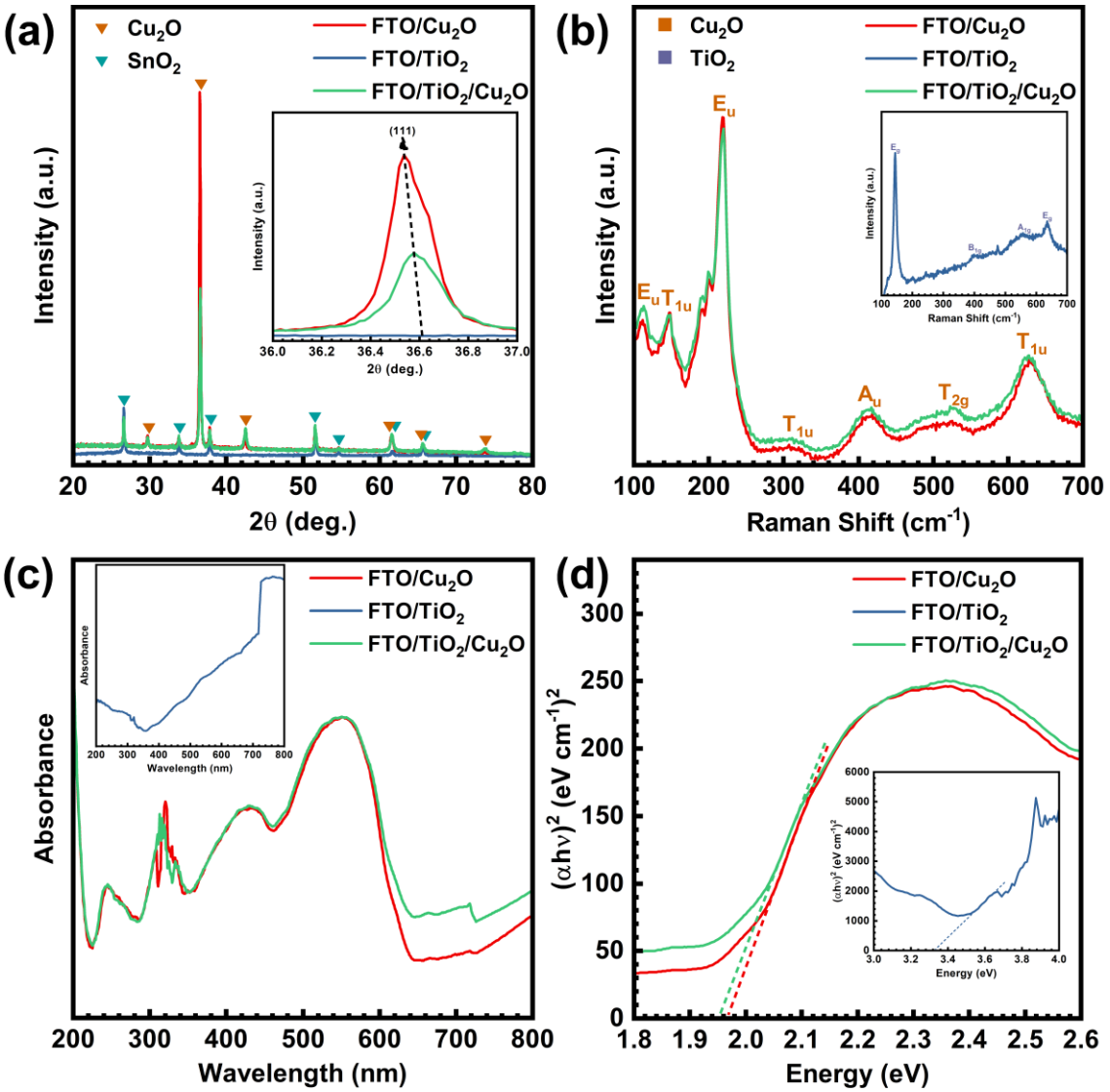

Figure 4.7: (a) XRD, (b) Raman spectra, (c) UV–vis absorbance spectra, and (d) direct band gap Tauc analyses of FTO/Cu_2O (E_g = 1.97 eV), FTO/TiO_2 (E_g = 3.32 eV), and FTO/TiO_2/Cu_2O (E_g = 1.95 eV) hierarchies. Inset of (c) and (d): UV–vis absorbance spectra and direct band gap Tauc analysis of FTO/TiO_2 junction, respectively.

The UV-vis spectra and direct band gap Tauc analyses given in Figure 4.7c and Figure 4.7d show that the FTO/Cu_2O and FTO/TiO_2/Cu_2O systems do not differ drastically in terms of absorption characteristics and band gap values. The direct band gap value of the bare FTO/Cu_2O system is estimated as 1.97 eV, while the

FTO/TiO_2/Cu_2O heterojunction has a direct band gap of 1.95 eV. This similarity is an expected outcome due to the thick layer of Cu_2O blocking the light absorption of the TiO_2 underlayer. Nevertheless, the absorption spectrum and band gap values of the bare FTO/TiO_2 system are given in the insets of Figure 4.7c and Figure 4.7d, respectively. Accordingly, the direct band gap of the FTO/TiO_2 is estimated as 3.32 eV.

The XPS results given in Figure 4.8a support the previously discussed structural characterization findings and confirm that the surfaces of both FTO/Cu_2O and FTO/TiO_2/Cu_2O systems are dominated by the Cu^+ species. Yet, a broadening is observed for both the Cu $2p_{1/2}$ (951.9 eV) and Cu $2p_{3/2}$ (932.0 eV) peaks of the heterojunction system. This finding supports the previous discussions about the lower crystallinity of the Cu_2O surface within the FTO/TiO_2/Cu_2O system with respect to the bare FTO/Cu_2O junction. Additionally, the broadening could be the indication of an oxygen-deficient structure due to a broader Cu oxidation state distribution resulting from the oxygen defects within the lattice. Similar inferences can also be made from the Cu LMM Auger spectra depicted in Figure 4.8b.

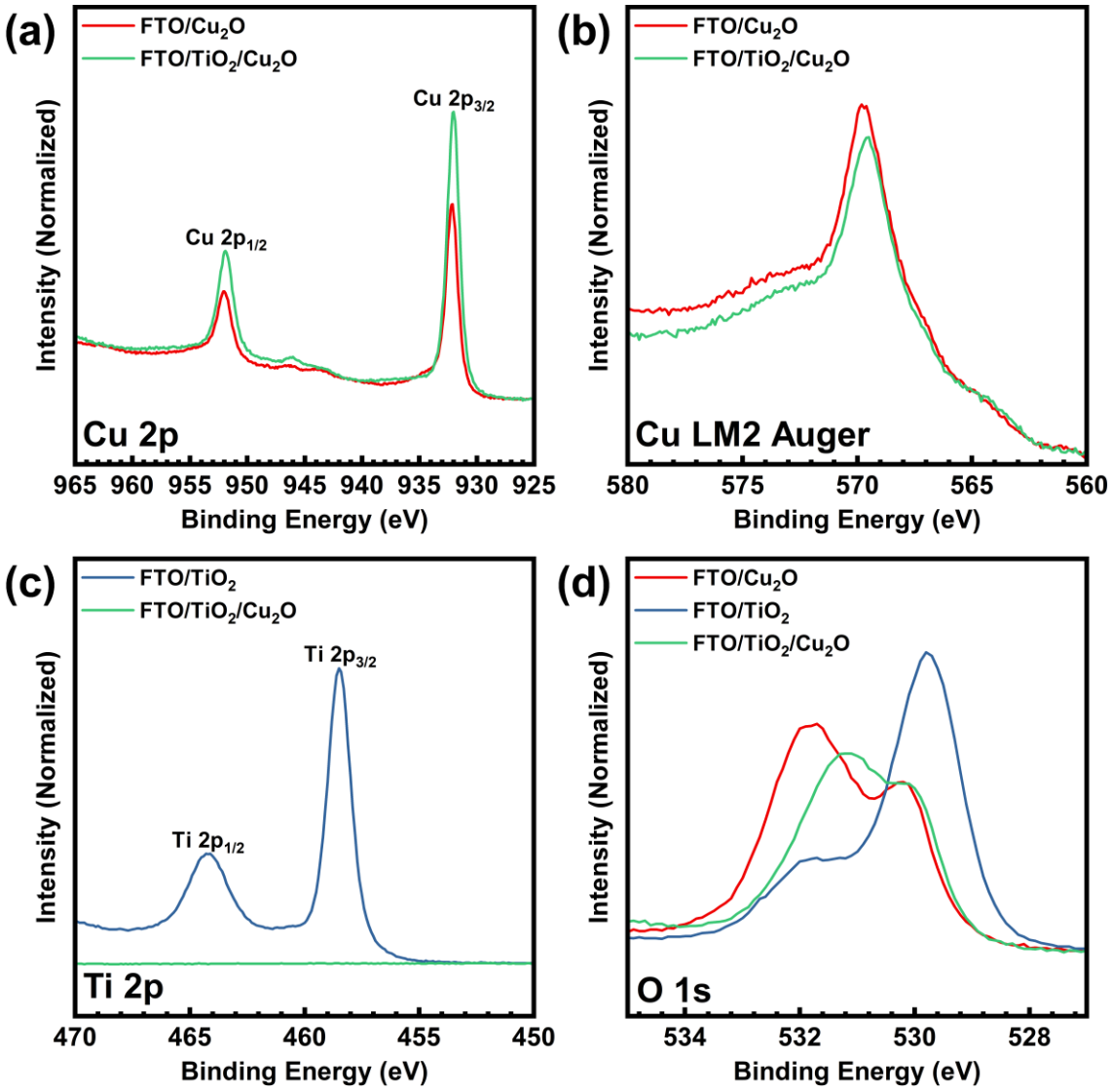

Figure 4.8: (a) Cu 2p, (b) Cu LM2 Auger, (c) Ti 2p, and (d) O 1 s XPS spectra of FTO/Cu_2O, FTO/TiO_2, and FTO/TiO_2/Cu_2O hierarchies.

On the other hand, the Ti 2p spectra given in Figure 4.8c confirm that the surface of the bare FTO/TiO_2 system consists of Ti^{4+} species. The Ti $2p_{1/2}$ and Ti $2p_{3/2}$ peaks at 464.3 eV and 458.5 eV correspond to a 4+ oxidation state for the Ti atoms on the surface. Such peaks are not observed for the FTO/TiO_2/Cu_2O system due to the thickness of the Cu_2O on the top, as expected.

Lastly, the O 1s spectra for all three systems in Figure 4.8d indicate the existence of lattice oxygen species (O^{2-}) for both the Cu_2O and TiO_2 layers at 530.2 eV and 529.8 eV, respectively. Furthermore, surface-adsorbed hydroxyl species of OH_{ad} give a shoulder at 531.7 eV and 531.2 eV for the FTO/Cu_2O and FTO/TiO_2/Cu_2O systems, respectively.

Meanwhile, the FTO/TiO_2 system also has its OH_{ad} peak at 531.7 eV. The 0.5 eV low binding energy shift of the OH_{ad} peak for the heterojunction system hints at a more negative average oxidation state for these oxygen species compared to the FTO/Cu_2O and FTO/TiO_2 systems. This finding is again in parallel with the discussions made previously on the less crystalline and oxygen-deficient nature of the FTO/TiO_2/Cu_2O system. Such a system would be expected to have a more positively charged surface due to the oxygen vacancies and, therefore, lower the OH_{ad} binding energies[112].

PEC activity and stability of Cu_2O layers with varying deposition times were scanned through five consecutive chopped LSV scans between 0.5 V and 0.0 V vs. RHE under front and back illumination conditions. In Figure 4.9a, the poor PEC stability of the 15 min electrodeposited photocathode can be observed right after the first front illuminated chopped LSV scan. The photocurrent density produced at 0.1 V drops by 66% during the second LSV measurement and keeps falling until the fifth scan. Following the front-illuminated measurements, the poor photocurrent response under back illumination is also depicted in the inset of Figure 4.9a.

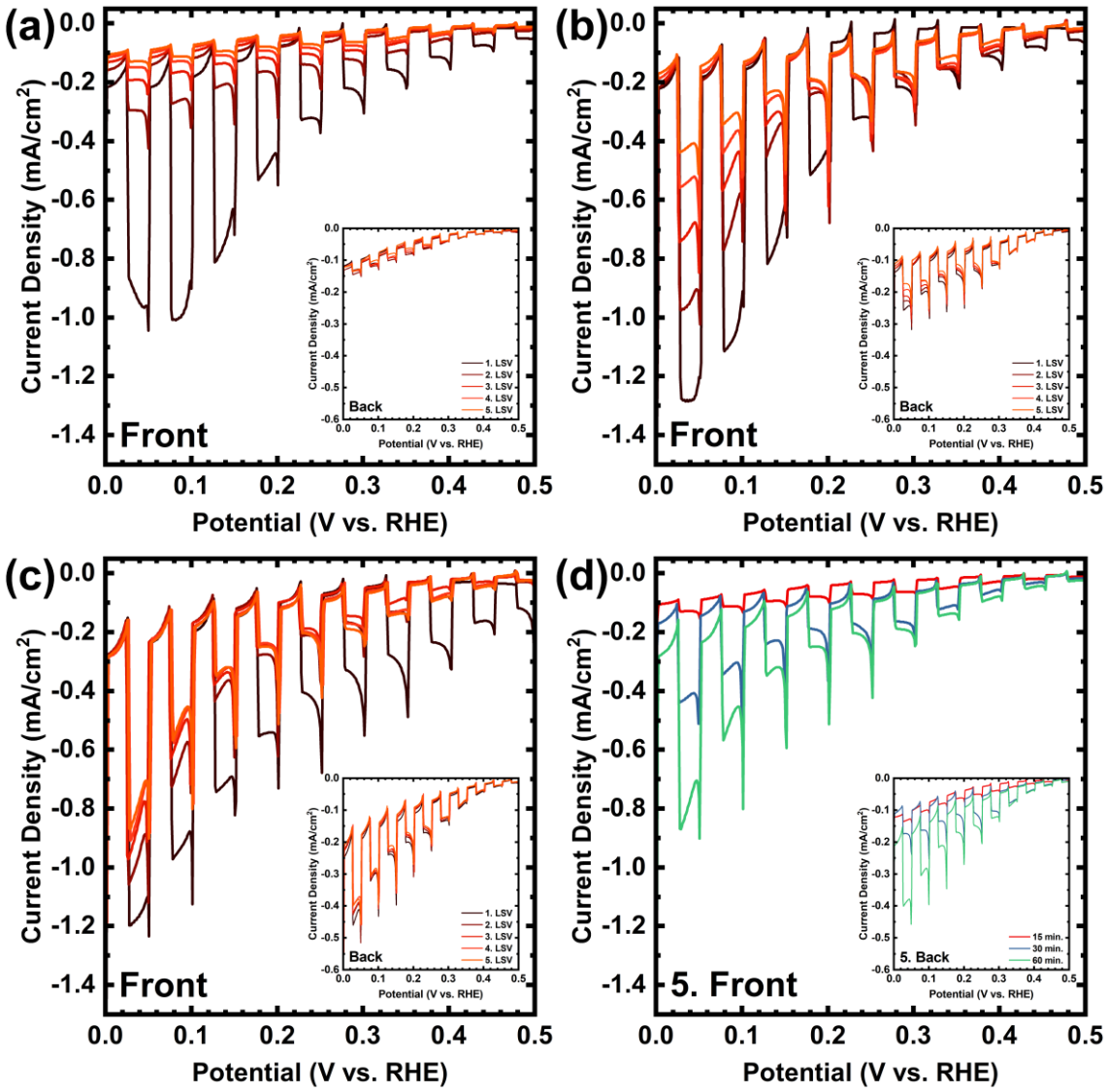

Figure 4.9: Five consecutive front-illuminated chopped LSV scans of (a) 15 min, (b) 30 min, and (c) 60 min electrodeposited Cu_2O photocathodes and (d) comparison of the fifth front-illuminated chopped LSV scans. Insets (a), (b), and (c) include five consecutive back-illuminated chopped LSV scans of photocathodes, and inset (d) consists of a comparison of the fifth back-illuminated chopped LSV scans.

The photocurrent performance and stability of the 30 min electrodeposited Cu_2O photocathode under front illumination in Figure 4.9b and under back illumination in the inset of Figure 4.9b is greater than the 15 min photocathode. Yet, the best PEC activity and stability under both front and back illumination is obtained with the 60 min electrodeposited Cu_2O photocathode, as can be seen in Figure 4.9c and its inset.

Finally, the comparison of the fifth front and back-illuminated LSV scans of each photocathode is given in Figure 4.9d and its inset. This comparison clearly shows that the

60 min electrodeposited Cu_2O photocathode has superior PEC activity and stability due to the previously discussed structural properties such as larger grain size, less defective, and highly crystalline cubic Cu_2O structure.

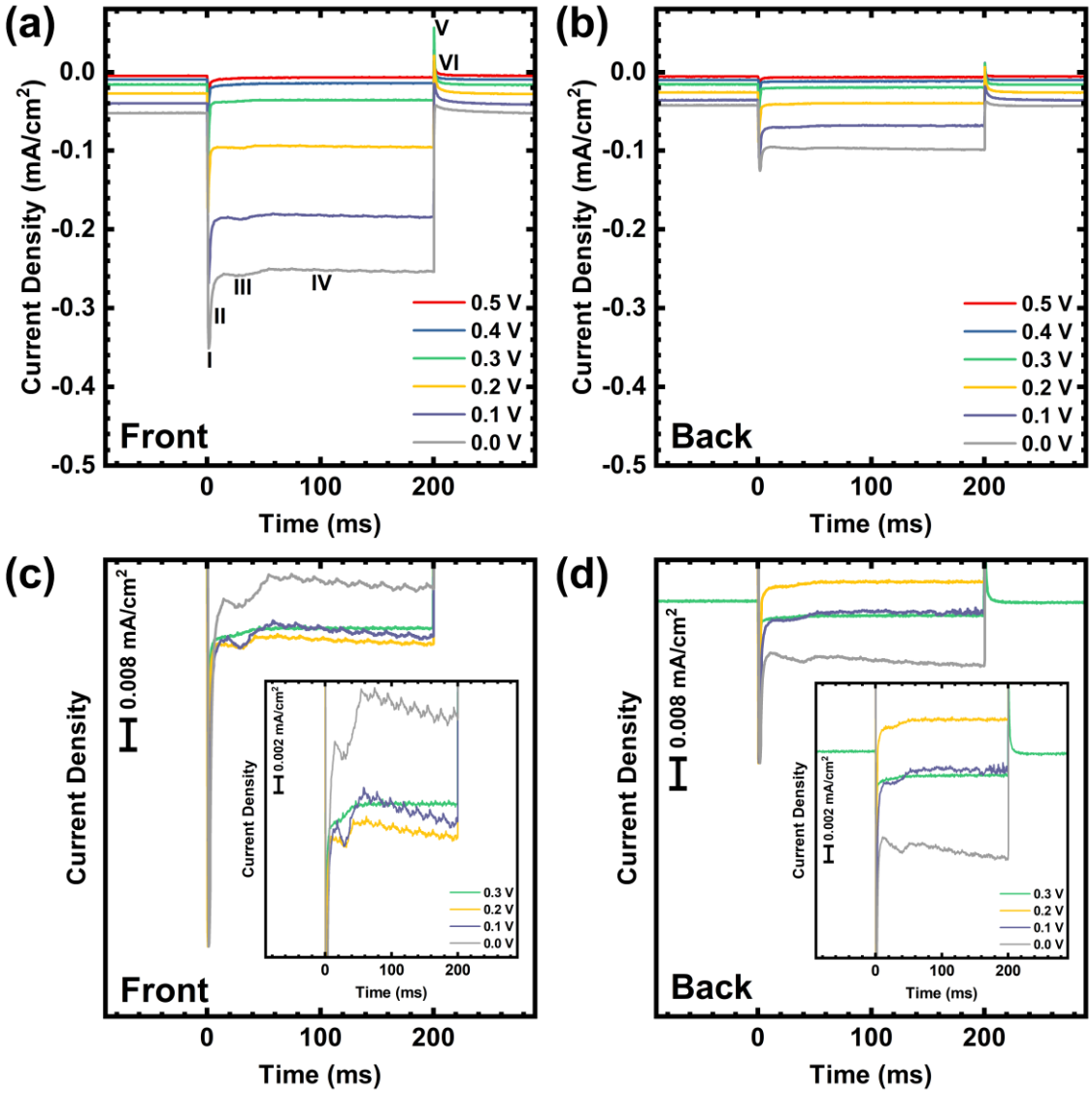

Figure 4.10: Potential-dependent TPC measurements taken from 60 min electrodeposited Cu_2O photocathode under (a) front and (b) back illumination conditions with their stacked representations for 0.3-0.0 V in (c) and (d), respectively. Roman numerals in (a) indicate the photoinitiated charge carrier processes. I: cathodic electron accumulation due to the photoexcitation with the LED pulse, II: recombination of the photogenerated electrons with the surface trapped holes, III: photoreduction of the photocathode surface, IV: periodic oscillation of the photocurrent response named as "wiggles", V: anodic hole accumulation due to the surface trapped holes exceeding the number of electrons following the end of the interaction with the LED pulse, VI: recombination of the trapped holes with the remaining electrons. Insets of (c) and (d) provide a close-up view of the wiggles.

Charge carrier-related events that occur at the photocathode interfaces within the ms timescale are investigated via potential-dependent TPC experiments. Accordingly, these charge carrier processes are shown in Figure 4.10a with Roman numerals. Although these processes are mutually observed under back illumination conditions in Figure 4.10b, the assignment of the charge carrier events is done with the front-illuminated results due to the achieved higher current resolution.

Following the interaction with an LED pulse, the first event that is observed is the cathodic electron accumulation spike, denoted as I in Figure 4.10a. This feature stems from the formation of photogenerated electrons at the Cu_2O surface. It dissipates fast due to the recombination of these electrons with the surface trapped holes at the Cu^+ or V''_{Cu} sites denoted as II.

$$Cu_2O + H_2O + 2e^- \leftrightarrow 2Cu + 2OH^- \text{ (+0.47 V vs. SHE)} \quad \text{(Eq. 4.1)}$$

$$2CuO + H_2O + 2e^- \leftrightarrow 2Cu_2O + 2OH^- \text{ (+0.60 V vs. SHE)} \quad \text{(Eq. 4.2)}$$

As the recombination of the excess carriers ends, remainder of the photoexcited electrons give rise to a photoreduction peak (denoted as III) below 0.3 V that occurs either from the reduction of Cu^+ to Cu^0 (Eq. 4.1) or Cu^{2+} to Cu^+ (Eq. 4.2). Regarding the reduction potentials of these processes, previously discussed XPS results, and the potential-dependent observations in Figure 4.10a, this photoreduction peak is assigned to the reduction of Cu^+ to Cu^0.

The photoreduction peak is followed by a rather strange but intriguing feature, which is the periodic oscillation of the photocurrent signal. This event is denoted as IV in Figure 4.10a and is called the wiggle behavior[56]. The periodic oscillations that are observed along the photocurrent baseline include continuously revolving anodic and cathodic events, as can be seen clearly in Figure 4.10c and its inset. However, the intensity of these wiggles falls almost under the noise limits under back illumination conditions (Figure 4.10d) due to the lower current resolution. Yet, the wiggles are not considered to result from the HER processes that occur at the photocathode/electrolyte interface but from the side processes that involve the consumption of photogenerated charge carriers. Still, the origin of these wiggles remains an interesting topic that requires further investigation.

As the interaction between the LED pulse and the photocathode system comes to an end, most of the photogenerated electrons at the surface quickly dissipate. This gives rise to an excess hole population that was previously occupying the surface trap sites of Cu^{+} or $V_{Cu}^{''}$ origin. Due to this excess hole population at the surface, an anodic response is observed, denoted as V. Following the positive charge build-up at the photocathode surface due to hole trapping, these trapped holes recombine with the remaining minority electrons until the system reaches a steady state (denoted as VI).

When these six processes are considered in relation to each other, it is observed that there is a direct correlation between the intensity of I and III. Therefore, it can be claimed that the amount of electron accumulation at the photocathode surface intensifies the photoreduction peak. Additionally, the intensity of the wiggles in IV was also observed to increase with the intensity of I, therefore indicating the accumulated charge carrier-related origin of such wiggles. Lastly, the intensity of V is observed as inversely proportional to the intensities of I, III, and IV. This is clearly due to the smaller number of holes sitting at the trap sites of Cu^{+} or $V_{Cu}^{''}$ origin at lower potentials. All six events are, therefore, associated with the intensity of the applied potential and induction of higher photocurrent.

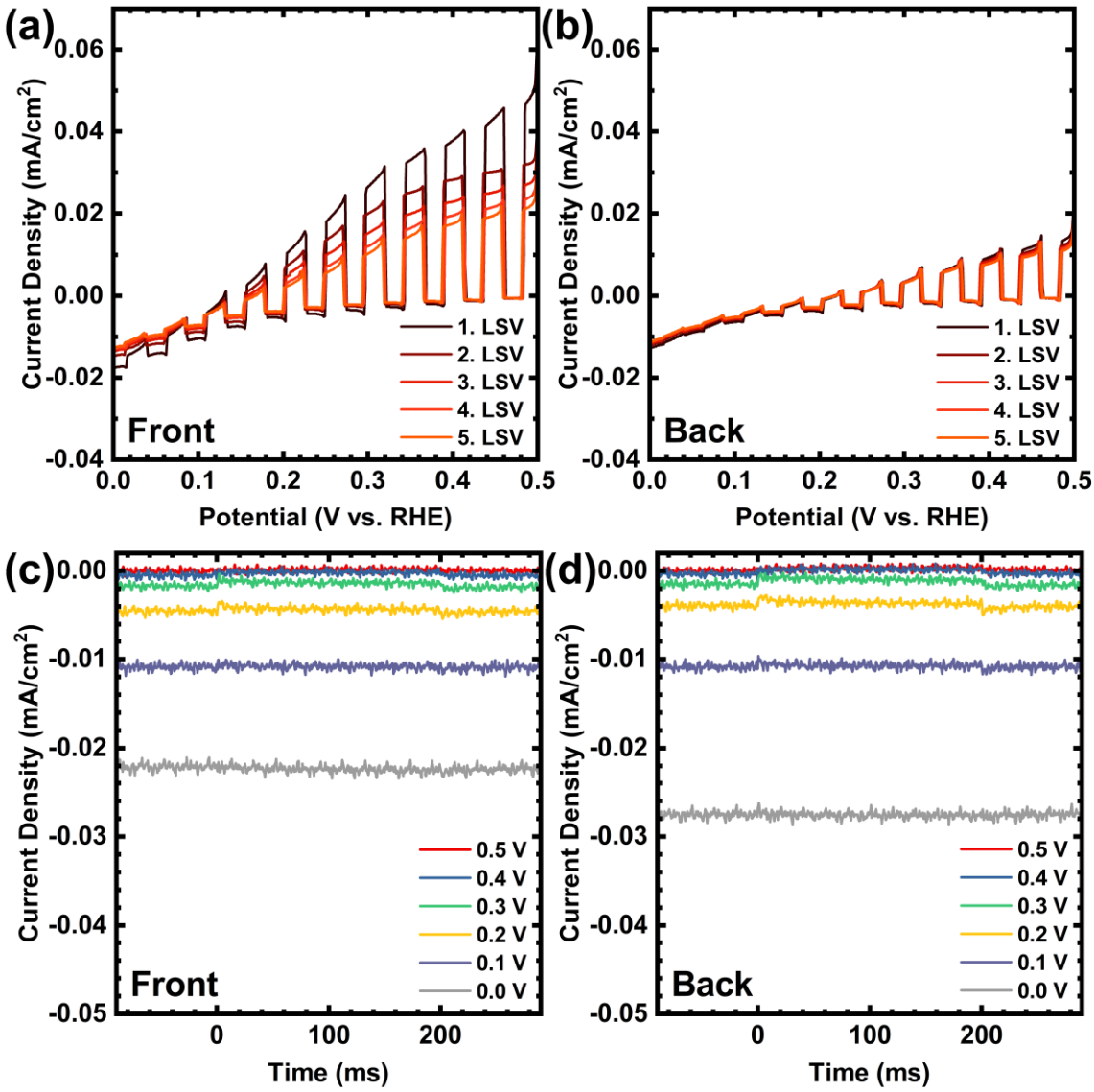

Figure 4.11: Five consecutive cathodic chopped LSV scans of bare TiO_2 under (a) front and (b) back illumination conditions. Potential-dependent TPC measurements were taken from bare TiO_2 under (c) front and (d) back illumination conditions.

The PEC activity and the stability of the bare TiO_2 layer, as well as its TPC response, were also tested to develop an understanding of the possible effects of the TiO_2 as an underlayer. According to the cathodic front-illuminated chopped LSV results in Figure 4.11a, TiO_2 shows a minor photocurrent response that decays steadily from 0.5 V to 0.0 V. On the other hand, under back-illuminated conditions, the photocurrent is mostly lost under 0.1 V, as can be seen in Figure 4.11b.

In terms of TPC response, no significant signal was detected due to the LED spectrum being mostly limited to the visible region. Since the direct band gap of TiO_2 was also estimated as 3.32 eV from the Tauc analysis, the LED's visible light was not

expected to excite the system. Still, a few μA/cm^2's of photocurrent density was observed both under front and back LED illumination which can be seen in Figure 4.11c and Figure 4.11d.

Once the PEC activity and stability of bare Cu_2O and TiO_2 layers are understood along with their TPC response, the FTO/TiO_2/Cu_2O heterojunction was further investigated under the same methods and conditions. Figure 4.12a and its inset include the five consecutive chopped LSV scans of the heterojunction system under front and back illumination conditions. According to these results, the overall PEC activity of the heterojunction system was found to be less than the FTO/Cu_2O system. However, an increase in stability was also noticed. This stability could also be linked to the low cathodic photocurrent performance, causing the photocathode to go through less self-reduction. However, the anodic photocurrent performance above 0.3 V under back illumination in the inset of Figure 4.12a indicates the successful synthesis of the FTO/TiO_2/Cu_2O hierarchy. From this perspective, the anodic photocurrent exceeds the anodic photocurrent of the FTO/TiO_2 system by more than ten times under the same conditions. Therefore, it is clear that there is a collective photoabsorption occurring inside the heterojunction system, which includes both absorption cross-sections of the TiO_2 and Cu_2O layers when the system is illuminated from the back. Such a joint absorption is also beneficial in terms of providing a platform to study both the anodic and cathodic charge carrier processes within the same system in a potential range as narrow as 0.5-0.0 V.

Front-illuminated potential-dependent TPC results given in Figure 4.12b are found to be similar to the previously discussed FTO/Cu_2O results except for the photoreduction peak (III) and the wiggles (IV). Accordingly, the potential dependence of almost all charge carrier processes is once again observed. Yet, the intensity of these events was higher compared to the FTO/Cu_2O system due to the collective absorption effects. Mainly, processes I and V, which heavily rely on the population of the trapped carriers at the photocathode surface, occur at higher intensities. Therefore, this can be claimed as another indication of the heterojunction between the Cu_2O and TiO_2 causing the transfer and accumulation of the excess charge carriers at the photocathode surface.

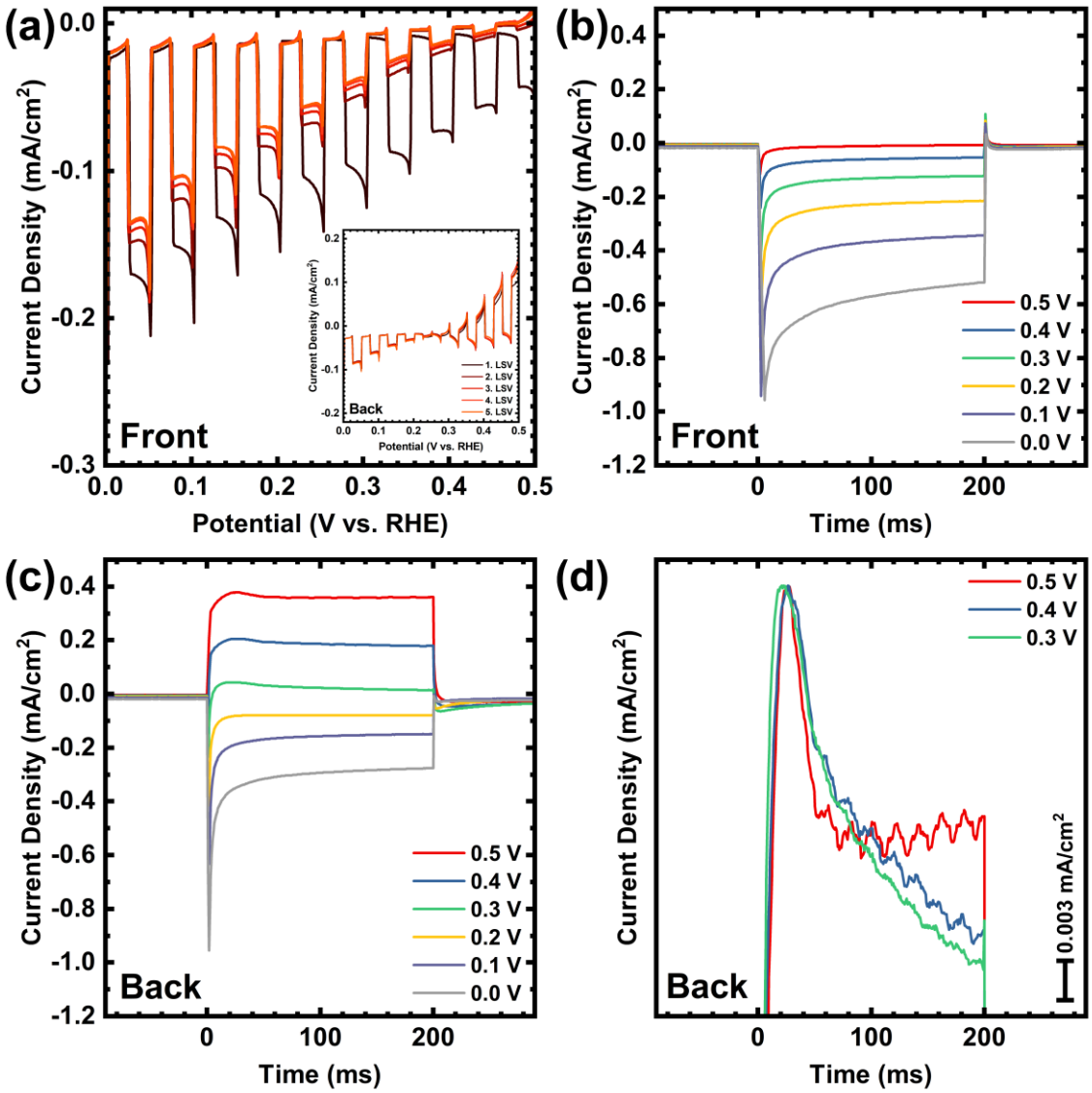

Figure 4.12: (a) Five consecutive front-illuminated chopped LSV scans of the FTO/TiO_2/Cu_2O heterojunction. Potential-dependent TPC measurements taken from the FTO/TiO_2/Cu_2O heterojunction under (b) front and (c) back illumination conditions. (d) Stacked representation of the potential-dependent TPC measurements taken from the FTO/TiO_2/Cu_2O heterojunction under back illumination conditions for 0.5-0.3 V. Inset of (a) includes five consecutive back-illuminated chopped LSV scans of the FTO/TiO_2/Cu_2O heterojunction.

In particular, the back-illuminated potential-dependent TPC measurements in Figure 4.12c show the most exciting results. While an anodic photocurrent behavior is observed for the 0.5-0.3 V interval, the photocurrent switches to cathodic behavior below 0.3 V. This is important due to the heterojunction system being able to drive both OER and HER within a narrow potential range. Hence, the carrier dynamics of the whole system are observed to switch in direction at around 0.3 V.

When looked at in detail, the broad anodic hole accumulation peak at 0.5 V is followed by intense wiggles with no negative cathodic offshoot at the light cut-off. This means that the trapping of the charge carriers does not occur at this potential, and the system is highly efficient at driving PEC OER. It is also vital to notice that the OER photocurrent once again exceeds the bare FTO/TiO_2 photocurrent even under LED illumination due to the collective absorption with the Cu_2O layer. Therefore, it is evident that the photogenerated holes at the TiO_2/Cu_2O interface play an essential role in driving the OER at the Cu_2O/electrolyte interface.

As the potential is lowered in the cathodic direction, the hole trapping process intensifies as it can be seen from the positive offshoot appearing at the light cut-off at 0.3 V. Due to the enhanced hole trapping, electron accumulation at the light switch-off also intensifies. The accumulated electrons at the photocathode surface later recombine with the trapped holes as it was previously described in the FTO/Cu_2O system. Still, the electron trapping is expected to be seriously hindered with the introduction of the TiO_2 underlayer.

The intensity of the wiggles reaches its peak at 0.5 V for the heterojunction system, as depicted in Figure 4.12d. Meanwhile, the bare Cu_2O shows its most intense wiggle behavior at 0.0 V. Regarding these outcomes, the origins of the wiggles can be assigned to the trapped charge carrier species in each system under a certain applied potential. Coherently, the surface electron trapping is thought to be the main cause of the wiggles at 0.5 V for the FTO/TiO_2/Cu_2O system, while the wiggles at 0.0 V for the FTO/Cu_2O system originate from the side processes that involve surface trapped holes. These assignments are also in parallel with the previously pronounced structural characteristics of both systems. The oxygen-defected nature of the FTO/TiO_2/Cu_2O system is prone to electron trapping, while the FTO/Cu_2O bears possible hole trap sites such as Cu^+ or intrinsic V''_{Cu}

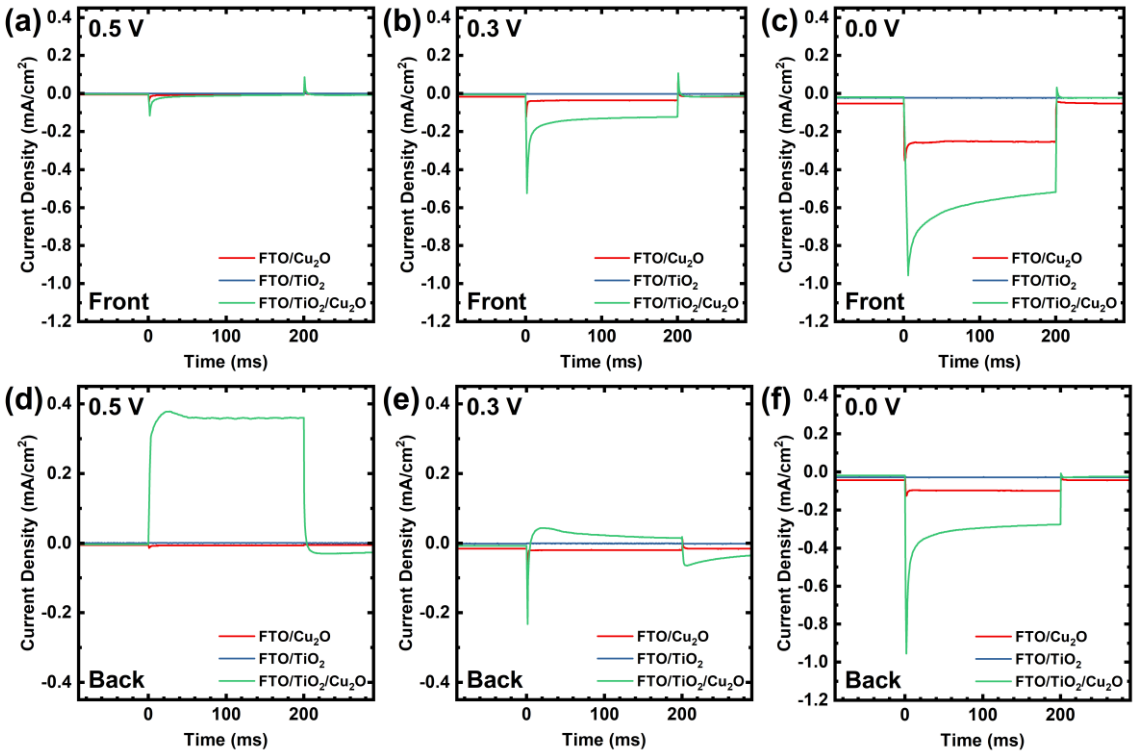

Figure 4.13: Comparison of the potential-dependent TPC measurements taken from the FTO/Cu_2O, FTO/TiO_2, and FTO/TiO_2/Cu_2O systems under front illumination at (a) 0.5 V, (b) 0.3 V, (c) 0.0 V and back illumination at (a) 0.5 V, (b) 0.3 V, (c) 0.0 V.

Comparison of the potential-dependent TPC responses of the bare Cu_2O, bare TiO_2, and heterojunction systems at the critical potential values of 0.5, 0.3, and 0.0 V are shown in Figure 4.13. Accordingly, the front illumination works the same way for all three hierarchies in terms of potential response. Due to a thick layer of Cu_2O on top of the heterojunction system, most of the TPC response emerges from the charge carrier dynamics in this layer. It is important to notice that none of the systems are able to produce photocurrent at 0.5 V, as can be seen in Figure 4.13a. Still, because of the heterojunction effect, the FTO/TiO_2/Cu_2O system gives the highest TPC response in terms of charge accumulation, recombination, stabilized photocurrent, and anodic offshoot intensities at 0.3 and 0.5 V, as represented in Figure 4.13b and Figure 4.13c.

On the other hand, under back illumination conditions at 0.5 V (Figure 4.13d), the heterojunction system produces its highest anodic photocurrent response, while the bare Cu_2O and TiO_2 systems give almost zero photoactivity. Moreover, what happens at the photocurrent behavior switch of the heterojunction system at 0.3 V is clearly visible in Figure 4.13e. The system traps high numbers of electrons before producing an anodic photocurrent, while the FTO/Cu_2O system begins to show a cathodic photocurrent

response at the same potential. This is also confirmed by the negative offshoot occurring at the light switch-off, followed by the dissipation of the trapped electrons with holes. Eventually, in Figure 4.13f, both the FTO/Cu_2O and FTO/TiO_2/Cu_2O systems start to behave similarly cathodic at 0.0 V.

Supported by the structural characterization results and PEC performance tests, the TPC findings shed light on the complex charge carrier dynamics of the FTO/TiO_2/Cu_2O heterojunction photocathode system, as well as bare Cu_2O as a photocathode.

4.4 Conclusion

In conclusion, light-induced charge carrier events such as electron and hole trapping are investigated on both the FTO/Cu_2O and FTO/TiO_2/Cu_2O systems via potential-dependent TPC experiments combined with chopped LSV experiments under front and back illumination conditions and various structural characterization techniques. The results clearly show that the FTO/Cu_2O system suffers from hole trapping, and the introduction of the TiO_2 changes this behavior more towards electron trapping, resulting in enhanced hole utilization dynamics as well as improved stability. Although these results hint at the possible origins of the periodic oscillations observed along the photocurrent response, these wiggles remain a mysterious finding that might contain a lot more information about the side processes that occur in parallel with the PEC OER and HER on the photocathode surface. The effect of electrodeposition times on the structural properties and PEC performances of Cu_2O photocathodes was also investigated. The findings show that longer deposition times result in highly crystalline photocathodes with larger grain sizes and less number of defects. Overall, the study makes connections between the structural integrity and photoactivity of single and heterojunction Cu_2O photocathodes by providing deep insights into the charge carrier mechanisms that hinder the PEC HER activities.

Chapter 5:
SUMMARY & OUTLOOK

In summary, this thesis aims to draw attention to the importance of understanding the charge carrier dynamics in PEC HER research by utilizing time-resolved methods on intriguing photocathode structures. The effects of vacancy defects, as well as heterostructures are investigated from the perspective of ultrafast charge transport and relatively slower interfacial charge transfer dynamics.

In the first part of the thesis, ultrafast charge transport dynamics of CBO photocathodes are investigated. The study aims to fabricate intrinsically p-type, Cu- and Bi-deficient CBO photocathodes to characterize and investigate the effects of cation vacancies on the ultrafast charge transport dynamics in the scope of PEC HER. As a combinational investigation, the study comprises advanced characterization techniques, comprehensive PEC performance tests, and *ex situ*/*in situ* TAS experiments to unravel the different polaron formation tendencies which affect the PEC HER performances of Cu- and Bi-deficient CBO photocathodes. Accordingly, Bi vacancies possess a greater tendency to polaronically trap photogenerated holes and therefore hinder the photocurrent generation in Bi-deficient CBO to a larger extent. Yet, the hole polaron concept needs further comprehension both in CBO and all other photocathodes through element-specific and time-resolved spectroscopic methods.

In the second part, interfacial charge transfer dynamics of Cu_2O-based single and heterojunction photocathodes are investigated. Heterojunction systems play a crucial role in enhancing interfacial charge transfer dynamics. In this context, photocathodes with FTO/Cu_2O and FTO/TiO_2/Cu_2O hierarchies were fabricated and characterized using various bulk- and surface-sensitive characterization methods. Their PEC activity and stability were examined through consecutive LSV scans and TPC measurements under long- and short-pulsed light conditions, respectively. The experimental findings suggest that the bare Cu_2O photocathode suffers from surface hole trapping while the heterojunction photocathode exhibits electron trapping due to its anodic character. In addition, the observation of the periodic photocurrent oscillations, which hint at the existence of side processes that go in parallel with the PEC HER, is an attractive finding.

Nonetheless, the roles of surface-trapped charge carriers in these side processes require further *in situ* time-resolved investigations to unravel their mysteries.

Chapter 6:
REFERENCES

[1] Z. Li, S. Fang, H. Sun, R.-J. Chung, X. Fang, and J.-H. He, 'Solar Hydrogen', *Advanced Energy Materials*, vol. 13, no. 8, p. 2203019, 2023, doi: 10.1002/aenm.202203019.

[2] Y. Li *et al.*, 'Recent progress in hydrogen: From solar to solar cell', *Journal of Materials Science & Technology*, vol. 176, pp. 236–257, Mar. 2024, doi: 10.1016/j.jmst.2023.08.030.

[3] P. Saha *et al.*, 'Grey, blue, and green hydrogen: A comprehensive review of production methods and prospects for zero-emission energy', *International Journal of Green Energy*, vol. 0, no. 0, pp. 1–15, 2023, doi: 10.1080/15435075.2023.2244583.

[4] H. Song, S. Luo, H. Huang, B. Deng, and J. Ye, 'Solar-Driven Hydrogen Production: Recent Advances, Challenges, and Future Perspectives', *ACS Energy Lett.*, vol. 7, no. 3, pp. 1043–1065, Mar. 2022, doi: 10.1021/acsenergylett.1c02591.

[5] Z. Chen, H. N. Dinh, and E. Miller, *Photoelectrochemical Water Splitting: Standards, Experimental Methods, and Protocols*. in SpringerBriefs in Energy. New York, NY: Springer, 2013. doi: 10.1007/978-1-4614-8298-7.

[6] Y. Chen, X. Feng, Y. Liu, X. Guan, C. Burda, and L. Guo, 'Metal Oxide-Based Tandem Cells for Self-Biased Photoelectrochemical Water Splitting', *ACS Energy Lett.*, vol. 5, no. 3, pp. 844–866, Mar. 2020, doi: 10.1021/acsenergylett.9b02620.

[7] J. H. Kim, D. Hansora, P. Sharma, J.-W. Jang, and J. S. Lee, 'Toward practical solar hydrogen production – an artificial photosynthetic leaf-to-farm challenge', *Chem. Soc. Rev.*, vol. 48, no. 7, pp. 1908–1971, 2019, doi: 10.1039/C8CS00699G.

[8] K. Zhang, M. Ma, P. Li, D. H. Wang, and J. H. Park, 'Water Splitting Progress in Tandem Devices: Moving Photolysis beyond Electrolysis', *Advanced Energy Materials*, vol. 6, no. 15, p. 1600602, 2016, doi: 10.1002/aenm.201600602.

[9] A. Fujishima and K. Honda, 'Electrochemical Photolysis of Water at a Semiconductor Electrode', *Nature*, vol. 238, no. 5358, pp. 37–38, Jul. 1972, doi: 10.1038/238037a0.

[10] K. Scott, Ed., *Electrochemical Methods for Hydrogen Production:* in Energy and Environment Series. Cambridge: Royal Society of Chemistry, 2019. doi: 10.1039/9781788016049.

[11] M. Z. Rahman, T. Edvinsson, and J. Gascon, 'Hole utilization in solar hydrogen production', *Nat Rev Chem*, vol. 6, no. 4, Art. no. 4, Apr. 2022, doi: 10.1038/s41570-022-00366-w.

[12] W. Yang and J. Moon, 'Recent Advances in Earth-Abundant Photocathodes for Photoelectrochemical Water Splitting', *ChemSusChem*, vol. 12, no. 9, pp. 1889–1899, Aug. 2019, doi: 10.1002/cssc.201801554.

[13] S. Corby, R. R. Rao, L. Steier, and J. R. Durrant, 'The kinetics of metal oxide photoanodes from charge generation to catalysis', *Nat Rev Mater*, vol. 6, no. 12, pp. 1136–1155, Aug. 2021, doi: 10.1038/s41578-021-00343-7.

[14] J. B. Baxter, C. Richter, and C. A. Schmuttenmaer, 'Ultrafast Carrier Dynamics in Nanostructures for Solar Fuels', *Annual Review of Physical Chemistry*, vol. 65, no. 1, pp. 423–447, Jan. 2014, doi: 10.1146/annurev-physchem-040513-103742.

[15] R. van de Krol and M. Grätzel, Eds., *Photoelectrochemical Hydrogen Production*, vol. 102. in Electronic Materials: Science & Technology, vol. 102. Boston, MA: Springer US, 2012. doi: 10.1007/978-1-4614-1380-6.

[16] H. V. Le, T. L. Le, U. T. D. Thuy, and P. D. Tran, 'Current perspectives in engineering of viable hybrid photocathodes for solar hydrogen generation', *Adv. Nat. Sci: Nanosci. Nanotechnol.*, vol. 9, no. 2, p. 023001, Jun. 2018, doi: 10.1088/2043-6254/aac93e.

[17] A. C. Minja, K. R. Ag, A. Raes, R. Borah, and S. W. Verbruggen, 'Recent progress in developing non-noble metal-based photocathodes for solar green hydrogen production', *Current Opinion in Chemical Engineering*, vol. 43, p. 101000, Mar. 2024, doi: 10.1016/j.coche.2024.101000.

[18] T. Arai, Y. Konishi, Y. Iwasaki, H. Sugihara, and K. Sayama, 'High-Throughput Screening Using Porous Photoelectrode for the Development of Visible-Light-Responsive Semiconductors', *J. Comb. Chem.*, vol. 9, no. 4, pp. 574–581, Jul. 2007, doi: 10.1021/cc0700142.

[19] J. K. Cooper *et al.*, '$CuBi_2O_4$: Electronic Structure, Optical Properties, and Photoelectrochemical Performance Limitations of the Photocathode', *Chem. Mater.*, vol. 33, no. 3, pp. 934–945, Feb. 2021, doi: 10.1021/acs.chemmater.0c03930.

[20] S. P. Berglund, F. F. Abdi, P. Bogdanoff, A. Chemseddine, D. Friedrich, and R. van de Krol, 'Comprehensive Evaluation of $CuBi_2O_4$ as a Photocathode Material for Photoelectrochemical Water Splitting', *Chem. Mater.*, vol. 28, no. 12, pp. 4231–4242, Jun. 2016, doi: 10.1021/acs.chemmater.6b00830.

[21] M. Sun *et al.*, 'Optoelectrical Regulation of $CuBi_2O_4$ Photocathode via Photonic Crystal Structure for Solar–Fuel Conversion', *ACS Appl. Mater. Interfaces*, vol. 14, no. 38, pp. 43946–43954, Sep. 2022, doi: 10.1021/acsami.2c12309.

[22] M. Sun, B. Liu, W. Han, Z. Zhang, and M. Xie, '$CuBi_2O_4$ photocathode with integrated electric field for enhanced H_2O_2 production', *Applied Catalysis B: Environmental*, vol. 304, p. 120980, Dec. 2021, doi: 10.1016/j.apcatb.2021.120980.

[23] Z. Zhang *et al.*, 'Understanding the Role of Oxygen and Hydrogen Defects in Modulating the Optoelectronic Properties of P-Type Metal Oxide Semiconductors', *Chem. Mater.*, vol. 33, no. 19, pp. 7829–7838, Oct. 2021, doi: 10.1021/acs.chemmater.1c02444.

[24] I. L. E. Gonzaga and C. C. Mercado, 'Copper ternary oxides as photocathodes for solar-driven CO_2 reduction', *Reviews on Advanced Materials Science*, vol. 61, no. 1, pp. 430–457, Jan. 2022, doi: 10.1515/rams-2022-0043.

[25] R. Gottesman *et al.*, 'Pure $CuBi_2O_4$ Photoelectrodes with Increased Stability by Rapid Thermal Processing of Bi_2O_3/CuO Grown by Pulsed Laser Deposition', *Adv. Funct. Mater.*, vol. 30, no. 21, p. 1910832, Mar. 2020, doi: 10.1002/adfm.201910832.

[26] Y. Xu *et al.*, 'Bulk Embedding of Ferroelectric Nanodomains in $CuBi_2O_4$ Photocathodes Enables Boosted Photoelectrochemical Hydrogen Generation', *Advanced Functional Materials*, vol. n/a, no. n/a, p. 2213568, Apr. 2023, doi: 10.1002/adfm.202213568.

[27] A. Song *et al.*, 'Cu:NiO as a hole-selective back contact to improve the photoelectrochemical performance of $CuBi_2O_4$ thin film photocathodes', *J. Mater. Chem. A*, vol. 7, no. 15, pp. 9183–9194, Apr. 2019, doi: 10.1039/C9TA01489F.

[28] F. Wang *et al.*, 'Gradient Self-Doped $CuBi_2O_4$ with Highly Improved Charge Separation Efficiency', *J. Am. Chem. Soc.*, vol. 139, no. 42, pp. 15094–15103, Oct. 2017, doi: 10.1021/jacs.7b07847.

[29] H. J. Jung *et al.*, 'Direct Identification of Antisite Cation Intermixing and Correlation with Electronic Conduction in $CuBi_2O_4$ for Photocathodes', *ACS Appl.*

Mater. Interfaces, vol. 12, no. 39, pp. 43720–43727, Sep. 2020, doi: 10.1021/acsami.0c12491.

[30] L. Qu *et al.*, 'Point-defect engineering of nanoporous $CuBi_2O_4$ photocathode via rapid thermal processing for enhanced photoelectrochemical activity', *Journal of Energy Chemistry*, vol. 71, pp. 201–209, Aug. 2022, doi: 10.1016/j.jechem.2022.03.013.

[31] G. Sharma *et al.*, 'Electronic structure, photovoltage, and photocatalytic hydrogen evolution with p-$CuBi_2O_4$ nanocrystals', *J. Mater. Chem. A*, vol. 4, no. 8, pp. 2936–2942, Dec. 2015, doi: https://doi.org/10.1039/C5TA07040F.

[32] S. D. Tilley, M. Schreier, J. Azevedo, M. Stefik, and M. Graetzel, 'Ruthenium Oxide Hydrogen Evolution Catalysis on Composite Cuprous Oxide Water-Splitting Photocathodes', *Advanced Functional Materials*, vol. 24, no. 3, pp. 303–311, 2014, doi: 10.1002/adfm.201301106.

[33] J. Luo, L. Steier, M.-K. Son, M. Schreier, M. T. Mayer, and M. Grätzel, 'Cu_2O Nanowire Photocathodes for Efficient and Durable Solar Water Splitting', *Nano Lett.*, vol. 16, no. 3, pp. 1848–1857, Mar. 2016, doi: 10.1021/acs.nanolett.5b04929.

[34] Y. Zhang *et al.*, 'Modulating the Cu_2O Photoelectrode/Electrolyte Interface with Bilayer Surfactant Simulating Cell Membranes for Boosting Photoelectrochemical CO_2 Reduction', *J. Phys. Chem. Lett.*, vol. 14, no. 27, pp. 6301–6308, Jul. 2023, doi: 10.1021/acs.jpclett.3c00672.

[35] A. Paracchino, V. Laporte, K. Sivula, M. Grätzel, and E. Thimsen, 'Highly active oxide photocathode for photoelectrochemical water reduction', *Nature Mater*, vol. 10, no. 6, pp. 456–461, Jun. 2011, doi: 10.1038/nmat3017.

[36] M. E. Aguirre, R. Zhou, A. J. Eugene, M. I. Guzman, and M. A. Grela, 'Cu_2O/TiO_2 heterostructures for CO_2 reduction through a direct Z-scheme: Protecting Cu_2O from photocorrosion', *Applied Catalysis B: Environmental*, vol. 217, pp. 485–493, Nov. 2017, doi: 10.1016/j.apcatb.2017.05.058.

[37] S. Lany, 'Semiconducting transition metal oxides', *J. Phys.: Condens. Matter*, vol. 27, no. 28, p. 283203, Jul. 2015, doi: 10.1088/0953-8984/27/28/283203.

[38] E. Pastor *et al.*, 'In situ observation of picosecond polaron self-localisation in α-Fe_2O_3 photoelectrochemical cells', *Nat Commun*, vol. 10, no. 1, p. 3962, Sep. 2019, doi: 10.1038/s41467-019-11767-9.

[39] H. Zhu *et al.*, 'In Situ Determination of Polaron-Mediated Ultrafast Electron Trapping in Rutile TiO_2 Nanorod Photoanodes', *J. Phys. Chem. Lett.*, vol. 12, no. 44, pp. 10815–10822, Nov. 2021, doi: 10.1021/acs.jpclett.1c03113.

[40] L. D. Landau, 'On the motion of electrons in a crystal lattice', *Phys. Z. Sowjetunion*, vol. 3, no. 664, 1933.

[41] S. I. Pekar, 'Local quantum states of electrons in an ideal ion crystal', *Zh. Eksp. Teor. Fiz.*, vol. 16, pp. 341–348, 1946.

[42] H. Fröhlich, H. Pelzer, and S. Zienau, *Properties of Slow Electrons in Polar Materials*. Taylor & Francis, 1950.

[43] H. Fröhlich, 'Electrons in lattice fields', *Advances in Physics*, vol. 3, no. 11, pp. 325–361, Jul. 1954, doi: 10.1080/00018735400101213.

[44] T. Holstein, 'Studies of polaron motion: Part I. The molecular-crystal model', *Annals of Physics*, vol. 8, no. 3, pp. 325–342, Nov. 1959, doi: 10.1016/0003-4916(59)90002-8.

[45] T. Holstein, 'Studies of polaron motion : Part II. The "small" polaron', *Annals of Physics*, vol. 8, pp. 343–389, Nov. 1959, doi: 10.1016/0003-4916(59)90003-X.

[46] J. Wiktor, F. Ambrosio, and A. Pasquarello, 'Role of Polarons in Water Splitting: The Case of $BiVO_4$', *ACS Energy Lett.*, vol. 3, no. 7, pp. 1693–1697, Jul. 2018, doi: 10.1021/acsenergylett.8b00938.

[47] A. Kahraman, M. Barzgar Vishlaghi, I. Baylam, A. Sennaroglu, and S. Kaya, 'Roles of Charge Carriers in the Excited State Dynamics of $BiVO_4$ Photoanodes', *J. Phys. Chem. C*, vol. 123, no. 47, pp. 28576–28583, Nov. 2019, doi: 10.1021/acs.jpcc.9b07391.

[48] S. Bandaranayake, E. Hruska, S. Londo, S. Biswas, and L. R. Baker, 'Small Polarons and Surface Defects in Metal Oxide Photocatalysts Studied Using XUV Reflection–Absorption Spectroscopy', *J. Phys. Chem. C*, vol. 124, no. 42, pp. 22853–22870, Oct. 2020, doi: 10.1021/acs.jpcc.0c07047.

[49] C. Franchini, M. Reticcioli, M. Setvin, and U. Diebold, 'Polarons in materials', *Nat Rev Mater*, vol. 6, no. 7, pp. 560–586, Mar. 2021, doi: 10.1038/s41578-021-00289-w.

[50] S. H. Park *et al.*, 'Direct and real-time observation of hole transport dynamics in anatase TiO_2 using X-ray free-electron laser', *Nat Commun*, vol. 13, no. 1, Art. no. 1, May 2022, doi: 10.1038/s41467-022-30336-1.

[51] S. Corby *et al.*, 'Water Oxidation and Electron Extraction Kinetics in Nanostructured Tungsten Trioxide Photoanodes', *J. Am. Chem. Soc.*, vol. 140, no. 47, pp. 16168–16177, Nov. 2018, doi: 10.1021/jacs.8b08852.

[52] W. Qiu, S. Xiao, Y. Tong, and S. Yang, 'Toward Efficient Charge Collection and Light Absorption: A Perspective of Light Trapping for Advanced Photoelectrodes', *J. Phys. Chem. C*, vol. 123, no. 31, pp. 18753–18770, Aug. 2019, doi: 10.1021/acs.jpcc.9b01533.

[53] E. Pastor, M. Sachs, S. Selim, J. R. Durrant, A. A. Bakulin, and A. Walsh, 'Electronic defects in metal oxide photocatalysts', *Nat Rev Mater*, vol. 7, no. 7, pp. 503–521, Jul. 2022, doi: 10.1038/s41578-022-00433-0.

[54] Z. Zhang, B. Zhu, and X. Guan, 'Operational Spectroelectrochemical Investigation on the Interfacial Charge Dynamics of Copper Bismuth Oxide Based Photocathode', *J. Phys. Chem. Lett.*, vol. 13, no. 10, pp. 2356–2364, Mar. 2022, doi: 10.1021/acs.jpclett.2c00140.

[55] D. Derelli *et al.*, 'Photodegradation of $CuBi_2O_4$ Films Evidenced by Fast Formation of Metallic Bi using Operando Surface-sensitive X-ray Scattering', *Angewandte Chemie International Edition*, vol. 62, no. 43, p. e202307948, 2023, doi: 10.1002/anie.202307948.

[56] E. Ö. Alagöz, H. Jahangiri, and S. Kaya, 'Profound influence of surface trap states on the utilization of charge carriers in CdS photoanodes', *Materials Advances*, vol. 5, no. 4, pp. 1513–1522, 2024, doi: 10.1039/D3MA00847A.

[57] S. Selim *et al.*, 'Impact of Oxygen Vacancy Occupancy on Charge Carrier Dynamics in $BiVO_4$ Photoanodes', *J. Am. Chem. Soc.*, vol. 141, no. 47, pp. 18791–18798, Nov. 2019, doi: 10.1021/jacs.9b09056.

[58] D. Li *et al.*, 'Unraveling the Kinetics of Photocatalytic Water Oxidation on WO_3', *J. Phys. Chem. Lett.*, vol. 11, no. 2, pp. 412–418, Jan. 2020, doi: 10.1021/acs.jpclett.9b03340.

[59] W. Yang *et al.*, 'Time-Resolved Observations of Photo-Generated Charge-Carrier Dynamics in Sb_2Se_3 Photocathodes for Photoelectrochemical Water Splitting', *ACS Nano*, vol. 12, no. 11, pp. 11088–11097, Nov. 2018, doi: 10.1021/acsnano.8b05446.

[60] F. Le Formal, K. Sivula, and M. Grätzel, 'The Transient Photocurrent and Photovoltage Behavior of a Hematite Photoanode under Working Conditions and

the Influence of Surface Treatments', *J. Phys. Chem. C*, vol. 116, no. 51, pp. 26707–26720, Dec. 2012, doi: 10.1021/jp308591k.

[61] F. Boudoire, Y. Liu, F. Le Formal, N. Guijarro, C. R. Lhermitte, and K. Sivula, 'Spray Synthesis of $CuFeO_2$ Photocathodes and In-Operando Assessment of Charge Carrier Recombination', *J. Phys. Chem. C*, vol. 125, no. 20, pp. 10883–10890, May 2021, doi: 10.1021/acs.jpcc.1c02282.

[62] J. Xue and J. Bao, 'Interfacial charge transfer of heterojunction photocatalysts: Characterization and calculation', *Surfaces and Interfaces*, vol. 25, p. 101265, Aug. 2021, doi: 10.1016/j.surfin.2021.101265.

[63] M. D. Tyona, 'A theoritical study on spin coating technique', *1*, vol. 2, no. 4, Art. no. 4, Dec. 2013.

[64] J. H. Kim, A. Adishev, J. Kim, Y. S. Kim, S. Cho, and J. S. Lee, 'All-Bismuth-Based Oxide Tandem Cell for Solar Overall Water Splitting', *ACS Appl. Energy Mater.*, vol. 1, no. 12, pp. 6694–6699, Dec. 2018, doi: 10.1021/acsaem.8b01025.

[65] S. A. M. Al-Bat'hi, 'Electrodeposition of Nanostructure Materials', in *Electroplating of Nanostructures*, IntechOpen, 2015. doi: 10.5772/61389.

[66] J. Paglione, N. P. Butch, and E. E. Rodriguez, *Fundamentals Of Quantum Materials: A Practical Guide To Synthesis And Exploration*. World Scientific, 2021.

[67] Y. Wang, F. Cai, P. Guo, Y. Lei, Q. Xi, and F. Wang, 'Short-Time Hydrothermal Synthesis of $CuBi_2O_4$ Nanocolumn Arrays for Efficient Visible-Light Photocatalysis', *Nanomaterials*, vol. 9, no. 9, p. 1257, Sep. 2019, doi: 10.3390/nano9091257.

[68] A. Alyamani, O. M. Lemine, A. Alyamani, and O. M. Lemine, 'FE-SEM Characterization of Some Nanomaterial', in *Scanning Electron Microscopy*, IntechOpen, 2012. doi: 10.5772/34361.

[69] G. Friedbacher and H. Bubert, Eds., *Surface and Thin Film Analysis*, 1st ed. John Wiley & Sons, Ltd, 2011. doi: 10.1002/9783527636921.

[70] F. A. Stevie and C. L. Donley, 'Introduction to x-ray photoelectron spectroscopy', *Journal of Vacuum Science & Technology A*, vol. 38, no. 6, p. 063204, Sep. 2020, doi: 10.1116/6.0000412.

[71] J. Epp, '4 - X-ray diffraction (XRD) techniques for materials characterization', in *Materials Characterization Using Nondestructive Evaluation (NDE) Methods*, G.

Hübschen, I. Altpeter, R. Tschuncky, and H.-G. Herrmann, Eds., Woodhead Publishing, 2016, pp. 81–124. doi: 10.1016/B978-0-08-100040-3.00004-3.

[72] Y. C. Jean, P. E. Mallon, and D. M. Schrader, *Principles and Applications of Positron and Positronium Chemistry*. World Scientific, 2003. doi: 10.1142/5086.

[73] A. Arrar *et al.*, 'Optical and photoluminescence spectroscopy analysis and Doppler broadening annihilation radiation studies of perovskites based on $La_{1-X}Ni_XMnO_{2.75}$ thin layers', *Optik*, vol. 224, p. 165678, Dec. 2020, doi: 10.1016/j.ijleo.2020.165678.

[74] J. Dryzek, 'SP-SE: Evaluation program of Doppler broadening parameters S and W'. 2024. [Online]. Available: https://ifj.edu.pl/private/jdryzek/page_r18.html

[75] M. Izerrouken, R. Hazem, S. Kuzeci, C. Tav, U. Yahsi, and S. Limam, 'Electronic ionisation-induced annealing of pre-existing defects in Al_2O_3 and CaF_2 single crystals', *Philosophical Magazine*, vol. 102, no. 4, pp. 283–298, Feb. 2022, doi: 10.1080/14786435.2021.1989075.

[76] M. Izerrouken *et al.*, 'Heavy ion irradiation induced defects in Zircaloy-4', *Phys. Scr.*, vol. 96, no. 4, p. 045008, Feb. 2021, doi: 10.1088/1402-4896/abe3bf.

[77] S. P. Mulvaney and C. D. Keating, 'Raman Spectroscopy', *Anal. Chem.*, vol. 72, no. 12, pp. 145–158, Jun. 2000, doi: 10.1021/a10000155.

[78] A. Kudelski, 'Analytical applications of Raman spectroscopy', *Talanta*, vol. 76, no. 1, pp. 1–8, Jun. 2008, doi: 10.1016/j.talanta.2008.02.042.

[79] M. Picollo, M. Aceto, and T. Vitorino, 'UV-Vis spectroscopy', *Physical Sciences Reviews*, vol. 4, no. 4, Apr. 2019, doi: 10.1515/psr-2018-0008.

[80] J. Klein, L. Kampermann, B. Mockenhaupt, M. Behrens, J. Strunk, and G. Bacher, 'Limitations of the Tauc Plot Method', *Advanced Functional Materials*, vol. 33, no. 47, p. 2304523, 2023, doi: 10.1002/adfm.202304523.

[81] A. J. Bard, L. R. Faulkner, and H. S. White, *Electrochemical Methods: Fundamentals and Applications*. John Wiley & Sons, 2022.

[82] R. Berera, R. van Grondelle, and J. T. M. Kennis, 'Ultrafast transient absorption spectroscopy: principles and application to photosynthetic systems', *Photosynth Res*, vol. 101, no. 2, pp. 105–118, Sep. 2009, doi: 10.1007/s11120-009-9454-y.

[83] J. Zhang, B. Zhu, L. Zhang, and J. Yu, 'Femtosecond transient absorption spectroscopy investigation into the electron transfer mechanism in photocatalysis', *Chem. Commun.*, vol. 59, no. 6, pp. 688–699, Jan. 2023, doi: 10.1039/D2CC06300J.

[84] K. E. Knowles, M. D. Koch, and J. L. Shelton, ‘Three applications of ultrafast transient absorption spectroscopy of semiconductor thin films: spectroelectrochemistry, microscopy, and identification of thermal contributions’, *Journal of Materials Chemistry C*, vol. 6, no. 44, pp. 11853–11867, 2018, doi: 10.1039/C8TC02977F.

[85] T.-H. Lai, K. Katsumata, and Y.-J. Hsu, ‘In situ charge carrier dynamics of semiconductor nanostructures for advanced photoelectrochemical and photocatalytic applications’, *Nanophotonics*, vol. 10, no. 2, pp. 777–795, Dec. 2020, doi: 10.1515/nanoph-2020-0472.

[86] X. Xiong, M. Forster, J. D. Major, Y. Xu, and A. J. Cowan, ‘Time-Resolved Spectroscopy of ZnTe Photocathodes for Solar Fuel Production’, *J. Phys. Chem. C*, vol. 121, no. 40, pp. 22073–22080, Oct. 2017, doi: 10.1021/acs.jpcc.7b06304.

[87] L. Shenje, S. Larson, Y. Zhao, and S. Ullrich, ‘Composition Effects on Ultrafast Optical Properties of Cu_xO_y Thin Films: A Transient Absorption Study’, *J. Phys. Chem. C*, vol. 124, no. 45, pp. 24908–24918, Nov. 2020, doi: 10.1021/acs.jpcc.0c08716.

[88] J. Liu *et al.*, ‘Ultrafast carrier dynamics of Cu_2O thin film induced by two-photon excitation’, *Chinese Phys. B*, vol. 30, no. 11, p. 114205, Dec. 2021, doi: 10.1088/1674-1056/ac003c.

[89] Z. Zhang *et al.*, ‘Fermi Level Engineering of Passivation and Electron Transport Materials for p-Type $CuBi_2O_4$ Employing a High-Throughput Methodology’, *Adv. Funct. Mater.*, vol. 30, no. 24, p. 2000948, May 2020, doi: 10.1002/adfm.202000948.

[90] B. Tan, B. Liu, M. Sun, Y. Li, Z. Cao, and Z. Zhang, ‘Enhanced charge collection and surface activity of a $CuBi_2O_4$ photocathode crystal facet engineering’, *J. Mater. Chem. A*, vol. 10, no. 17, pp. 9427–9434, Mar. 2022, doi: 10.1039/D2TA00476C.

[91] B. Duployer, C. Tenailleau, Y. Thimont, P. Lenormand, A. Barnabé, and L. Presmanes, ‘Preparation and study of $CuBi_2O_4$ thin films by RF magnetron sputtering’, *Materials Research Bulletin*, vol. 130, p. 110940, Oct. 2020, doi: 10.1016/j.materresbull.2020.110940.

[92] H. Ghimire, P. V. V. Jayaweera, D. Somvanshi, Y. Lao, and A. G. U. Perera, ‘Recent Progress on Extended Wavelength and Split-Off Band Heterostructure Infrared

Detectors', *Micromachines*, vol. 11, no. 6, Art. no. 6, May 2020, doi: 10.3390/mi11060547.

[93] S. R. Pendlebury *et al.*, 'Ultrafast Charge Carrier Recombination and Trapping in Hematite Photoanodes under Applied Bias', *J. Am. Chem. Soc.*, vol. 136, no. 28, pp. 9854–9857, Jul. 2014, doi: 10.1021/ja504473e.

[94] I. Grigioni, L. Ganzer, F. V. A. Camargo, B. Bozzini, G. Cerullo, and E. Selli, 'In Operando Photoelectrochemical Femtosecond Transient Absorption Spectroscopy of WO_3/$BiVO_4$ Heterojunctions', *ACS Energy Lett.*, vol. 4, no. 9, pp. 2213–2219, Sep. 2019, doi: 10.1021/acsenergylett.9b01150.

[95] J. Miao, Y. Yang, P. Cui, C. Ru, and K. Zhang, 'Improving Charge Transfer Beyond Conventional Heterojunction Photoelectrodes: Fundamentals, Strategies and Applications', *Advanced Functional Materials*, vol. n/a, no. n/a, p. 2406443, doi: 10.1002/adfm.202406443.

[96] S. Meng, W. Sun, S. Zhang, X. Zheng, X. Fu, and S. Chen, 'Insight into the Transfer Mechanism of Photogenerated Carriers for WO_3/TiO_2 Heterojunction Photocatalysts: Is It the Transfer of Band–Band or Z-Scheme? Why?', *J. Phys. Chem. C*, vol. 122, no. 46, pp. 26326–26336, Nov. 2018, doi: 10.1021/acs.jpcc.8b07524.

[97] A. Song, I. Levine, R. van de Krol, T. Dittrich, and S. P. Berglund, 'Revealing the relationship between photoelectrochemical performance and interface hole trapping in $CuBi_2O_4$ heterojunction photoelectrodes', *Chem. Sci.*, vol. 11, no. 41, pp. 11195–11204, Oct. 2020, doi: 10.1039/D0SC03030A.

[98] S. Lettieri, M. Pavone, A. Fioravanti, L. Santamaria Amato, and P. Maddalena, 'Charge Carrier Processes and Optical Properties in TiO_2 and TiO_2-Based Heterojunction Photocatalysts: A Review', *Materials*, vol. 14, no. 7, Art. no. 7, Jan. 2021, doi: 10.3390/ma14071645.

[99] A. Iqbal *et al.*, 'Charge Transport Phenomena in Heterojunction Photocatalysts: The WO_3/TiO_2 System as an Archetypical Model', *ACS Appl. Mater. Interfaces*, vol. 13, no. 8, pp. 9781–9793, Mar. 2021, doi: 10.1021/acsami.0c19692.

[100] E. Usman, M. Barzgar Vishlaghi, A. Kahraman, N. Solati, and S. Kaya, 'Modifying the Electron-Trapping Process at the $BiVO_4$ Surface States via the TiO_2 Overlayer for Enhanced Water Oxidation', *ACS Appl. Mater. Interfaces*, vol. 13, no. 50, pp. 60602–60611, Dec. 2021, doi: 10.1021/acsami.1c16847.

[101] D. H. Wi, M. A. Lumley, Z. Xi, M. Liu, and K.-S. Choi, 'Investigation of Electron Extraction and Protection Layers on Cu_2O Photocathodes', *Chem. Mater.*, vol. 35, no. 11, pp. 4385–4392, Jun. 2023, doi: 10.1021/acs.chemmater.3c00543.

[102] M. B. Akbar, Y. Gong, Y. Wang, A. R. Woldu, X. Zhang, and T. He, 'Role of TiO_2 coating layer on the performance of Cu_2O photocathode in photoelectrochemical CO_2 reduction', *Nanotechnology*, vol. 32, no. 39, p. 395707, Jul. 2021, doi: 10.1088/1361-6528/ac0ddb.

[103] W. Siripala, A. Ivanovskaya, T. F. Jaramillo, S.-H. Baeck, and E. W. McFarland, 'A Cu_2O/TiO_2 heterojunction thin film cathode for photoelectrocatalysis', *Solar Energy Materials and Solar Cells*, vol. 77, no. 3, pp. 229–237, May 2003, doi: 10.1016/S0927-0248(02)00343-4.

[104] M. Nishikawa *et al.*, 'A method to give chemically stabilities of photoelectrodes for water splitting: Compositing of a highly crystalized TiO_2 layer on a chemically unstable Cu_2O photocathode using laser-induced crystallization process', *Applied Surface Science*, vol. 363, pp. 173–180, Feb. 2016, doi: 10.1016/j.apsusc.2015.12.002.

[105] H. E. Kim, D. H. Wi, J. S. Lee, and K.-S. Choi, 'Photoelectrochemical Nitrate and Nitrite Reduction Using Cu_2O Photocathodes', *ACS Energy Lett.*, vol. 9, no. 5, pp. 1993–1999, May 2024, doi: 10.1021/acsenergylett.4c00256.

[106] L. Pan *et al.*, 'High carrier mobility along the [111] orientation in Cu_2O photoelectrodes', *Nature*, vol. 628, no. 8009, pp. 765–770, Apr. 2024, doi: 10.1038/s41586-024-07273-8.

[107] M. Schleuning *et al.*, 'Carrier Localization on the Nanometer-Scale limits Transport in Metal Oxide Photoabsorbers', *Advanced Functional Materials*, vol. 33, no. 25, p. 2300065, 2023, doi: 10.1002/adfm.202300065.

[108] G. F. Harrington and J. Santiso, 'Back-to-Basics tutorial: X-ray diffraction of thin films', *J Electroceram*, vol. 47, no. 4, pp. 141–163, Dec. 2021, doi: 10.1007/s10832-021-00263-6.

[109] S. Tafazoli, M. Yusufoğlu, T. Balkan, and S. Kaya, 'In-situ surface enhanced Raman spectroscopy investigations on surface transformations of oxide derived copper electrodes during CO_2RR', *Journal of Catalysis*, vol. 423, pp. 118–128, Jul. 2023, doi: 10.1016/j.jcat.2023.04.021.

[110] M. Valvo, J. Thyr, and T. Edvinsson, ‘Defect-Induced Raman Scattering in Cu_2O Nanostructures and Their Photocatalytic Performance’, *ChemElectroChem*, vol. 10, no. 22, p. e202300376, 2023, doi: 10.1002/celc.202300376.

[111] S. Challagulla, K. Tarafder, R. Ganesan, and S. Roy, ‘Structure sensitive photocatalytic reduction of nitroarenes over TiO_2’, *Sci Rep*, vol. 7, no. 1, p. 8783, Aug. 2017, doi: 10.1038/s41598-017-08599-2.

[112] J. Yao *et al.*, ‘Oxygen-Defect Enhanced Anion Adsorption Energy Toward Super-Rate and Durable Cathode for Ni–Zn Batteries’, *Nano-Micro Lett.*, vol. 13, no. 1, p. 167, Aug. 2021, doi: 10.1007/s40820-021-00699-z.

Chapter 7:

APPENDIX

7.1 Supporting Information for Chapter 3

Table 7.1: (a) Cu:Bi ratio of Cu-deficient and Bi-deficient CBO thin-film photocathodes and pristine CBO powder.

	Cu:Bi Ratio
CBO powder	0.54
Cu-deficient	0.46
Bi-deficient	0.67

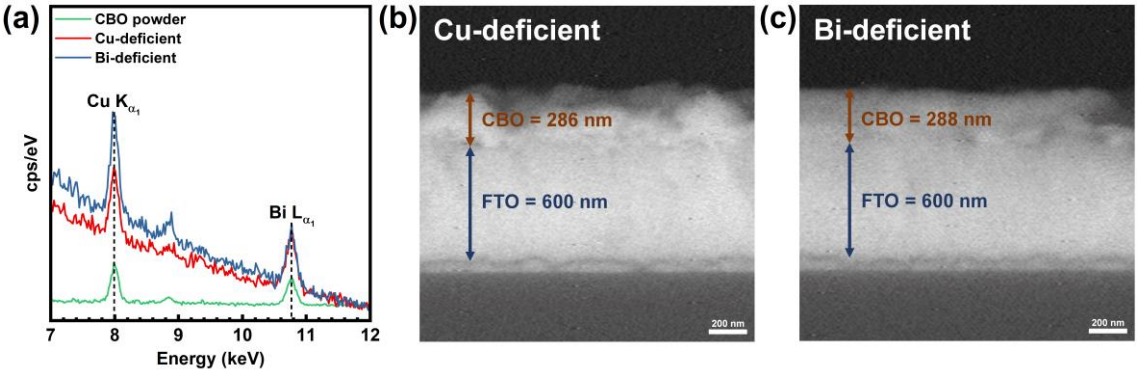

Figure 7.1: (a) EDX spectra of CBO powder (Cu:Bi = 0.54), Cu-deficient (Cu:Bi = 0.46), and Bi-deficient (Cu:Bi = 0.67) CBO. Cross-sectional SEM images of (b) Cu-deficient and (c) Bi-deficient CBO photocathodes.

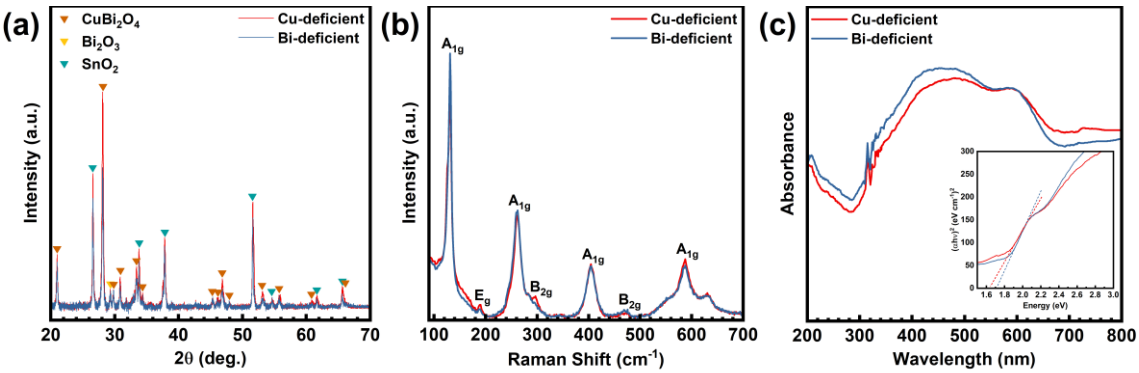

Figure 7.2: (a) XRD, (b) Raman spectra, and (c) UV–vis absorbance spectra of Cu-deficient (E_g = 1.63 eV) and Bi-deficient (E_g = 1.71 eV) CBOs. Inset of (c): Tauc analysis to determine the band gap values. The (a) reflections at 26.59° (110), 33.82° (101), 37.79° (200), 51.63° (211), 54.58° (220), 61.65° (310), and 65.62° (301) belong to the FTO (SnO_2, cassiterite – PDF 01-070-4175) layer.

Table 7.2: The crystallite size and strain of the CBO photocathode were estimated from the analysis of the XRD data.

	CBO Crystallite Size (nm)	CBO Strain
Cu-deficient	139.6	0.354
Bi-deficient	120.9	0.763

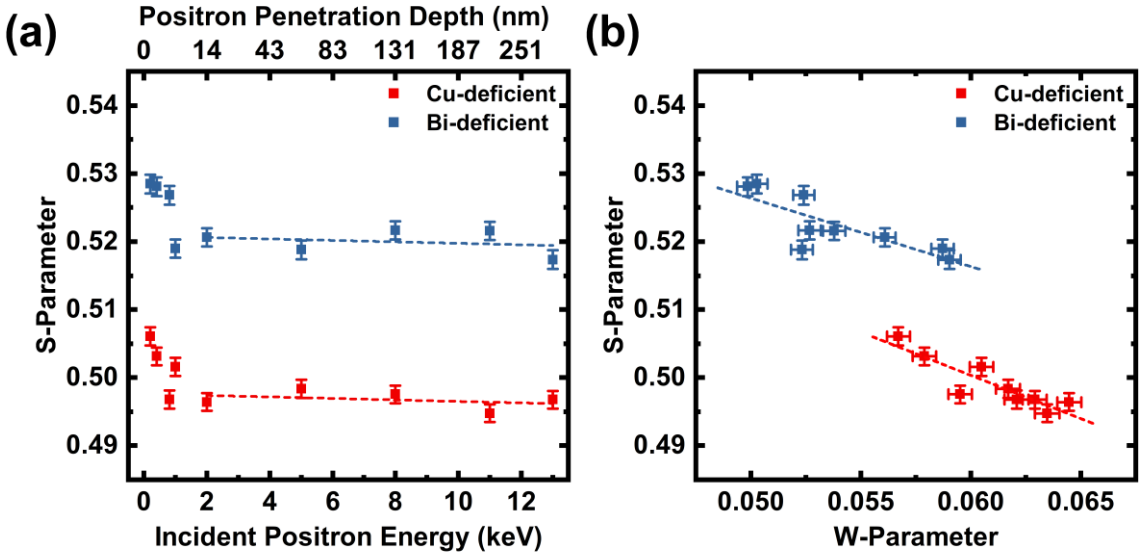

Figure 7.3: DBS of positron annihilation (a) S-parameter vs. incident positron energy (positron penetration depth) and (b) S-parameter vs. W-parameter graphs. The fit lines are shown as dashed lines.

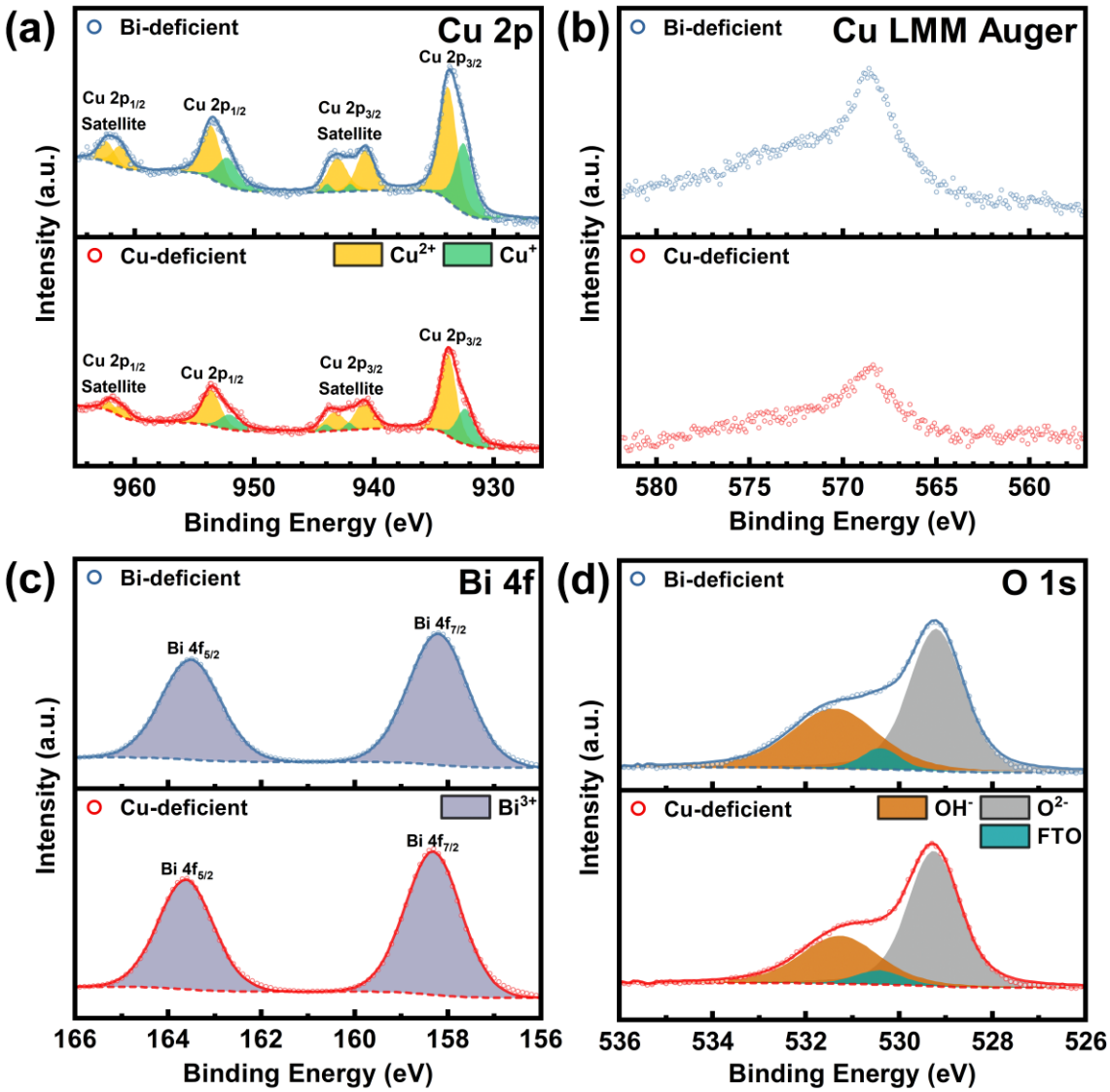

Figure 7.4: (a) Cu 2p, (b) Cu LMM Auger, (c) Bi 4f, and (d) O 1 s XPS spectra of Cu-deficient and Bi-Deficient CBOs.

Table 7.3: Z-fitting results of Nyquist plots obtained from potential-dependent PEIS measurements.

	R_{ct} (kΩ)	
	Cu-deficient	**Bi-deficient**
Dark OCP	666.1	8660.0
Light OCP	53.3	54.3
0.9 V	2.1	2.7
0.7 V	1.5	2.2
0.4 V	1.3	0.6